NONLINEAR MECHANICS OF GRAPHENE MEMBRANES AND RELATED SYSTEMS

A Dissertation

Presented to the Faculty of the Graduate School

of Cornell University

in Partial Fulfillment of the Requirements for the Degree of

Doctor of Philosophy

by

Roberto De Alba

January 2017

NONLINEAR MECHANICS OF GRAPHENE MEMBRANES AND RELATED SYSTEMS

Roberto De Alba, Ph.D.

Cornell University 2017

Micro- and nano-mechanical resonators with low mass and high vibrational frequency are often studied for applications in mass and force detection where they can offer unparalleled precision. They are also excellent systems with which to study nonlinear phenomena and fundamental physics due to the numerous routes through which they can couple to each other or to external systems.

In this work we study the structural, thermal, and nonlinear properties of various micro-mechanical systems. First, we present a study of graphene-coated silicon nitride membranes; the resulting devices demonstrate the high quality factors of silicon nitride as well as the useful electrical and optical properties of graphene. We then study nonlinear mechanics in pure graphene membranes, where all vibrational eigenmodes are coupled to one another through the membrane tension. This effect enables coherent energy transfer from one mechanical mode to another, in effect creating a graphene mechanics-based frequency mixer. In another experiment, we measure the resonant frequency of a graphene membrane over a wide temperature range, 80K - 550K, to determine whether or not it demonstrates the negative thermal expansion coefficient predicted by prevailing theories; our results indicate that this coefficient is positive at low temperatures – possibly due to polymer contaminants on the graphene surface – and negative above room temperature. Lastly, we study optically-induced self-oscillation in metal-coated silicon nitride nanowires. These structures exhibit

self-oscillation at extremely low laser powers (~ 1 μW incident on the nanowire), and we use this photo-thermal effect to counteract the viscous air-damping that normally inhibits micro-mechanical motion.

Biographical Sketch

Roberto – "Bob" – was born in Laredo, Texas, a warm and culturally vibrant city on the Texas-Mexico border. He grew up with a fervent interest in math and science, and at the age of 18 moved to College Station, Texas to study chemistry at Texas A&M University. After a semester of organic chemistry, he quickly discovered his passion for physics and changed focus. He graduated with a bachelor's degree in physics in 2010, and moved to Ithaca, New York to attend graduate school at Cornell. There, he has studied nonlinear behavior of micro-mechanical systems under the guidance of Jeevak Parpia.

Bob has recently accepted a post-doctoral position at NIST in Gaithersburg, Maryland.

For Mom & Dad, without whom none of this would have been possible.

Acknowledgements

Firstly, I would like to acknowledge my advisor Jeevak Parpia. Without his guidance and support I could not have developed the experimental and analytical skills needed to succeed in this research. I would also like to thank Professors Paul McEuen and Harold Craighead for years of insightful discussions and priceless feedback. Many thanks are also due to Eric Smith for all of his advice and help in the lab.

Vivek Adiga and Abhilash Sebastian taught me a great deal about nanofabrication, vacuum systems, and other experimental techniques. They also greatly contributed much to my work, from fabricating devices to building apparatuses, and I am forever indebted to them. I am also very glad to call both of them friends.

I would like to thank Nikolay Zhelev, for taking me under his wing as a new graduate student and for always offering his help – no matter what experimental difficulty I faced.

Lastly, I'd like to thank all those close friends who stuck by me though the years and made the burdens of graduate school all the lighter: Nathan Mirman, David MacNeill, Veronica Pillar, Kathryn McGill, Jen Grab, Ethan Kassner, Andy Bohn, and others. And to my lovely girlfriend Rachel Steinhardt: your support has meant the world to me.

Table of Contents

List of Tables

List of Figures

Chapter 1

Introduction

In 1983, Richard Feynman laid out his vision for micro-machines in a lecture at Jet Propulsion Laboratory [18]. Having witnessed the boom in progress towards ever smaller electronic devices, and the societal impact of integrated circuits, batch fabrication, and personal computers, he speculated on the untapped potential of small mechanical devices. While he considered this avenue of research important, he had difficulty predicting the applications of micro-machines. In his own words:

> "What use would such things be? Now it gets embarrassing. I tried very hard to think of a use that sounded sensible – or semisensible – you'll have to judge."

He went on to describe arrays of micro-shutters for filtering light to create programmable lithography masks or as a new means of producing television images, medicinal micro-robots that he referred to as "swallowable surgeons", and

a new form of entertainment (akin to a video game) in which a person steers a swimming, sword-wielding micro-robot to combat single-celled organisms in water.

In the years since Prof. Feynman's lecture, the fields of Micro-Electro-Mechanical Systems (MEMS) and Nano-Electro-Mechanical Systems (NEMS) have developed and matured into vibrant research fields encompassing modern physics, materials science, mechanical and electrical engineering, and an industry worth $6 billion USD in 2012 [1]. Although his grand vision for micro-machines involved complex robots moving in three dimensions, the most impactful devices (commercially and for fundamental research) have often been the simplest structures: cantilevers, doubly-clamped beams, or membranes. Furthermore, he could not predict the role that simple oscillatory motion would have in making MEMS structures important in modern consumer electronics or in the study of quantum motion.

This thesis focuses on the fundamental physics of NEMS resonators consisting of two-dimensional membranes and one-dimensional wires. In the case of membranes, we focus on graphene – a single layer of carbon atoms arranged in a honeycomb lattice. This material represents the ultimate limit of thinness in mechanical devices, benefiting many sensing applications in which low mass is desirable, while also being electrically conducting and strongly interacting with light – making it easier to manipulate and more functional. Our primary interests are: 1) using this material to improve existing NEMS devices, 2) uncovering its intrinsic non-linear mechanics which can be exploited for novel device applications, and 3) understanding its peculiar temperature-dependent behaviors, which differ greatly between theory and experiment.

For the case of wires, we study the interaction between light and oscillatory motion in a system that is only 50 nm – or roughly 200 atoms – in both width and height, but 40 μm long. More specifically, we study light's ability to induce motion and set constraints on that motion, with an eye towards future device applications and experiments.

1.1 MEMS & NEMS

MEMS describes the use of mechanical (usually moving) parts on the 1 μm to 100 μm length-scales, integrated with electronics, to accomplish specific tasks. Because of their small footprint, low mass, low power consumption, and sensitivity to electro-magnetic fields, strains, pressures, temperature changes, inertial forces, and other external stimuli, they are typically used as sensors or actuators on the micron scale.

Conveniently, MEMS are largely made using the same batch-fabrication processes already developed for the semiconductor industry (lithography, deposition, etching, etc.), and can consist of a wide range of materials. One of the early papers that discussed development of MEMS devices and spread awareness of their potential was Kurt Petersen's "Silicon as a mechanical material" [19]. Today, MEMS devices can incorporate piezoelectrics, magnetic films, optical absorbers and reflectors, tensioned membranes, and micro-fluidic channels. Commercially, they are used as accelerometers which detect impacts in automobiles to deploy airbags, as pressure sensors in car tires, as disposable blood pressures sensors, as arrays of moving micro-mirrors in display technologies, and countless other applications. They are found in modern smartphones as accelerome-

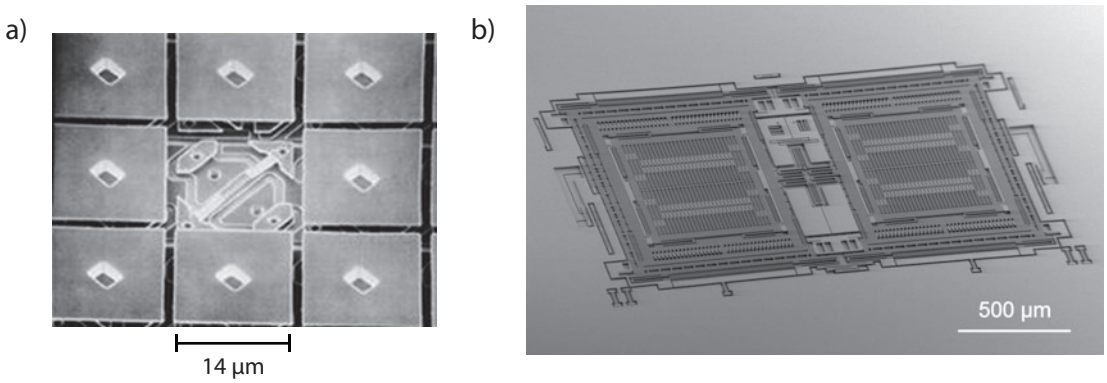

Figure 1.1: **Commercial MEMS devices.** (a) A 3x3 array of tilting micromirrors from a Digital Light Processing chip (©Texas Instruments), with center mirror missing to show hinge assembly. These are commonly used in cinema projectors and projects for schools and offices. (b) A MEMS gyroscope, which operates by vibrating a central proof mass in the plane and detecting the out-of-plane motion generated upon external rotation of the device. Both images are taken from Ref. 1.

ters, gyroscopes, microphones, and as mechanical oscillators which serve as frequency references for microprocessors. For a timeline of the history of MEMS devices and information on their many uses, Refs. 1 & 20. Two commercial MEMS structures are shown in Figure 1.1.

In the laboratory, MEMS and NEMS (the nanometer-scale counterpart to MEMS) are among the most sensitive detectors of force, mass, pressure, and motion available today. Possibly the most familiar MEMS deice to an experimental physicist is a vibrating AFM (atomic force microscopy) cantilever tip, which in optimal conditions can image surfaces with atomic resolution. To illustrate the sensitivity of resonant MEMS/NEMS devices, we will consider a mass sensor. Examples of two mass sensors are shown in Figure 1.2. The resonant frequency

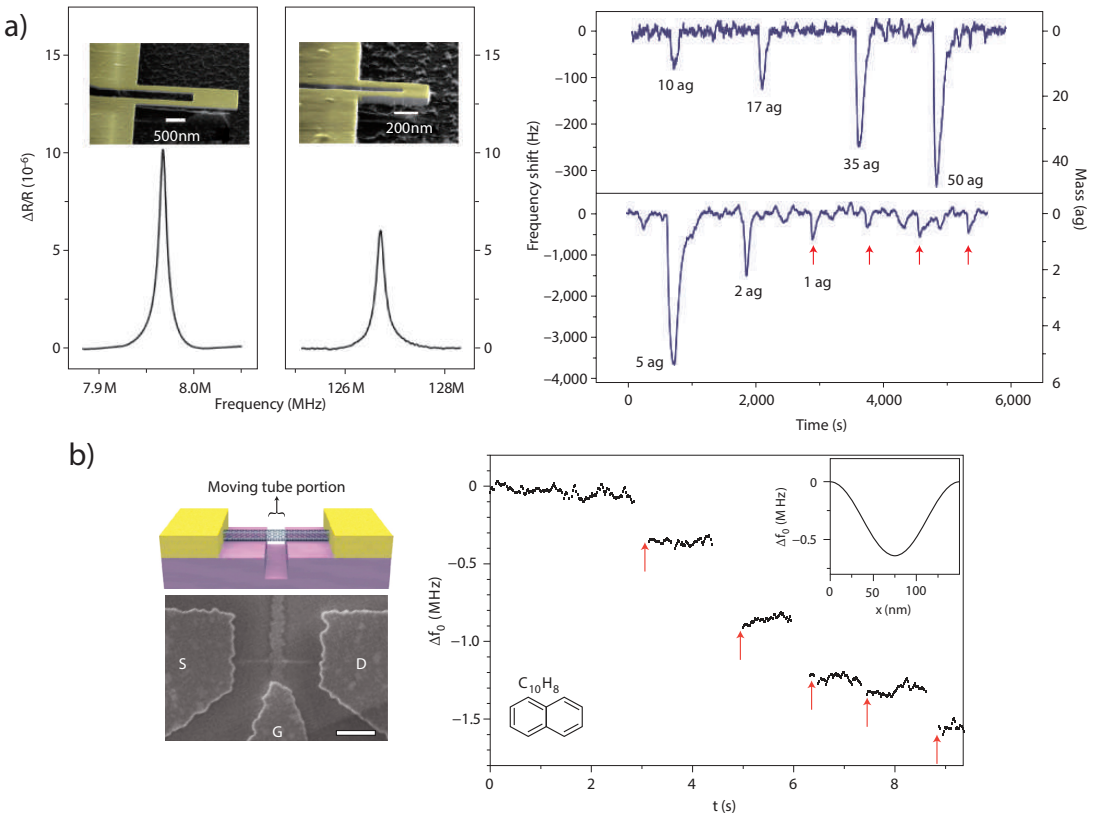

Figure 1.2: **Laboratory-grade MEMS/NEMS sensors.** (a) SiC cantilever-based mass sensors. Left: Scanning electron microscopy (SEM) images of two piezoresistive cantilevers, and their resonance peaks measured in units of resistance change. Right: Resonant frequency shifts for the two devices as $C_2H_4F_2$ gas molecules interact with the cantilevers (Ref. 2). (b) A suspended carbon nanotube mass sensor. Left: Device schematic and SEM image; scale bar: 300 nm. Right: Measured frequency shift versus time during exposure to $C_{10}H_8$ molecules. Red arrows denote sudden shifts which are consistent with detection of a single molecule (Ref. 3).

f_0 of any mechanical resonator can be defined as

$$f_0 = \frac{1}{2\pi}\sqrt{\frac{k}{m}} \tag{1.1}$$

where k and m are the spring constant and mass of the resonator, respectively. Upon adding a small bit of mass Δm (which we wish to detect), the resonant

frequency shits by an amount Δf, which to first order can be approximated as

$$\Delta f = -\frac{1}{2}\frac{\Delta m}{m} f_0. \tag{1.2}$$

This then shows us two of the dual advantages of small systems: the incredibly low mass m and high frequencies f_0 of MEMS/NEMS both contribute to large frequency shifts for the same added mass Δm. But how does the resonant frequency f_0 depend on device dimensions? For a cantilever beam, the spring constant is given by

$$k = \frac{wt^3 E}{4L^3} \tag{1.3}$$

where w is the beam width, t is the thickness, L is the length, and E is its elastic modulus [20]. We thus see that if each dimension of the cantilever is reduced by a constant factor s, then k also reduces by s. However, the mass m scales as the volume of the cantilever and so reduces by a factor of s^3. By Eq. 1.1, this results in a frequency f_0 that increases as $1/s$. So we see finally that $\Delta f \propto 1/s^4$, and smaller devices have drastically larger frequency shifts.

Usually a frequency shift Δf is detected by measuring a resonance peak of the device – *i.e.* applying a drive force at varying frequencies near f_0 and measuring the resulting motion. Two example peaks are shown in Figure 1.2 (a). The full width at half maximum (FWHM) of this peak is a measure of damping in the mechanical system, and we will call it γ. A typical figure of merit for mechanical resonators is the quality factor $Q = f_0/\gamma$, which is a dimensionless number. An equivalent definition of Q is the ratio of the total mechanical energy in a resonator to the energy lost per cycle. Typical Q factors for MEMS range from 10^3 to 10^6. For a mass sensor, the minimum detectable mass Δm_{min} is determined by how well one can detect a shift in the resonance peak. If we assume that the peak location f_0 can be determined accurately to some fixed

fraction of the FWHM γ, the ultimate sensitivity scales as

$$\Delta m_{\min} \propto \frac{m}{Q}. \tag{1.4}$$

This shows that quality factor also plays a large role in determining device performance [21].

Other than sensors, one of the major goals of MEMS/NEMS research is to explore nonlinear phenomena and discover new ways to exploit these devices for future applications. To explain what is meant by "nonlinear phenomena," we first consider the equation of motion for a linear harmonic oscillator:

$$\ddot{x} + \gamma\dot{x} + \omega_0^2 x = F_{\mathrm{d}}(t) \tag{1.5}$$

This differential equation describes the evolution of the oscillator position x with time t; dots denote time derivatives. The resonant frequency is here written in angular units as $\omega_0 = 2\pi f_0$, as is the damping $\gamma = \omega_0/Q$. The term $F_{\mathrm{d}}(t)$ is an applied drive force. If a sinusoidal force $F_{\mathrm{d}}(t) = F\cos\omega t$ is applied, and $Q \gg 1$, the solution of this equation (as a function of drive frequency ω) is a standard Lorentzian resonance peak like that seen in Figure 1.2 (a):

$$x^2 = \left(\frac{F}{2\omega_0}\right)^2 \frac{1}{(\omega_0 - \omega)^2 + (\gamma/2)^2} \tag{1.6}$$

Nonlinear effects in MEMS/NEMS devices modify the equation of motion (Eq. 1.5) in a number of interesting ways, including:

$$\ddot{x} + \gamma\dot{x} + \omega_0^2 x + \beta x^3 = F_{\mathrm{d}}(t) \tag{1.7}$$

$$\ddot{x} + \gamma\dot{x} + \omega_0^2 x + \eta x^2\dot{x} = F_{\mathrm{d}}(t) \tag{1.8}$$

$$\ddot{x} + \gamma\dot{x} + \Big(1 - F\cos(2\omega_0 t)\Big)\omega_0^2 x = 0 \tag{1.9}$$

$$\ddot{x} + \gamma\dot{x} + \omega_0^2(x - y) = F_{\mathrm{d}}(t) \tag{1.10}$$

In the first of these, β is known as a Duffing coefficient, and it effectively changes the resonant frequency ω_0 as the vibration amplitude x^2 increases. In the second equation, η is a nonlinear damping coefficient, which effectively alters γ as x^2 increases. The third equation denotes "parametric excitation," which is when the experimenter can directly modulate the resonant frequency; usually a modulation "force" F is applied at frequency $2\omega_0$. The last equation demonstrates coupling between the oscillator x and a second oscillator y, which has its own equation of motion similar to Eq. 1.5.

Each of these types of nonlinearities brings with it new ways to manipulate and exploit resonator motion. Figure 1.3 shows an example of a MEMS structure with both a Duffing nonlinearity β and parametric excitation [4]. In this example, the resonator is driven into motion by a parametric drive force at frequency $2\omega_0$, and responds with one of two phases (0 or π) relative to the drive. The phase of motion can then serve as a bit of information, which can easily be written, erased, or flipped. This served as a proof of concept that mechanical resonators can be an alternative to transistor memory. In a follow up paper by the same group, it was demonstrated that each vibrational mode of the bridge (of which there are infinitely many) can serve as an independent bit of data [22]. Furthermore, because the modes are coupled in a manner akin to Eq. 1.10, data can be transferred from one mode to another. Other groups have utilized nonlinear effects to drastically enhance the frequency stability of MEMS oscillators for timing applications [23], devise new architectures for NEMS voltage controlled oscillators [24], and more.

Yet another exciting and busy field of study with MEMS/NEMS is the ongoing quest to observe and manipulate quantum states of motion. There are

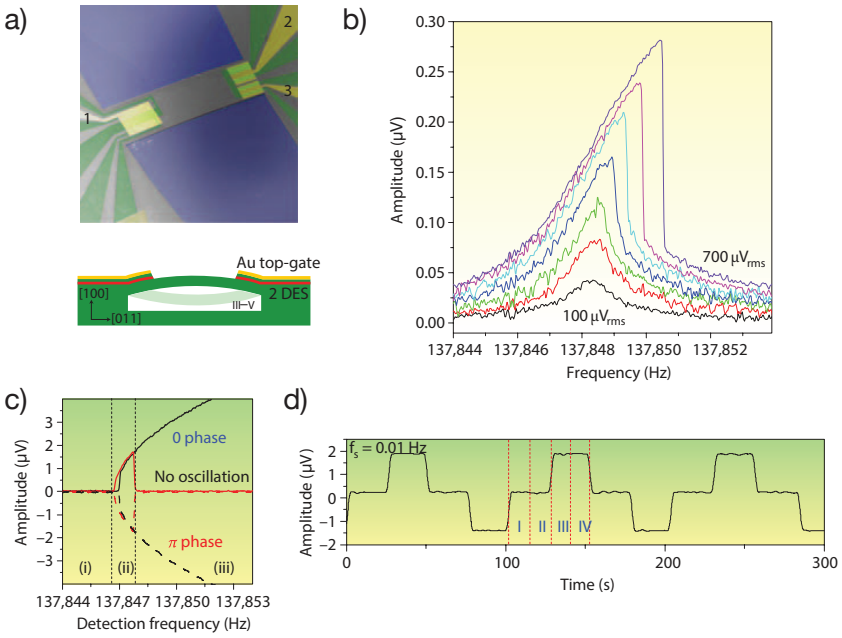

Figure 1.3: **A MEMS device used as a mechanical bit.** (a) SEM image & diagram of the 260 μm-long MEMS bridge. (b) Asymmetric resonance peaks indicative of a Duffing nonlinearity are measured upon applying a strong drive force. (c) Upon applying parametric excitation at $2\omega_0$, the bridge can oscillate with one of two phases: 0 or π. (d) The bridge can be controllably switched between the 0 and π phases and used for data storage. Taken from Ref. 4.

multiple reasons to do so: 1) To test quantum theory in the regime of large sizes and masses (compared to individual atoms). 2) To explore the transition between classical and quantum behavior. 3) To interface mechanics with quantum optics and electronics, leading to new quantum communications technology. 4) To test theories of quantum coherence.

The difficulty in observing quantum behavior is that at laboratory temperatures MEMS/NEMS have thermal phonon occupations of up to $n_m \approx 10^6$. That is to say, they undergo large thermal motion at room temperature that keeps them behaving classically. Since phonons obey Bose-Einstein statistics,

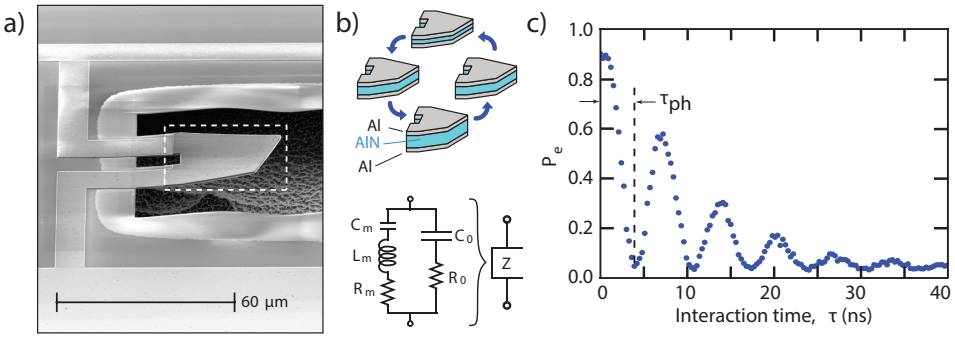

Figure 1.4: **Quantum measurements of a 6 GHz MEMS resonator.** (a) SEM image of the suspended cantilever resonator. (b) The mechanical resonance studied is the vertical "dilatation mode", in which the cantilever thickness oscillates (top diagram). (c) The resonator is coupled to a superconducting qubit to measure its quantum state. Shown is P_e, the probability of measuring the qubit in its excited state, after it is allowed to interact with the resonator for a time τ. At $\tau = 0$ the resonator is prepared with a single phonon, and the oscillations are caused by swapping of the phonon between the resonator and qubit. The decay is caused by loss of the phonon to the thermal bath of the resonator. The experiment is performed in a dilution refrigerator at 25 mK. Taken from Ref 5.

the mean number of phonons in a mechanical resonator with frequency ω_m at temperature T is $n_m = [\exp(\hbar\omega_m/k_BT) - 1]^{-1}$, where $\hbar, k_B$ are the reduced Planck constant and Boltzmann constant. In order to reach the quantum ground state and have an occupancy of $n_m \ll 1$, the resonator would need to be cooled to temperatures $T \ll \hbar\omega_m/k_B$. For a resonator in the audible frequency range with $\omega_m \approx 2\pi \times 1$ kHz, this would require $T \ll 50$ nK – far below what is possible with modern refrigeration.

Despite these challenges, quantum behavior has already been observed in MEMS/NEMS systems, and techniques for doing so are constantly being developed/improved. Reaching the ground state can at present be done by two means: 1) Using a very high frequency NEMS device with $\omega_m \gtrsim 2\pi \times 1$ GHz,

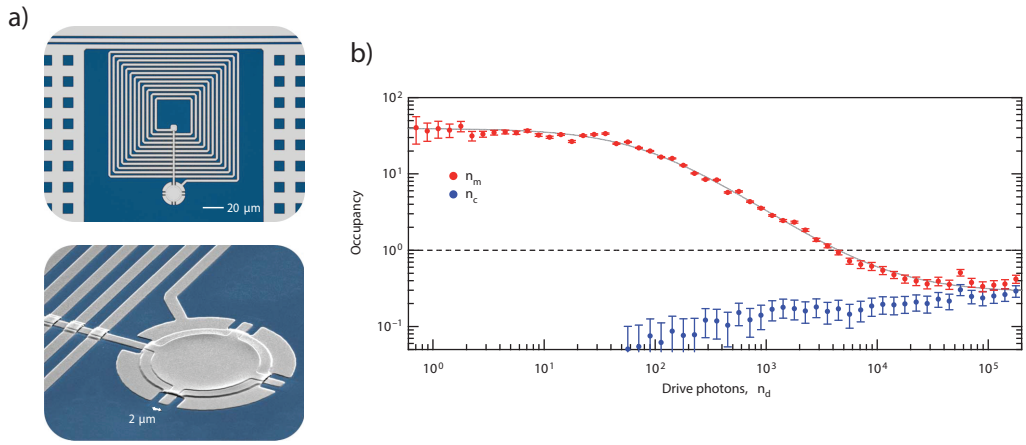

Figure 1.5: **Cooling a mechanical resonator with photons.** (a) SEM image of the circular membrane capacitor with vibration frequency of $\omega_m/2\pi = 10\,\text{MHz}$ (bottom image), and the spiral inductor forming an LRC (inductor-resistor-capacitor) resonant circuit with frequency of $\omega_c/2\pi = 7\,\text{GHz}$ (top image). The LRC circuit is commonly referred to as a microwave cavity. (b) Cooling of the mechanical mode into its ground state by driving the microwave cavity with a voltage at frequency $\omega_c - \omega_m$. Plotted are the occupancy of the mechanical mode n_m and microwave cavity n_c versus cavity drive strength. The experiment is performed at 20 mK. Taken from Refs. 6, 7.

which relaxes the temperature requirement to $T \lesssim 50\,\text{mK}$. This temperature can be reached in a modern dilution refrigerator. 2) Cooling the mechanical resonator "artificially" by coupling it to an electromagnetic resonant circuit or optical cavity resonator with resonant frequency $\omega_c \gtrsim 2\pi \times 1\,\text{GHz}$. Because the mechanical resonator and optical cavity are coupled, the experimenter can remove phonons and convert them into photons in the optical system. This is typically done by driving the optical system with laser light or microwave energy with frequency $\omega_c - \omega_m$. This is referred to as "red sideband pumping," and results in efficient conversion of phonons at frequency ω_m into photons at ω_c. For a great introduction and review of cavity cooling of mechanical resonators, see Ref. 15. An example of both of these approaches is shown in Figures 1.4 & 1.5.

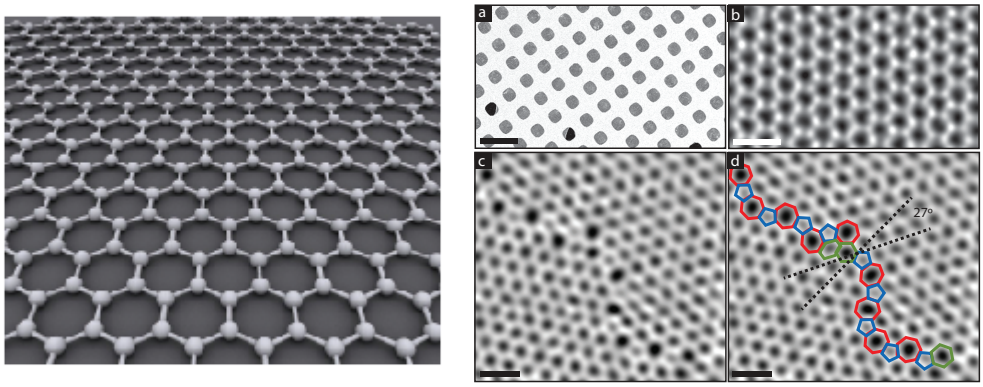

Figure 1.6: Left: Artist's rendering of a graphene sheet (source: Wikipedia). Right: (a) SEM image of graphene on a Transmission Electron Microscopy (TEM) grid; scale bar: 5 μm. (b-d) Images of the boundary between two graphene crystals taken using Scanning TEM; scale bars: 0.5 nm. Taken from Ref. 8.

1.2 Graphene NEMS

Since its discovery in 2004 [25], graphene has garnered much attention for its remarkable electronic, mechanical, and optical properties. The full breadth of graphene's electronic capabilities is beyond the scope of this introduction, but for a review see Ref. 26. From a NEMS perspective, graphene is highly attractive for a number of reasons. Firstly, it is the thinnest material known to man, being only a single carbon atom (or about 0.34 nm) thick. This means that as a 2-dimensional membrane it has the lowest mass possible for a NEMS-based force, mass, or pressure sensor. Secondly, it is electrically conducting and therefore very easy to integrate into electrical devices and drive its mechanical motion. Thirdly, it has a high mechanical stiffness and is extremely strong. Its tensile strength is 130 GPa, making it stronger than a sheet of steel of comparable thickness [27]. This means that it can be stretched incredibly far and undergo large motion without breaking – meaning that nonlinear behavior akin to Eqs. 1.7 -

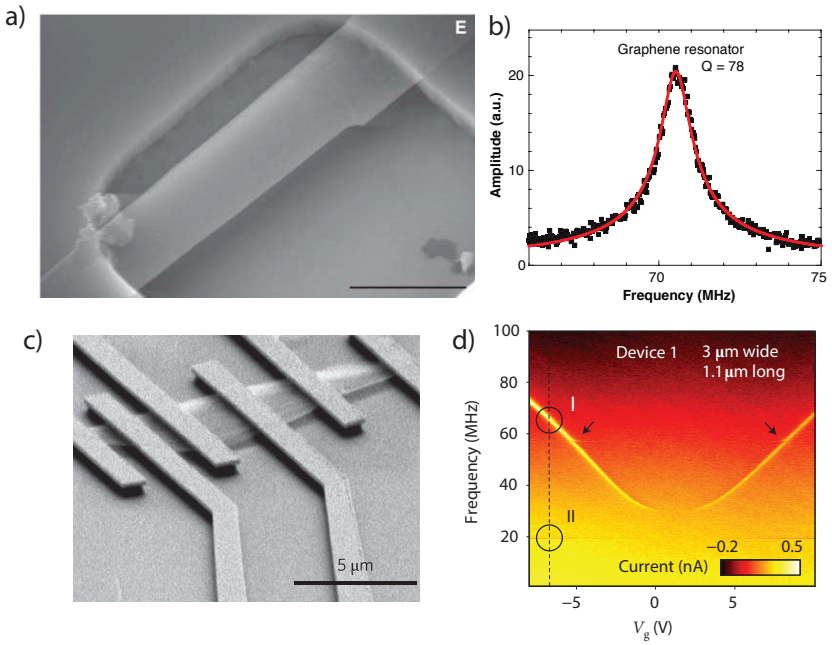

Figure 1.7: **Early graphene NEMS.** (a,b) The first graphene resonator, suspended above a linear trench (scale bar is 1 μm), and its measured resonance peak. The motion was driven by an applied AC voltage and detected optically by shining a laser on the graphene and measuring the reflected light. Taken from Ref. 9. (c,d) The first electrically integrated graphene resonator, suspended between metal electrodes, and its resonant frequency versus applied DC voltage. The bright yellow "U-shaped" curve shows the resonant frequency tunability with voltage. Taken from Ref. 10.

1.10 is accessible.

The first graphene NEMS resonators were made here at Cornell in 2007 by exfoliation [9]. This is the process by which an experimenter uses sticky tape to mechanically peel graphene layers from a bulk graphite crystal, and was the original method used to produce graphene [25]. One of these devices is shown in Figure 1.7 (a). The next milestone was the first fully electrically integrated device in 2009 [10], shown in Figure 1.7 (b). In this device, the graphene was suspended between metal electrodes, and resonant motion was both driven and

detected electrically. Furthermore, it was the first demonstration of the incredible tunability of graphene's resonant frequency. This tunability (also shown in Fig. 1.7 (b)) comes from an applied DC (direct current) voltage which stretches the graphene out-of-plane and increases its tension. This offers a range of tuning far wider than most other MEMS/NEMS structures (often several times the original frequency), and has become a hallmark of graphene devices. It makes graphene promising for a number of electronics applications, including signal processing, tunable bandpass filters, and voltage-controlled oscillators.

Exfoliation produces pure single-crystal graphene, but it is not scaleable. It typically yields graphene flakes 10 μm in length or smaller. A huge advancement came with the ability to grow graphene on copper foil using Chemical Vapor Deposition (CVD) [28]. With this method arbitrarily large graphene sheets can be produced. In the laboratory this is typically a few cm^2, although sheets as long as 30 inches have been reported [29]. This technique was quickly adopted to graphene NEMS, and large arrays of graphene resonators were fabricated on a single silicon chip [30, 31]. Despite its advantages, there are two drawbacks to CVD graphene: 1) It is polycrystalline, meaning it consists of many graphene crystals that are "stitched" together (see Fig. 1.6). This can degrade the graphene's electrical properties and mechanical strength, but usually not to an extent relevant for NEMS. 2) After graphene is grown by CVD, it must be removed from its copper substrate and transferred to the device substrate. This process is usually facilitated by an acidic copper etch and a temporary polymer coating on the graphene, both of which can leave residue on the graphene surface. Several techniques have been developed to circumvent these issues, however [32, 33].

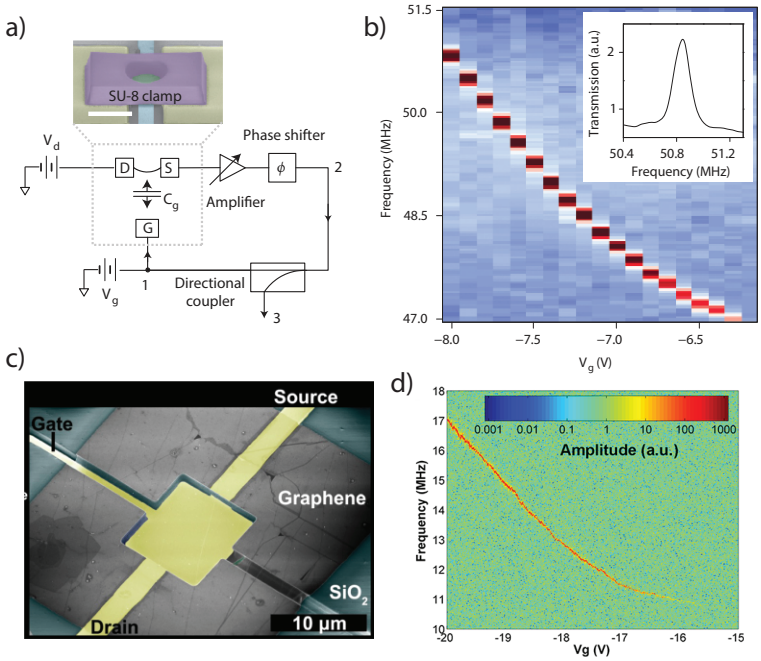

Figure 1.8: **More modern graphene NEMS.** (a,b) A graphene membrane operated as a voltage-controlled oscillator. Shown are the circular graphene membrane (in the SU-8 clamp), its circuit diagram, and the oscillation frequency versus DC voltage. Taken from Ref. 11. (c,d) A square graphene membrane which self-oscillates when exposed to laser light. Shown are the device with its metal Source, Drain, and Gate electrodes, and its oscillation frequency versus DC voltage when exposed to intense green light. Taken from Ref. 12.

In the years since the first graphene NEMS device, there has been a constant push to study its properties and discover new applications. Two of these are shown in Figure 1.8. In one case, the graphene was operated in an electrical feedback loop to create a self-sustaining oscillator with a very widely tunable frequency [11]. In the other, its strong optical absorption was utilized to couple its motion to incident laser light through a phenomenon known as the photothermal effect [12]. Through control of the laser intensity and wavelength, the experimenters were able to tune the frequency and damping of the membrane,

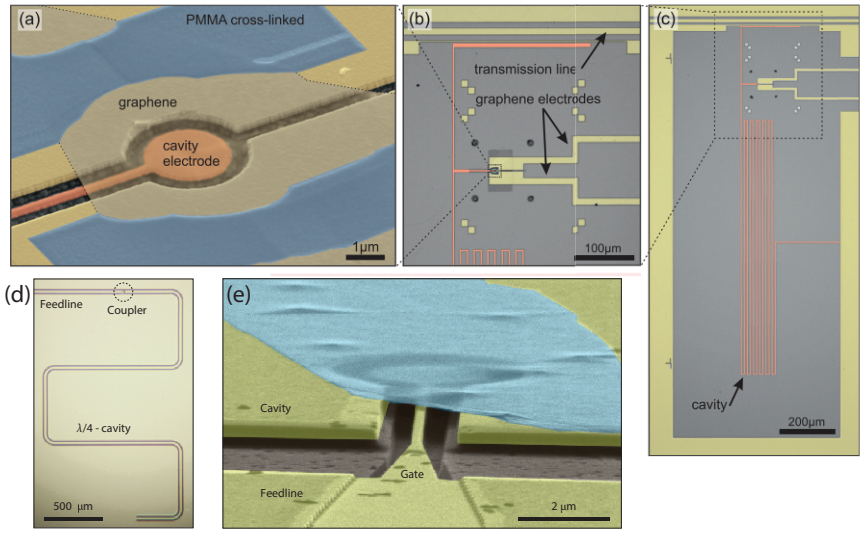

Figure 1.9: **Graphene NEMS coupled to microwave cavities.** The first devices demonstrating a graphene membrane coupled to an on-chip resonant microwave circuit. This coupling is a prerequisite to cooling graphene motion into the quantum regime. (a-c) Taken from Ref. 13. (d,e) Taken from Ref. 14.

as well as induce self-sustained oscillation. This effect will be elaborated on in the next section. Additional work has shown that graphene has a wide range of interesting nonlinear behavior, from nonlinear damping [34] to a voltage-tunable Duffing coefficient [13].

Because of its incredibly low mass, graphene membranes are also promising systems in which to observe quantum effects. This is because the zero-point motion of an oscillator – *i.e.* the quantum motion it undergoes in its ground state – depends on its mass and frequency as $x_{\mathrm{zpm}} = (\hbar/2m\omega_m)^{1/2}$. Thus graphene should have the largest zero-point motion of any membrane material. Furthermore, because it conducts it can easily be coupled to a resonant microwave circuit and cooled via the cavity cooling method described in the previous section (see Figure 1.5). Efforts are already underway to study quantum motion in graphene

membranes, and coupling to microwave cavities has already been reported, as shown in Figure 1.9.

The progress in graphene NEMS as described here represents the combined efforts of researchers across the globe, and is by no means comprehensive. For reviews up to 2013, see Refs. 35, 36. For additional reading specifically on the work done at Cornell, see the Ph.D. theses in Refs. 37–40.

1.3 Optomechanics and NEMS

Cavity cooling of a MEMS/NEMS resonator, as described in Sections 1.1 & 1.2 (see Figure 1.5), is an effect mediated by radiation pressure. A schematic diagram of this effect is shown in Figure 1.10. Light and motion are coupled together in the following manner: The mechanical resonator (a doubly-clamped bridge in the Fig. 1.10) comprises one mirror in a two-mirror optical cavity. The mechanical system and optical cavity have resonant frequencies of Ω_m and ω_{cav}, respectively. In steady state, there is a fixed intensity of laser light circulating in the optical cavity ($\hat{a}$ in the figure). This circulating light exerts radiation pressure on the mechanical resonator. If the resonator position x changes, it alters the cavity length, which in turn alters the intensity of circulating light. This affects the radiation pressure, and thus leads to another change in x. In this way, there is a feedback loop (mediated by the optics) by which any movement in x leads to a responsive force on x.

The feedback force can be in phase with the motion x (which would lead to amplification of motion), or out of phase with x (which would lead to deamplification of motion). In the laboratory setting, one can control the feed-

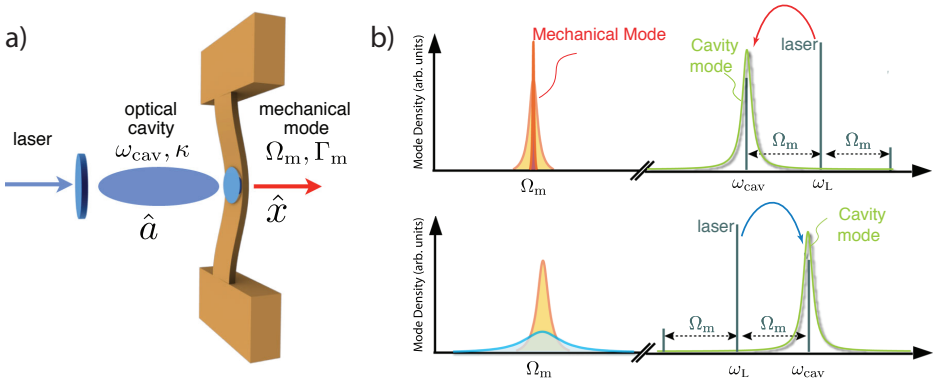

Figure 1.10: **Schematic of cavity optomechanics.** (a) The optomechanical system. (b) Blue (upper) and red (lower) sideband pumping. As shown, the mechanical resonance peak is either amplified or de-amplified depending on the frequency of laser light used. Taken from Ref. 15.

back phase by the frequency of laser light that is used in the optical cavity. Light at frequency $\omega_{\rm cav} + \Omega_m$ (termed the "blue sideband") leads to amplification, and light at frequency $\omega_{\rm cav} - \Omega_m$ (termed the "red sideband") leads to de-amplification. If x is undergoing thermally-driven motion, de-amplification is equivalent to cooling. Therefore the optical system can be used to decrease the thermal phonon occupancy n_m of the mechanical system, and cool it towards its quantum ground state.

For experiments in which a MEMS/NEMS device is coupled to a microwave resonant circuit, the circuit is exactly analogous to the optical cavity as described above. Identical "sideband" effects apply if energy is supplied to the microwave system at the corresponding frequencies.

A similar (albeit less efficient) means for of inducing optical feedback on motion is to utilize optical absorption. The scheme is similar to radiation pressure feedback: Laser light is incident on the MEMS device, as shown in Figure 1.11. A

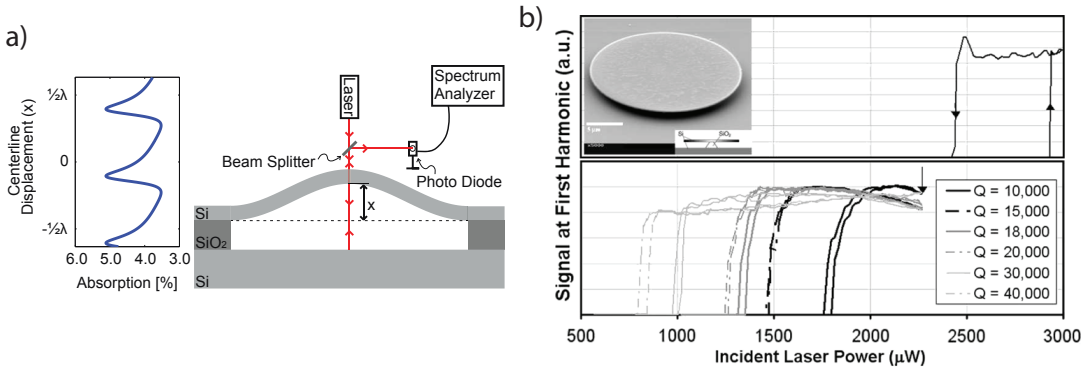

Figure 1.11: **The photothermal effect.** (a) Schematic of a buckled MEMS beam under laser illumination. Inset: the absorbed laser intensity versus displacement x. Taken from Ref. 16. (b) Photothermal self-oscillation in a MEMS disk. Plotted is the oscillation amplitude for several disks (of varying Q factors) versus incident laser power. Inset: SEM image of a MEMS disk; the disk is supported by a central pillar. Taken from Ref. 17.

weak (*i.e.* lossy) Fabry-Perot cavity is formed between the MEMS resonator and a silicon back-plane, leading to a light intensity profile similar to that shown in Fig. 1.11 (a). The MEMS resonator has a fixed optical absorption coefficient, and absorbed light leads to a temperature change within the resonator. Because of thermal expansion, this temperature change causes a position change. Therefore the feedback loop is as follows: Motion in x leads to a change in the absorbed laser power, which in turn applies a photothermal "force" F on x. Depending on the phase of this force, the photothermal effect can either amplify or de-amplify motion. Unlike the radiation pressure case, however, there are no sidebands that can be utilized to enhance the effect. Still, the photo-thermal effect benefits from its simplicity and the fact that it does not require a high-finesse optical cavity.

The photothermal effect has been demonstrated to cool a MEMS resonator

from 300 K to 30 K [41], and to amplify a MEMS resonator into self-sustaining oscillations [12, 17, 42]. This latter case is shown in Figure 1.11 (b). This effect thus offers a unique and robust way to manipulate mechanical motion using light, and can be a promising alternative to electrical feedback in MEMS/NEMS oscillators for timing applications.

1.4 Thesis Outline

This thesis is organized as follows:

- Chapter 1: **Introduction**.
- Chapter 2: **Graphene-coated high-Q silicon nitride resonators**. We present a study of graphene-coated silicon nitride membranes. The union of these two materials results in a mechanical system with large surface area, high quality factor, and motion that can be both manipulated and detected by electrical means. Moreover, optical absorption by the graphene offers a new means to influence the dynamics of this system. This work is published in Ref. 43.
- Chapter 3: **Tunable phonon cavity coupling in graphene membranes**. We demonstrate energy exchange between the vibrational modes of a suspended graphene membrane. This effect is mediated by a nonlinear coupling between the the membrane's tension and its displacement, and strengthened by our ability to experimentally tune the mode frequencies to a specific resonant condition. The result is a system in which one mechanical mode acts as an energy reservoir that can be tapped into to either

amplify or de-amplify the motion of another mode. This work is published in Ref. 44.

- Chapter 4: **Low-power photothermal self-oscillation of bimetallic nanowires**. We describe an experiment in which the motion of a tensioned nanowire is drastically affected by incident laser light. Optical absorption by the nanowire results in a feedback loop between its displacement and its temperature that can lead to mechanical self-oscillation. This photothermal effect has been previously observed in micro-mechanical systems, but with much higher laser powers needed for self-oscillation. We present a comprehensive theory to model this behavior, and unify previously existing competing theories in this field. This work has been submitted for publication; it is available online in Ref. 45.

- Chapter 5: **Temperature-dependence of graphene stress and elasticity**. We present measurements of graphene mechanics over a wide temperature range: 80K to 550K. By tracking the resonant frequency of a suspended graphene membrane as DC electrostatic forces are applied, we can extract its total mass, intrinsic tension, and elastic modulus. We observe temperature-dependent behavior that is consistent with a layer of polymer contamination on the graphene surface, and discuss the implications of such contamination. Understanding the temperature-dependence of these devices will be crucial for future device applications. This work is unpublished.

- Chapter 6: **Conclusions and outlook**

Chapter 2

Graphene-coated high-Q silicon nitride resonators

In this chapter we explore the resonant mechanics of high quality factor (Q) graphene-coated-silicon-nitride membranes using optical and electrical transduction schemes. With the addition of the graphene layer, we retain the desirable mechanical properties of silicon nitride but utilize the electrical and optical properties of graphene to transduce and tune the resonant motion by both optical and electrical means. By positioning the graphene-on-silicon-nitride drums in a tunable optical cavity, we observe position-dependent damping and resonant frequency control of the devices due to optical absorption by graphene.

This chapter is published in Ref. 43.

2.1 Motivation and Results

Resonant electromechanical systems [46, 47] and optomechanical systems [48] with high quality factors have been studied for applications such as ultrasensitive force measurements and displacement sensing at the quantum limit [48]. They have also found use in accelerometers and gyroscopes [49] and show promise for resonant sensing applications [50, 51]. Silicon nitride has desirable mechanical properties for microelectromechanical devices (MEMS) and is relatively simple to fabricate. Ultra-thin mechanical resonators made from silicon nitride have been explored for optomechanics [48], mass sensing [52], and force sensing [53] because of their high mechanical quality factors [54–56] ($Q > 10^6$), low masses, and low spring constants [48, 56]. Recently, it has been shown that membrane Q can be enhanced by the right choice of tensile stress, resonator size, mode shape, and optimized fabrication techniques [54, 55, 57]; quality factors of up to 4.4×10^6 can thus be achieved for a 15 nm thick silicon nitride membrane [54]. Such large area, ultra-thin tensioned membranes are useful as optomechanical elements [12, 48] whose mechanical degrees of freedom can be easily controlled using light [12, 48, 56]. However, because of the insulating nature of silicon nitride, some of the most desirable characteristics of these high-Q resonators can only be transduced optically. Electrical integration of these devices can be achieved through deposition of a thin conducting layer on the resonator surface. For metals, however, the thickness required to form a continuous layer results in significantly degraded Q and increased mass [58–60]. Metallization also adds complexity in terms of stresses associated with thermal expansion mismatch, causing the freestanding structures to bend or buckle.

Graphene has been widely studied because of its unique electronic [26], op-

tical [61], and mechanical properties [27]. Its light mass and strong optical absorption make it an ideal candidate for achieving optomechanical coupling [12]. Mechanical resonant devices have been constructed of monolayer graphene [9, 10, 30, 31, 62], but the mechanical quality factor, fabrication yield, and durability of these structures are limited. Hybrid silicon nitride-graphene (SiNG) devices that combine the properties of both materials would greatly expand the range of possible device applications, combining the desirable mechanical properties of silicon nitride with the electrical and optical properties of graphene. In this chapter, we demonstrate the electrical actuation of high stress silicon nitride membranes using monolayer graphene in a tunable Fabry-Perot cavity. We also present simultaneous detection of its resonant motion using both optical and electrical means enabling the comparison of the two detection schemes. Strong optical absorption in the atomic monolayer graphene [61] enables photothermal interaction with the high-Q silicon nitride membrane, with associated frequency and damping tunability due to tension modulation in the nitride. The electrical detection of this optical interaction over the entire cavity detuning (z/λ) range is useful to understand the photothermal processes [12] in these heterostructures; it enables us to decouple the resonant motion modulation due to optical absorption from the position-sensitive optical detection scheme. These frequency-tunable optically and electrically coupled systems have applications including oscillators, filters, and sensors [63–65]. Electrical integration of these high Q devices also enables us to understand mechanical nonlinearities [66–68] and provide greater scope for quantum control and cooling [69].

Silicon nitride-graphene square drums of side length $100\,\mu$m – $400\,\mu$m were fabricated using potassium hydroxide (KOH) etching of the backside of a silicon wafer. Chemical vapor deposition (CVD) grown graphene was transferred on

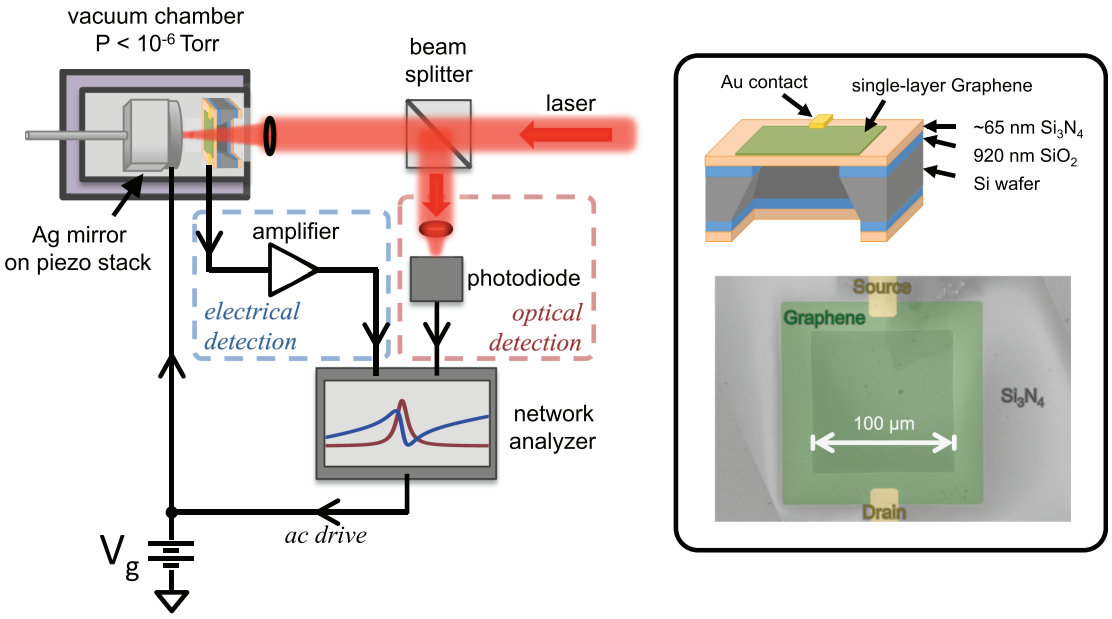

Figure 2.1: **Schematic of the experimental setup.** Variation in the reflected light from a Fabry-Perot cavity formed between a SiNG membrane and a piezo-controlled metallic mirror is monitored by a fast photodiode. A gate voltage, V_g, is applied between the graphene and the metallic mirror to actuate the resonator; this voltage has a DC component to tune the membrane tension and an AC component at the drive frequency. Measuring the capacitively coupled current provides a second means to read-out mechanical motion. Inset: Combined false-color scanning electron microscope (SEM) image and optical micrograph of a typical SiNG membrane resonator showing the device layout. Scale bar indicates the suspended region.

top of a wafer containing suspended drums and patterned using optical lithography. Electrical contacts to these resonators were defined by patterning metal leads (see Section 2.2.1). These graphene on silicon nitride devices are placed in close proximity to a piezo-controlled metallic mirror that forms a tunable optical cavity (see Section 2.2.2). Optical detection involves detecting the change in the reflected laser light as the membrane moves in the low finesse ($F \approx 1.2$)

optical cavity formed by the membrane and mirror as shown in Figure 2.1. The metallic mirror used in this cavity also acts as a conductive electrode which is placed in close proximity to the resonator ($< 60\,\mu$m), where we apply a bias voltage to actuate and tune the resonance of the SiNG membranes electrostatically under high vacuum conditions ($< 2 \times 10^{-6}$ Torr). A fast photodiode and a network analyzer are used to measure the time-varying component of our reflected optical signal. This detected signal is proportional to both the amplitude of the membrane's motion ($\tilde{z}(\omega)$) and the change in cavity reflectance ($R(z)$) with respect to membrane position (dR/dz) [70]. The amplitude of the capacitively driven membrane motion is given by

$$\tilde{z}(\omega) = -\frac{1}{m_{\text{eff}}}\frac{C_g}{d}V_g\tilde{V}_g\frac{1}{\omega_0^2 - \omega^2 + i\omega_0\omega/Q} \tag{2.1}$$

where $C_g = \epsilon_0 A/d$ is the membrane-mirror capacitance, m_{eff} is the membrane's effective mass, and A is the membrane area. $V_g, \tilde{V}_g$ are the DC gate voltage and AC drive voltage, respectively. $\omega_0 = 2\pi f_0$ and $\omega = 2\pi f$ are the membrane resonant frequency and the drive frequency, respectively. Our electrical detection scheme involves the capacitive detection of membrane motion (described in Section 2.2.3), and the observed signal ($\tilde{I}$) is given by $\tilde{I} = i\omega C_{\text{tot}}\tilde{V}_g - i\omega\frac{\tilde{z}(\omega)}{d}C_g V_g$. The first term here corresponds to the total capacitive background (C_{tot}), due to the device (~ 1.5 pf) and all parasitic capacitance (~ 5 pf). The second term is sensitive to membrane motion. The imaginary unit i reveals the phase relation between $\tilde{I}$ and $\tilde{V}_g, \tilde{z}$.

Figure 2.2 shows the typical gate tuning of the resonant frequency, where the composite membrane only shows capacitive softening [71] in the applied DC gate voltage range. At a given gate voltage, both optical and electrical resonant responses show a Lorentzian behavior (Figure 2.2 (d-e)), allowing us to extract the fundamental frequency ($f_0 = 2.8$ MHz), the full width at half maxi-

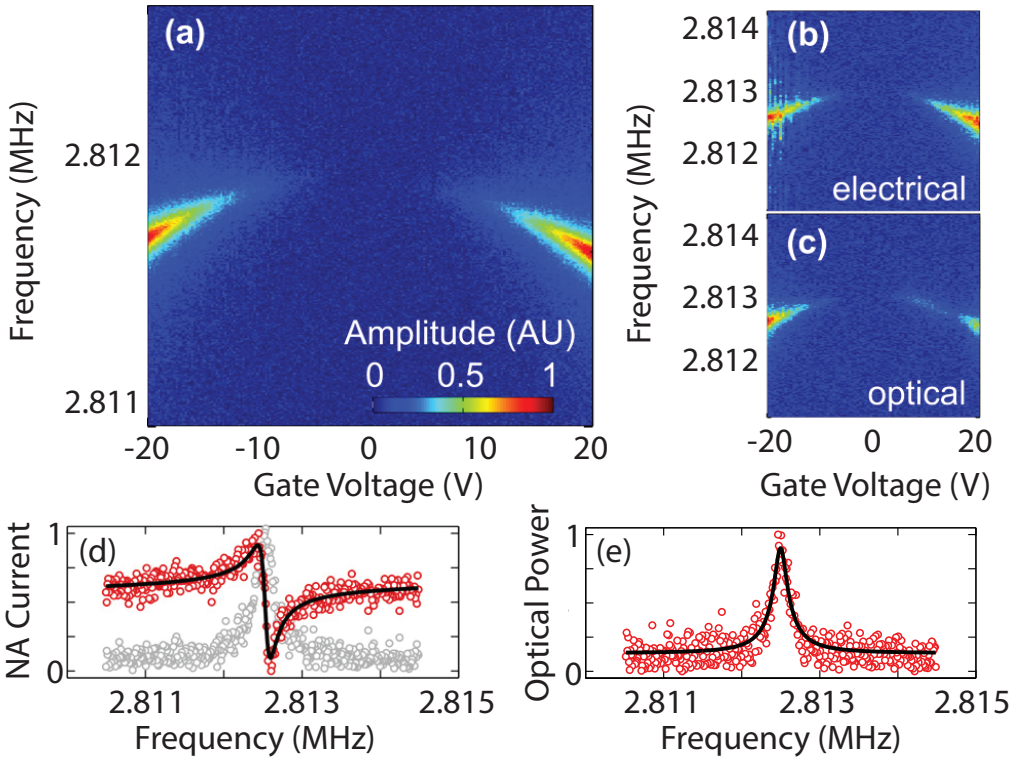

Figure 2.2: **Gate voltage tuning of the SiNG membrane resonant frequency.** (a) Tuning in a 100 μm membrane, detected using electrical means with zero laser power. Amplitude is in color scale. The resonator shows capacitive softening in the measured voltage range. Gate tuning detected using both electrical (b) and optical (c) means at 100 μW laser power. (d) Sample of raw electrical readout data with fit. Gray data points show the same data with the parasitic capacitance contribution subtracted, illustrating the Lorentzian signal as it appears in the color of (a) and (b). (e) Sample of optical readout data with fit. Fits give $f_0 = 2.8$ MHz and $Q = 17\,000$.

mum Γ, and the quality factor ($Q = f_0/\Gamma$) of the device. Electrically and optically detected signals give identical Q and resonant frequency measurements (within fitting errors). For the fundamental mode of a tensioned square drum, the resonant frequency is given by $f_0 = \frac{1}{L}\sqrt{\frac{\sigma}{2\rho}}$, where σ, ρ, L are stress, density, and side length of the resonator, respectively. This yields a tensile stress of 475 MPa in our 100 μm membrane. As such, quality factors of thin tensioned membranes

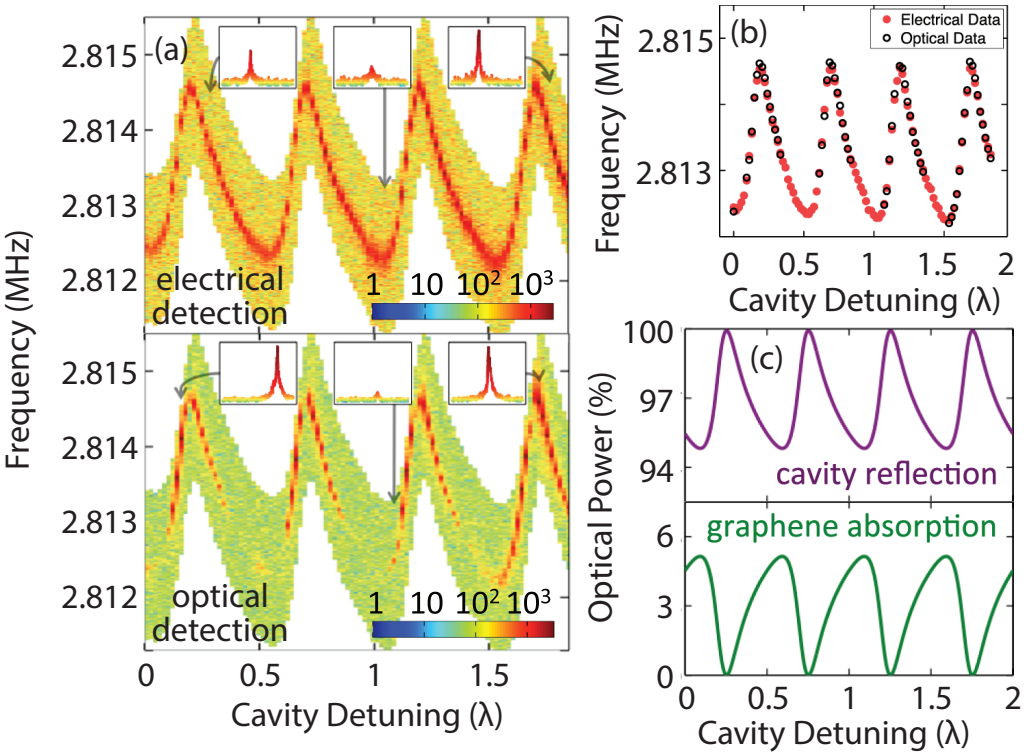

Figure 2.3: **SiNG membrane resonant frequency vs. mirror position.** (a) Electrical and optical detection of resonant frequency as a function of detuning of the cavity. Color scale indicates the amplitude of motion in log scale. While the electrical signal is continuous (capacitive background is subtracted from the data), there are positions in the cavity where optical signal disappears (dR/dz vanishes). (b) Overlaid resonance frequencies from fits of the electrical and optical readout data shown in (a). (c) Calculated reflectance of the optical cavity (upper panel) and absorption (lower panel) by graphene as a function of detuning of the cavity.

scale approximately linearly with the aspect ratio (side length/thickness) [54]. We have measured quality factors of up to ~ 70 000 for a 100 μm graphene-on-silicon-nitride drum for the fundamental mode. A similar 300 μm membrane yields Q ~ 250 000. Graphene contributes marginally to the observed mechanical damping of these structures [72].

Figure 2.3 shows the optically- and electrically-detected resonant frequency

response as the optical cavity is detuned by stepping the piezo-controlled mirror toward the membrane at a fixed incident laser power (0.2 mW). The disappearance of the optical readout signal corresponds to the positions in the cavity where dR/dz vanishes. We see a corresponding phase change in the optically detected signal (see Figure 2.9 in Section 2.2.5). The electrically detected signal is continuous and shows an overall increase in signal as the mirror approaches the membrane (Figure 2.6 in Section 2.2.3). The optical detection scheme results in a better signal to noise ratio except near the points where the cavity reflectivity is close to its turning point. However, optical detection also is responsible for the associated photothermal interaction resulting in periodic variations in the resonant frequency. We model this interaction by calculating the cavity reflectance $R(z)$ and graphene absorption $A(z)$ (Figure 2.3 (c)) in the cavity using a standard transfer matrix approach (Section 2.2.4). $A(z)$ in these calculations exceeds the well known value of $\pi\alpha \approx 2.3\%$ due to the cavity effect, and the asymmetric cavity response is caused by reflections within the nitride layer. The slight offset of the nodes (corresponding to $dR/dz = 0$) in the optically detected signal relative to the frequency extremes is indicative of additional losses in the cavity – attributed here to absorption by the Ag mirror. Figure 2.4 (a) shows the electrically-obtained resonant frequency as a function of mirror position for several values of the incident laser power, with corresponding fits based on the calculated optical absorption of graphene in our system (Figure 2.3 (c)). Nodal positions in the optical data were used to determine several cavity parameters in these fits based on dR/dz (see Section 2.2.5). We observe that the magnitude of the frequency variation (defined as the peak-to-peak frequency shift) scales linearly with incident laser power (shown in Figure 4(b)).

Both optically- and electrically-obtained data suggest that the mechanism

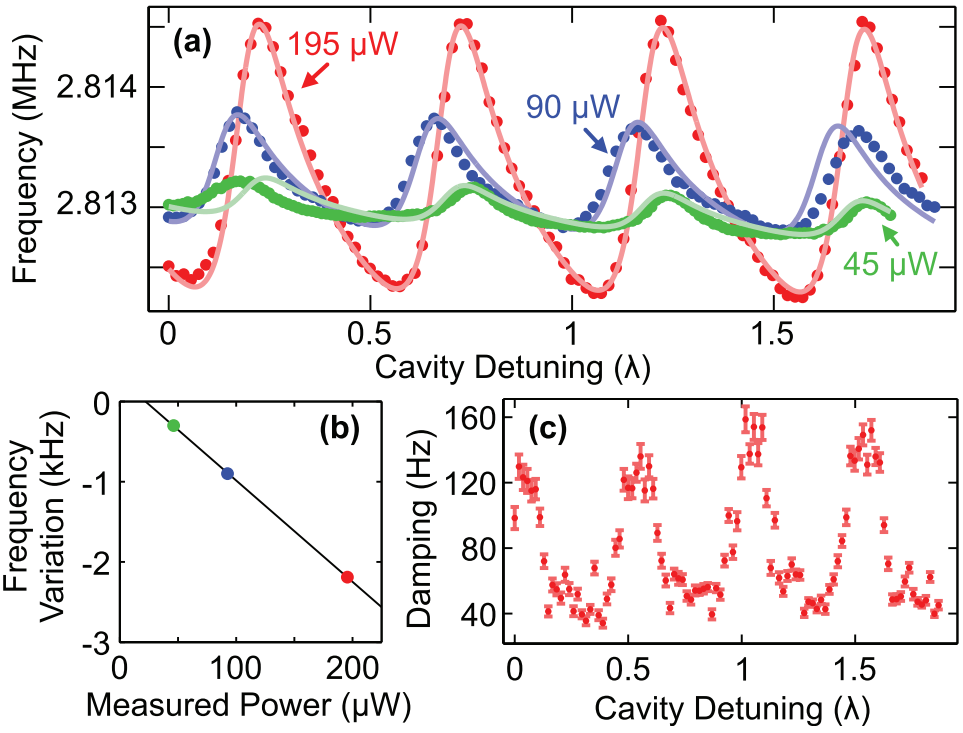

Figure 2.4: **Membrane frequency and damping vs. incident laser power and cavity detuning.** (a) Resonant frequency measured by electrical detection. Oscillations in the frequency are associated with optical absorption by the graphene and its effect on the tensile stress of the bilayer membrane. (b) Maximum frequency variation of the device as a function of incident laser power, with a linear fit. (c) Measured damping shifts at 195 μW laser power, in part due to the photothermal feedback on the membrane.

responsible for resonant frequency shifts in our devices is local heating in the membrane resulting from optical absorption by the graphene. Such heating leads to a lowering of the membrane's tensile stress through thermal expansion of the silicon nitride. In the low optical power limit, this results in a frequency shift that varies with temperature as $\frac{\Delta f}{f_0} = -\frac{E_{\mathrm{SiN}}\alpha_{\mathrm{SiN}}\Delta T}{2\sigma}$, where E_{SiN} and α_{SiN} are the Young's modulus and thermal expansion coefficient of nitride, and ΔT is the temperature shift due to optical heating. The numerator in this expression is

the change in tension caused by expansion of the nitride and ignores contributions from graphene contraction since the graphene thickness is small compared to silicon nitride and has minimal affect on the overall mechanics. To lowest order, the temperature rise can be approximated by assuming a circular membrane and solving for the equilibrium heat flow radially outward from the laser spot. Including heat dissipation through both the graphene and the nitride, the steady state temperature difference between the membrane edge and the laser spot is $\Delta T = \frac{P_{\mathrm{abs}}}{t_{\mathrm{SiN}} k_{\mathrm{SiN}} + t_{\mathrm{G}} k_{\mathrm{G}}} \times \frac{\ln(L/D)}{2\pi}$. Here, P_{abs} is the absorbed optical power and D is the laser spot diameter. $t_{\mathrm{SiN}}, t_{\mathrm{G}}$ are the thicknesses of the two materials, and $k_{\mathrm{SiN}}, k_{\mathrm{G}}$ are the thermal conductivities ($30\,\mathrm{W/m\,K}$ for nitride and $5 \times 10^3\,\mathrm{W/m\,K}$ for graphene). With a laser spot diameter of $\sim 8\,\mu$m, graphene absorption of 5% inside the cavity (see Figure 2.3 (c)), and incident power of $195\,\mu$W, we thus expect a temperature rise of $\sim 1.3\,$K. This results in a maximum frequency variation of $\Delta f = -2.7\,$kHz, which is an overestimate (in magnitude) since we have taken the mean membrane temperature to be that directly at the laser spot. This is, however, in excellent agreement with the measured frequency variation of $-2.2\,$kHz (Figure 2.4 (b)).

While the optical signal strength exhibits variations primarily due to its dependence on dR/dz, the electrical signal amplitude shows periodic variations (see Figure 2.11 in Section 2.2.6) mainly due to changes in the effective damping of the resonator (Figure 2.4 (c)). In the absence of the incident optical illumination, no such variations are observed. Such damping variations resulting from photothermal forces have been observed in bilayer materials [42, 73] and tensioned graphene drums [12]. Similar effects are possible in our system, with local bimetallic expansion of the membrane breaking the system symmetry and applying a feedback force in the direction of motion. Such a force would be

time-delayed by the membrane thermal relaxation time and would affect both device frequency and damping. Estimates of this time constant ($\omega\tau \sim 2\,000$) indicate that this effect would play a significant role in damping variations but would have a negligible effect on the frequency (see Section 2.2.6). This model predicts an effective damping [42, 73] of $\Gamma_{\text{eff}} = \Gamma\left(1 + Q\frac{\omega\tau}{1+\omega^2\tau^2}\frac{\nabla F}{K}\right)$, where K is the membrane spring constant and ∇F is the gradient in the bilayer force (w.r.t. mirror position) experienced by the membrane. The expected damping shift should thus vary as $dA(z)/dz$. However, such a model was found to have systematic deviations from our measured damping shifts (Figure 2.10). Thus, this is likely not the only mechanism influencing the damping of our devices, and further studies, including influence of nonlinearities [67, 68], are required to understand the feedback forces in these heterostructures.

2.2 Methods

2.2.1 Fabrication of graphene on silicon nitride drums

SiNG device fabrication began with growth of 900 nm thick thermal oxide (wet oxide, 980°C) on a double-side-polished silicon wafer. This oxide provides electrical isolation and etch isolation from a potassium hydroxide (KOH) etch. Stoichiometric high-stress silicon nitride (60 nm thick) was then deposited on the thermal oxide at 800°C. Square openings were patterned on the backside of the wafer using contact lithography (EV 620). This was followed by a reactive ion etch (CHF_3/O_2 nitride etch chemistry) recipe to etch both the nitride and oxide. Resist on the wafer backside was removed using Shipley 1165 solution (N-methyl-2-pyrrolidine). Exposed silicon was etched using KOH until the etch stopped – *i.e.* until the silicon was completely consumed and the oxide interface was reached on the front side of the wafer. Separately, monolayer graphene was grown on copper (Sigma Aldrich, 99.8%) using a chemical vapor deposition process [28] (980°C anneal in 60 sccm H_2 for 1 hour, graphene growth in 60 sccm H_2, 36 sccm CH_4 for 30 minutes at 980°C, followed by cool down to room temperature at 60 sccm H_2). CVD-grown graphene was coated with 50 nm of polymethyl methacrylate (PMMA). The copper substrate was then removed using a ferric chloride solution, and the graphene was transferred into several DI water baths before transferring onto the final substrate containing square silicon nitride drums on oxide.

After transfer, the graphene was patterned to localize it to a small region around the suspended silicon nitride drum (with the underlying oxide still present). The resist and PMMA were removed using 1165 solution. Graphene

was then annealed at 325°C for 3 hours using a forming gas mixture (CH_4 and Ar, 50% each at 1 L/min) to remove any residual resist. Gold electrical leads (60 nm thick with 2 nm Ti adhesion layer) were patterned on the graphene-coated silicon nitride wafer followed by lift-off in 1165 solution. The wafer was then spin-coated with photo-resist (SPR 700) to protect the front side, followed by a BOE (6:1) etch for 20 minutes to remove the oxide underneath the silicon nitride. Any remaining resist was removed using 1165.

Silicon nitride square drums with side length (L) of 100 μm to 400 μm (in increments of 100 μm) were fabricated per die using this method. Samples were diced and each resonator was current-annealed to yield a typical resistivity of 5 kΩ/square. Electrical contact was made to the on-chip source and drain electrodes using a wire bonder.

2.2.2 Experimental setup

Our custom-built tunable cavity setup involves a 3-axis Thorlabs piezo mirror mount (ASM 003) placed on an aluminum base, which is mechanically connected to a micrometer for coarse positioning (Figure 2.5). The micrometer resolution is 10 μm, whereas the piezo transverse resolution is 10 nm. The total piezo transverse travel is 7 μm.

The piezo mirror mount has both coarse (total travel $\sim$ 2°) and fine (total travel 2 arc minutes) tilt controls via mechanical screws and 3-axis piezo actuation respectively. This piezo can hold a 7 mm diameter silver mirror (Thorlabs PF03-03-P01). The mirror is mounted on a custom mirror mount that accepts a coax connector (Molex) and allows the mirror to be very close to the sample

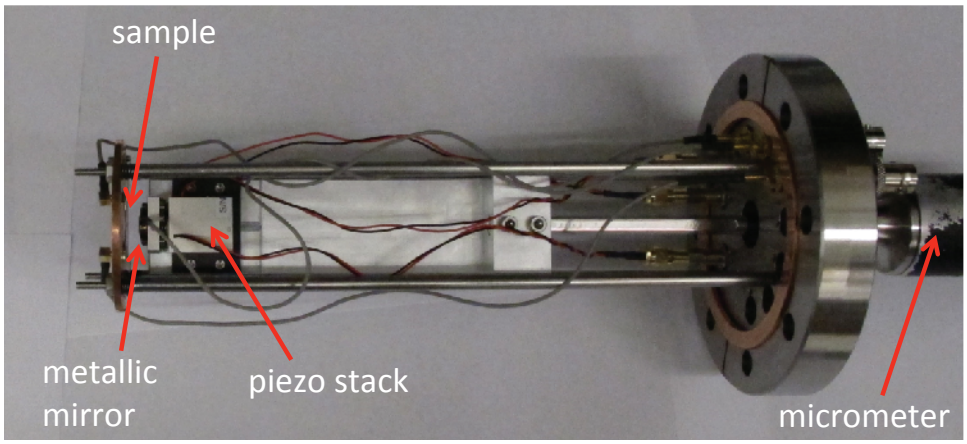

Figure 2.5: **Optical image of the custom-built tunable cavity set up.** A micrometer (Huntington Mechanical Laboratories, SN# VF-108) holds an aluminum support piece on which the piezo-controlled mirror is mounted for fine motion. The sample is mounted on an adjustable copper plate supported by steel rods. The whole assembly is mounted on a 4.5-inch flange with external feed-throughs for electrical connection.

($< 60\,\mu$m). The metallic mirror is electrically connected to a co-ax connector using conductive epoxy.

The sample is mounted on a copper plate using phosphor bronze springs which result in minimal mechanical drift. Source and drain are wire-bonded to co-ax connectors (Molex) in the copper plate. The copper plate rests on 4 steel rods and can also be tilt-adjusted using set screws. Source, drain, and gate electrodes are connected to external feed-throughs on a 4.5-inch flange using copper co-ax cables. The sample and mirror are made parallel to each other using optical means before sealing the chamber. The sample is oriented such that graphene faces the metallic mirror. The whole assembly is placed in a vacuum chamber that can reach 2×10^{-7} Torr and vacuum is maintained using an ion pump for vibration isolation. A DC+AC bias is applied to the mirror and an AC response through the drain is fed into a voltage amplifier followed by a net-

work analyzer. To minimize the parasitic capacitance, membrane resonators (4 per die) along with the electrical leads are positioned such that they are close to the edge of the metallic mirror. Similarly, optical response is read through a fast photo-detector using a network analyzer.

2.2.3 Electrical data fitting

In order to obtain reliable mechanical parameters for our resonators, a satisfactory model of the frequency response of our system is needed. As mentioned in Section 2.1, DC and AC voltage biases are applied to the membrane to drive it into mechanical motion. In the case of optical detection, a photodiode captures light reflected from the membrane-mirror cavity, and the measured signal amplitude resembles a standard Lorentzian response in frequency space. For electrical detection, however, the measured signal amplitude is non-Lorentzian. This is due to the many non-resonant components of the current in our circuit. As previously mentioned, the AC current through our device is

$$\tilde{I}(f) = i2\pi f C_{\text{tot}} \tilde{V}_g - i2\pi \frac{\tilde{z}(f)}{d} C_g V_g \tag{2.2}$$

where $\tilde{z}(f)$ is the membrane displacement, d is the membrane-mirror distance, and $V_g, \tilde{V}_g$ are the DC and AC voltages applied. C_g and C_{tot} are the membrane-mirror capacitance and the total (device + parasitic) capacitance, f is the drive frequency, and $i = \sqrt{-1}$. Because the linear background changes with the membrane-gate electrode distance, subtraction of this non-resonant current from the measured signal can be especially useful in analyzing membrane dynamics. Figure 2.6 shows the measured electrical signal as a color plot, before and after subtraction of the non-resonant background signal.

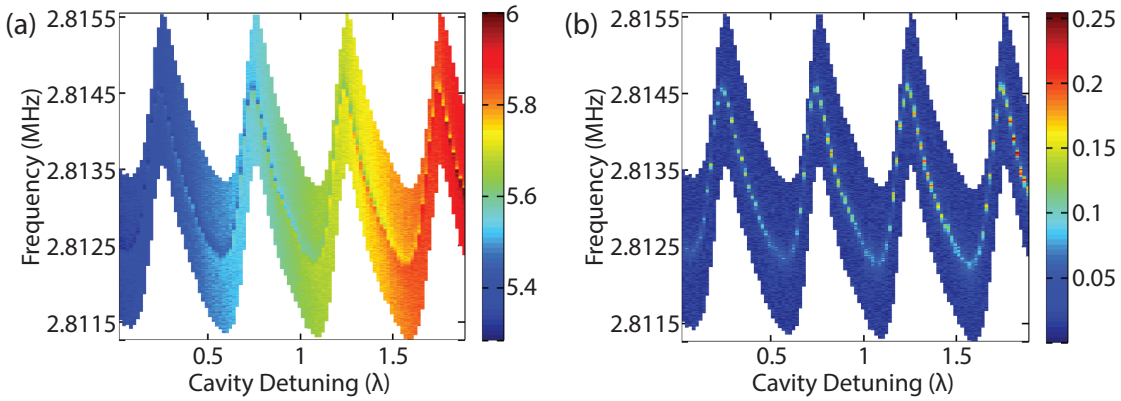

Figure 2.6: **Electrical signal before and after background subtraction.** (a) Raw amplitude of our measured signal as a function of drive frequency and mirror position with 0.195 mW incident power. Color denotes signal strength in mV. Note the increasing background and resonant signal as the capacitance of the system increases. (b) Amplitude of the same data (in mV) after background subtraction. Note the uniform background level and prominent resonance.

2.2.4 Modeling the optical cavity

Understanding the distribution of laser light intensity in our system is useful in the interpretation of our cavity detuning measurements. Shifts in the resonant frequency of our device (as seen in Figure 2.6) are directly related to the optical power incident on the graphene monolayer, and signal strength in our optically detected data is similarly related to the power reflected from our cavity. We have implemented a well-established transfer matrix approach [74] to model our optical system. A schematic of our cavity is shown in Figure 2.7.

Each interface and homogeneous region of light propagation can be modeled

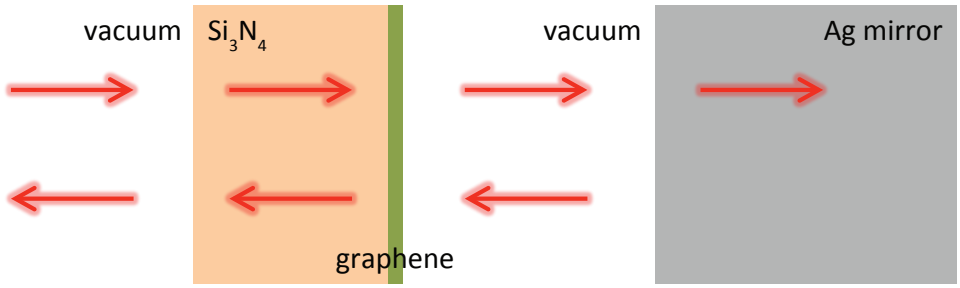

Figure 2.7: **Schematic of our optical cavity.** Far left: Incident laser beam and overall reflected beam. Far right: Overall transmitted beam (absorbed by Ag mirror). Red arrows indicate reflected and transmitted beams in each region of the cavity.

by a 2×2 matrix. For clarity, these are:

$$\begin{bmatrix} E_{1+} \\ E_{1-} \end{bmatrix} = \frac{1}{\tau} \begin{bmatrix} 1 & \rho \\ \rho & 1 \end{bmatrix} \begin{bmatrix} E_{2+} \\ E_{2-} \end{bmatrix} \tag{2.3}$$

Interface between two media

$$\begin{bmatrix} E_{1+} \\ E_{1-} \end{bmatrix} = \begin{bmatrix} e^{ikl} & 0 \\ 0 & e^{-ikl} \end{bmatrix} \begin{bmatrix} E_{2+} \\ E_{2-} \end{bmatrix} \tag{2.4}$$

Propagation through a homogeneous medium

Above, E_{1+}, E_{1-} are the electric field strength for right-going and left-going optical plane waves before an interface (or spatial propagation), and E_{2+}, E_{2-} are the corresponding waves after the interface (or spatial propagation). ρ, τ are the interface reflection and transmission coefficients, and k, l are the wavenumber and distance traveled. Matrices such as these are applied in succession to find the field in any region of the cavity.

In order to avoid issues with multiple reflected waves within the graphene layer, it was treated as an infinitely thin conducting interface rather than a thin film. To determine the transfer matrix for propagation across the graphene inter-

face, boundary conditions for the E and B fields (governed by Maxwell's equations) were used. In short, E fields parallel to the interface are conserved across it, while B fields experience a discontinuity proportional to the free current density of the graphene. Written in matrix form, these are restated as:

$$\begin{bmatrix} E_2 \\ cB_2 \end{bmatrix} = \begin{bmatrix} 1 & 0 \\ -\mu_0 c\sigma & 1 \end{bmatrix} \begin{bmatrix} E_1 \\ cB_1 \end{bmatrix} \tag{2.5}$$

where E_1, B_1 are the total fields before the graphene, and E_2, B_2 are the total fields after. μ_0, c, and σ are the vacuum permeability, speed of light in vacuum, and graphene conductivity. Taking n_1, n_2 to be the refractive indices of the two surrounding media, we can write this relation in terms of the left- and right-going waves as:

$$\begin{bmatrix} E_{1+} \\ E_{1-} \end{bmatrix} = \frac{1}{2n_1} \begin{bmatrix} n_1 + n_2 + \mu_0 c\sigma & n_1 - n_2 + \mu_0 c\sigma \\ n_1 - n_2 - \mu_0 c\sigma & n_1 + n_2 - \mu_0 c\sigma \end{bmatrix} \begin{bmatrix} E_{2+} \\ E_{2-} \end{bmatrix} \tag{2.6}$$

Transfer matrix for a graphene interface

If we now use the universal constant $\pi e^2/2h$ for the conductivity of Dirac fermions in graphene [75, 76], the combination $\mu_0 c\sigma$ simplifies to $\pi\alpha \approx 0.023$, the well-known opacity of graphene [61]. From Equation 2.6, we can thus extract the expected optical transmittance $T_G = (1 + \pi\alpha/2)^{-2}$ and reflectance $R_G = \pi^2\alpha^2 T_G/4$ of freestanding graphene, consistent with Ref. 61.

The relevant optical quantities needed to interpret our data are the optical power absorbed by the graphene membrane $A(z)$ and the total power reflected from our system $R(z)$ (as functions of the membrane-mirror distance). If we assume the mirror to be semi-infinite, we can readily compute the total reflected power and the total power absorbed by the mirror (normalized by the incident laser power) using the matrix approach described above. Of course, these are

functions not only of the membrane-mirror distance, but also the Si_3N_4 refractive index, Si_3N_4 thickness, and the complex refractive index of the mirror. Because the Si_3N_4 is considered to be lossless, any remaining optical power that is neither reflected out of the cavity nor absorbed by the mirror can be attributed to absorption by the graphene. The results of these calculations (for a given set of Si_3N_4 and mirror refractive indices) are shown in Figure 2.8.

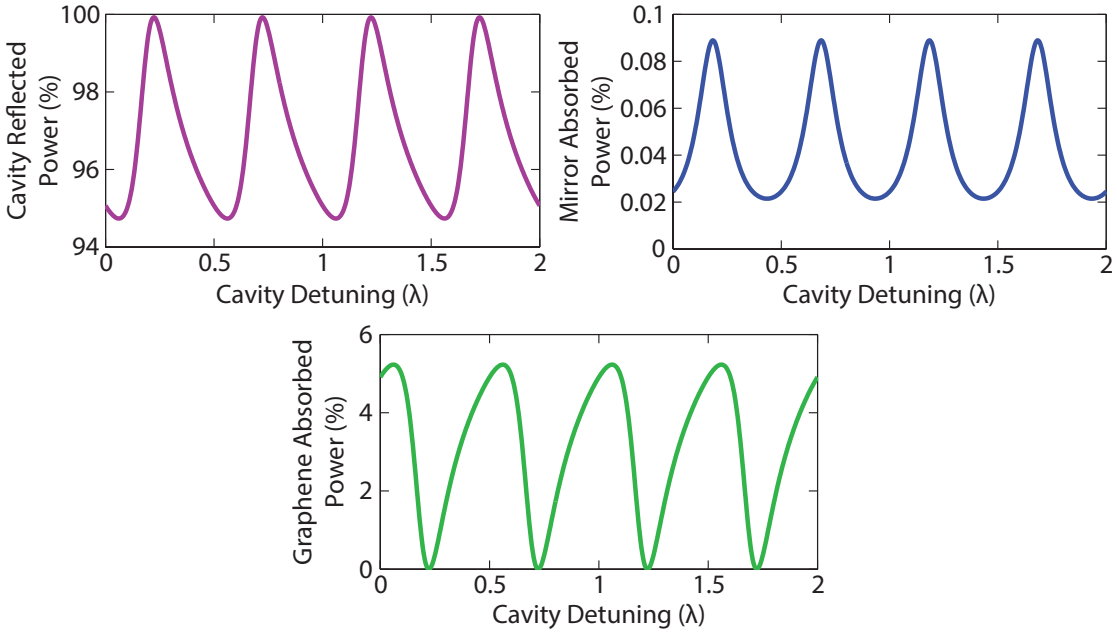

Figure 2.8: **Calculations of the laser power in different regions of our optical cavity.** Percentage of the incident laser power that is: (a) reflected out of the cavity, (b) absorbed by Ag mirror, and (c) absorbed by graphene, as predicted using the transfer matrix approach. The parameters used are: $n_{\mathrm{SiN}} = 1.5$, $n_{\mathrm{mirror}} = 0.001 - 2.8i$, and SiN thickness of 70 nm.

2.2.5 Fitting of cavity detuning data

With the calculations described above for the power in our optical cavity, a fitting model was generated for our resonant frequency vs. cavity detuning data. At high incident laser powers ($> 200\,\mu$W) the resonant peak becomes unstable due to optical absorption; for this reason only data obtained at lower laser powers has been used for analysis. The resonant frequency shifts were assumed to scale negatively with the optical power absorbed by the graphene layer – consistent with a tensile stress reduction due to thermal expansion of the bilayer membrane. In order to produce realistic optical parameters for our fit (refractive indices of the Si_3N_4 and the mirror), the amplitudes of our optically detected data were utilized. Nodal positions in the optical data correspond to cavity detunings at which the gradient of the reflected light vanishes ($dR/dz = 0$). Assuming small membrane deflections (relative to the optical wavelength), the signal amplitude scales linearly with $|dR/dz|$, as shown in Figure 2.9. The signal amplitude, however, is also affected by photothermal enhancement of the device Q, so only nodal positions are truly reliable.

2.2.6 Fitting of damping shift with cavity detuning

For low-finesse cavities, radiation pressure plays a negligible role on resonator mechanics, but photothermal forces cannot be discounted. The effective change in resonant frequency and damping due to a photothermal feedback force (as

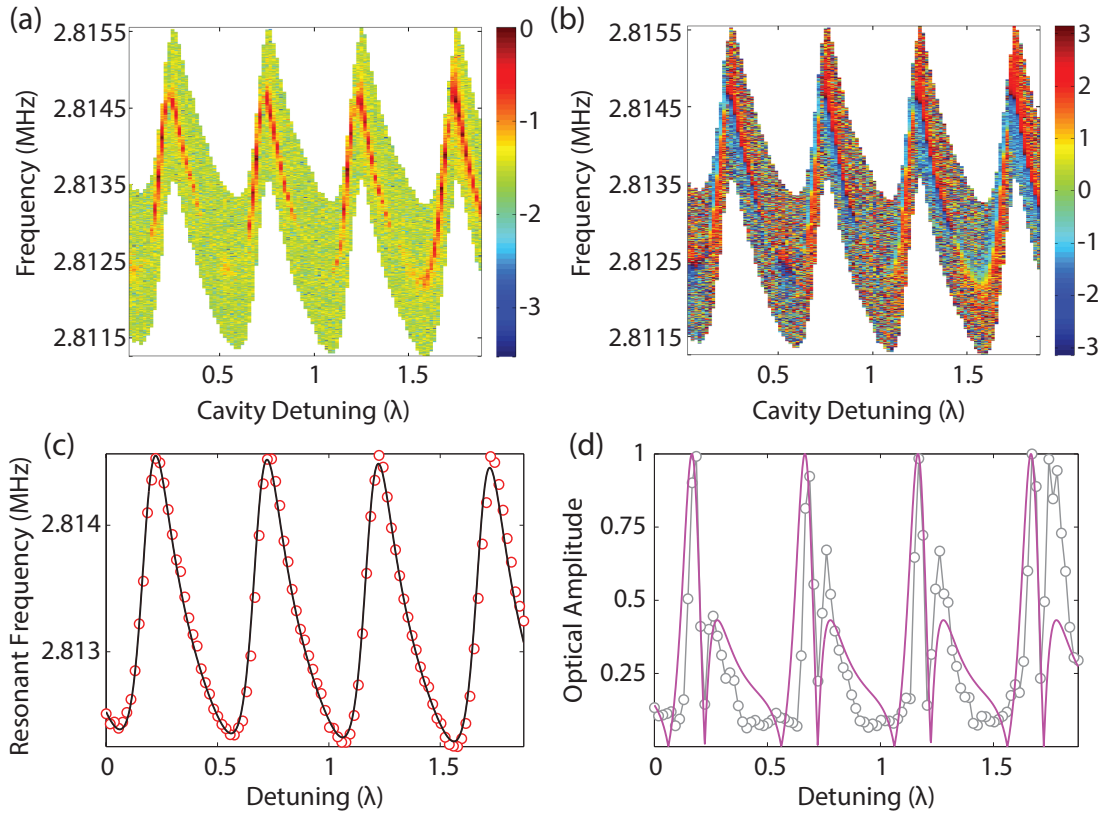

Figure 2.9: **Fits of the cavity detuning data.** (a) Optically-detected signal at 0.195 mW incident power. Color scale denotes $\log_{10}$ of the normalized signal amplitude. (b) Phase of the optical data in (a). Nodes in the optical signal are accompanied by 180°phase shifts. (c) Electrically-detected resonant frequency vs. cavity detuning. Fit parameters include a sloping background to account for capacitive softening of the resonator as the membrane-mirror distance decreases. (d) Normalized amplitude of the optical signal vs. cavity detuning. Fit scales with absolute value of the gradient in the reflected optical power. Note the agreement in nodal positions between the data and fit.

described in Refs. 42, 73) are given by:

$$\Gamma_{\text{eff}} = \Gamma\left(1 + Q\frac{\omega\tau}{1+\omega^2\tau^2}\frac{\nabla F}{K}\right) \tag{2.7}$$

$$\omega_{\text{eff}}^2 = \omega^2\left(1 - \frac{1}{1+\omega^2\tau^2}\frac{\nabla F}{K}\right) \tag{2.8}$$

Here, ∇F is the photothermal spring constant and is proportional to the gradient of the absorbed laser power ($\nabla F \propto dA/dz$). K is the spring constant of the resonator and $\tau = L^2\left(\rho_{\mathrm{SiN}} C_{\mathrm{SiN}} t_{\mathrm{SiN}} + \rho_g C_g t_g\right)/4\left(\kappa_{\mathrm{SiN}} t_{\mathrm{SiN}} + \kappa_g t_g\right)$ is the relaxation time [42, 73, 77] associated with the heat flow. We find that $\omega\tau = 2000$ for our resonator ($\omega = 17.6\,\mathrm{MHz}$, $L = 100\,\mu\mathrm{m}$). Here, we used $\rho_{\mathrm{SiN}} = 3000\,\mathrm{kg/m^3}$, $\kappa_{\mathrm{SiN}} = 30\,\mathrm{W/m\,K}$, $t_{\mathrm{SiN}} = 60\,\mathrm{nm}$, $C_{\mathrm{SiN}} = 700\,\mathrm{J/kg\,K}$ for silicon nitride, and $\rho_g = 2330\,\mathrm{kg/m^3}$, $\kappa_g = 3000\,\mathrm{W/m\,K}$, $t_g = 0.33\,\mathrm{nm}$, $C_g = 750\,\mathrm{J/kg\,K}$ for graphene. Such a large time constant results in a negligible shift in the resonant frequency of the resonator and hence the observed frequency shifts can be attributed to static absorption-induced stress rather than the optomechanical forces. However, observed changes in the mechanical damping can still be attributed to the absorption-dependent back action, the nature of which is still to be understood. Using the same optical parameters as Figures 2.8 & 2.9, this model produces a fit to the damping which is shown in Figure 2.10 (a). As can be seen in the figure, the data displays systematic deviations from the photothermal model. This is particularly true at high damping, where the data and model appear to be out of phase. Interestingly, the damping data seems to be 180°out of phase with the frequency tuning data (Figure 2.9 (c)). For this reason, we have also considered a damping model that scales with the graphene-absorbed power (Figure 2.10 (b)). While this fit seems in phase with the damping data near the maxima, it does not match the experiment well at low and intermediate values. A damping model that is a sum of these two contributions has also been considered (Figure 2.10 (c)), but still does not agree with experiment.

The complications in modeling the measured damping fits can arise from several sources. For extremely sharp resonances, for example, limited data point sampling near the peak frequency may affect the measured damping. It should

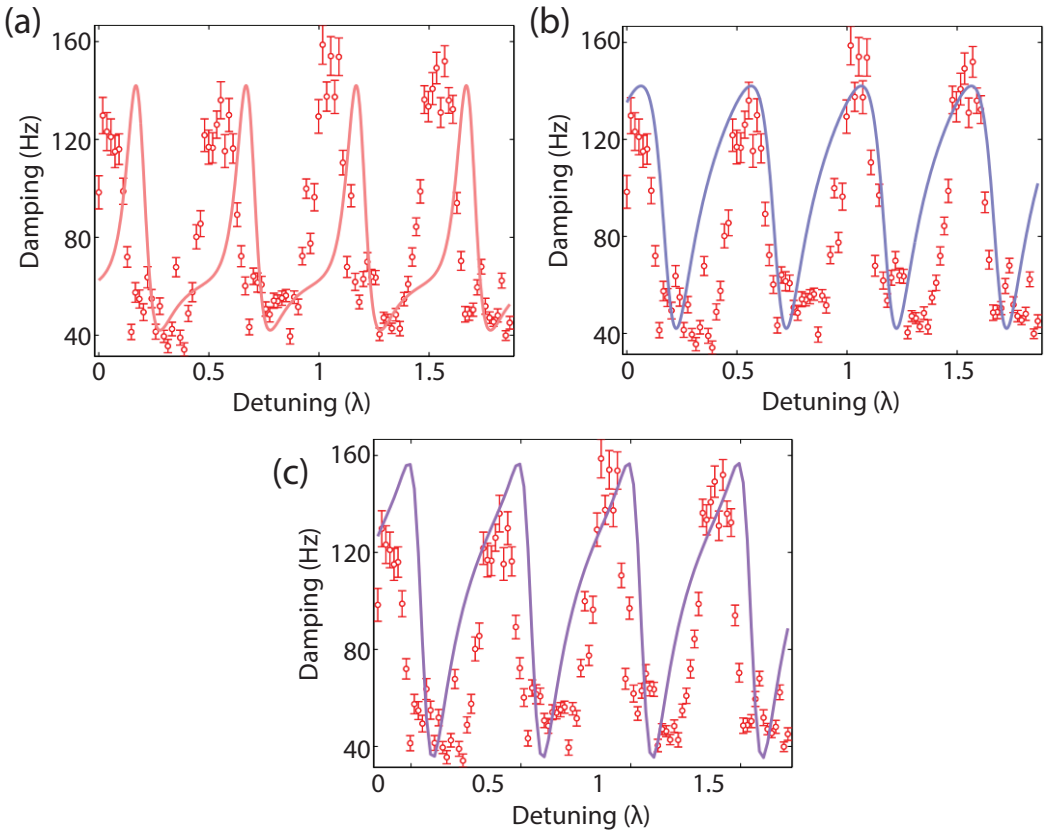

Figure 2.10: **Damping variations at 0.195 mW with various fitting models.** (a) Photothermal feedback fit, proportional to the gradient in the graphene-absorbed laser power. (b) Damping data with a fit proportional to the graphene-absorbed power. (c) Damping with a fit that is a sum of the two contributions from (a) and (b). These figures use optical parameters identical to those in Figures 2.9.

be noted that the error bars appearing in Figure 2.10 are based only on the goodness of the Lorentzian fits, and are not representative of all possible sources of uncertainty in the damping. Despite these issues in modeling the damping, the presence of a reproducible, optically-induced feedback force in our system is unmistakable. This effect on the damping is also seen in the amplitude of our electrically measured signal, as shown in Figure 2.11.

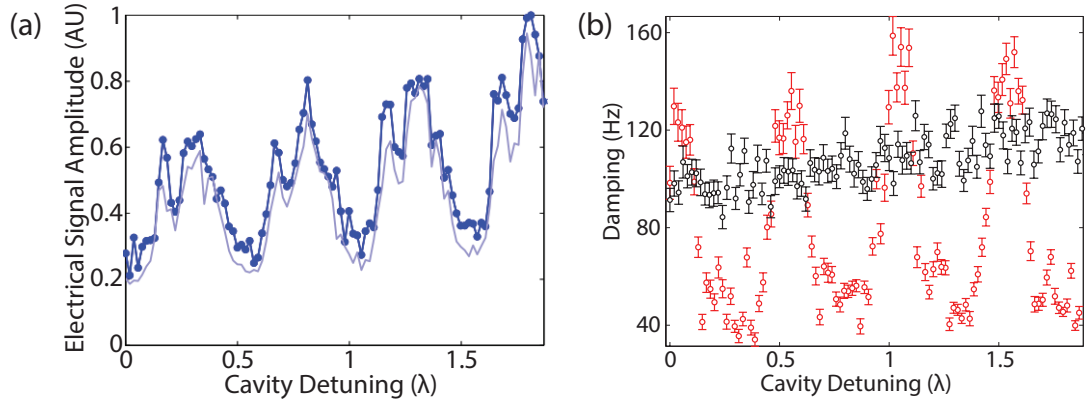

Figure 2.11: **Amplitude of electrically detected SiNG motion.** (a) Electrical signal amplitude as the membrane-mirror distance decreases. Note the periodic oscillations that scale with 1/damping. Dark blue points indicate amplitude data maxima (after subtraction of parasitic capacitance contribution). A light blue line indicates the measured amplitude arising from Lorentzian fits. (b) Damping with 0 mW laser power (black) compared to 0.195 mW laser power (red).

2.2.7 300 μm device response

All of the results shown thus far are for a 100 μm graphene-on-silicon-nitride membrane. Figure 2.12 shows the optically-detected response of a 300 μm graphene-on-silicon-nitride membrane of similar geometry (and identical thickness) to the 100 μm device depicted in Figure 2.1. The high Q is in line with that expected of a 300 μm SiN membrane of this tension. This suggests that (aside from optomechanics) the graphene has a minimal effect on the damping and the overall device mechanics.

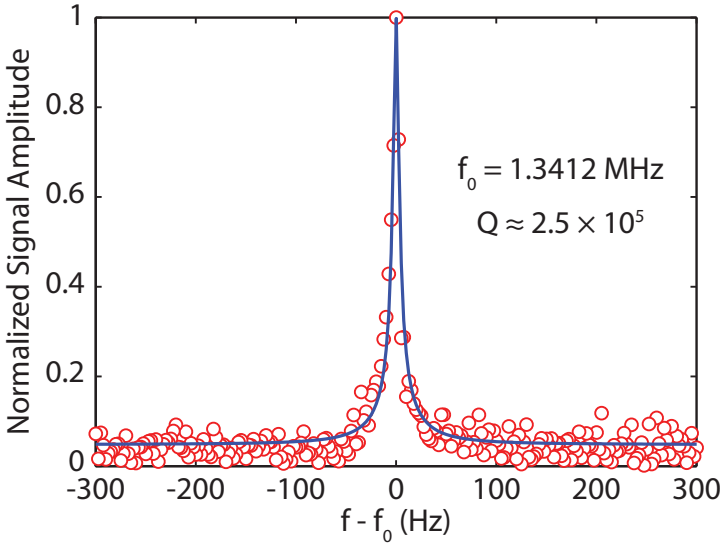

Figure 2.12: Optically detected resonant response of a 300 μm device.

Chapter 3

Tunable phonon cavity coupling in graphene membranes

3.1 Introduction

A major achievement of the past decade has been the realization of macroscopic quantum systems by exploiting interactions between optical cavities and mechanical resonators [5, 78, 79]. In these systems, phonons are coherently annihilated or created in exchange for photons. Similar phenomena have recently been observed through "phonon cavity" coupling – energy exchange between modes of a single system as mediated by intrinsic material nonlinearity [80, 81]. To date, this has been demonstrated primarily for bulk crystalline, high-quality-factor ($Q > 10^5$) mechanical systems operated at cryogenic temperatures. Here we propose graphene as an ideal candidate for the study of such nonlinear me-

chanics. The large elastic modulus of this material and capability for spatial symmetry breaking via electrostatic forces is expected to generate a wealth of nonlinear phenomena [82], including tunable inter-modal coupling. We have fabricated circular graphene membranes and report strong phonon cavity effects at room temperature, despite the modest Q ($\sim$ 100) of this system. We observe both amplification into parametric instability ("mechanical lasing") and cooling of Brownian motion in the fundamental mode through excitation of cavity sidebands. Furthermore, we characterize quenching of these parametric effects at large vibrational amplitudes, offering a window on the all-mechanical analogue of cavity optomechanics, where observation of such effects has proven elusive.

This chapter is published in Ref. 44.

3.2 Experimental results

Mechanical resonators composed of atomically thin membranes have been widely studied in recent years [3, 9, 10, 12, 34, 71, 72, 83–85]. In the case of graphene, its low mass, $\rho_g \approx 0.75\,\mathrm{mg/m^2}$, electrical integrability, and strong optical interaction [12, 86] make it a rich and versatile system studied largely for force and mass sensing. At room temperature the moderate Q's, extreme frequency tunability, and low in-line resistance of graphene resonators make them promising as intermediate-frequency ($1 - 50\,\mathrm{MHz}$) electromechanical elements, including passive filters and oscillators. At cryogenic temperatures ($T < 4\,\mathrm{K}$) graphene is becoming an attractive system for the study quantum motion, as it exhibits both large zero point motion and drastically enhanced Q's; progress towards this end has already been made [13, 14, 87], with coupling to on-chip microwave cavities and significant optomechanical cooling recently demonstrated. The mechanical nonlinearity studied here represents a complementary method for parametric control of these membranes based on intrinsic interactions of their vibrational modes. This effect can be utilized to enhance the Q (and hence sensitivity) of graphene-based sensors, provide multi-mode readout through detection of a single mode [88], and ultimately enable information exchange between optically cooled quantum modes. Moreover, this coupling makes graphene viable as low-power, tunable, electromechanical frequency mixers.

The primary source of nonlinearity in graphene membranes is motion-induced tension modulation. Similar to mode coupling in other mechanical systems [80, 89, 90], one vibrational mode (here assumed to be the fundamental mode at frequency ω_1) can be parametrically manipulated through its interac-

tion with a second mode, which is deemed the phonon cavity (at ω_c). Exciting the coupled system at the cavity's red sideband ($\omega_c - \omega_1$) results in energy flow from the fundamental to the cavity, whereas pumping the blue sideband ($\omega_c + \omega_1$) generates amplification of both the fundamental and cavity modes; these processes are depicted in Figure 3.1. The efficiency of this inter-modal energy exchange is dictated by the coupling rate, $G = d\omega_c/dx_1$, where x_1 is the amplitude of motion at ω_1. This coupling rate is reminiscent of cavity optomechanics, and an identical formalism can be used to derive the resulting equations of motion (see Section 3.3).

The advantages of graphene over other membrane materials (*e.g.* SiN or MoS_2) in generating this effect are two-fold: 1) As will be shown below, G increases linearly with the static membrane deflection x_0. In typical graphene devices this value can be tuned electrostatically via a dc gate voltage. Moreover, graphene can withstand exceptionally large out-of-plane stretching as a result of its atomic thinness ($h \sim 0.3\,\text{nm}$) and low in-plane stiffness $C = Eh/(1-\nu^2)$, where E, ν are the elastic modulus (160 GPa [91] - 1.0 TPa [27]) and Poisson ratio respectively. Previous studies of suspended graphene have shown that x_0 can exceed 3% of the membrane width without rupturing [92]. 2) Because the tension in graphene is highly tunable, the frequency spectrum can be adjusted to obtain 3-mode alignment, $\omega_c \pm \omega_1 \approx \omega_{sb}$. Here ω_{sb} signifies the resonance of a third mode, which overlaps the cavity sideband and enhances pumping by a factor of Q_{sb}; this arrangement is also depicted in Fig. 3.1 (c). Under these conditions, it is thus possible to generate large phonon cavity effects in the room temperature graphene system.

There exist alternative inter-modal coupling mechanisms for tensioned

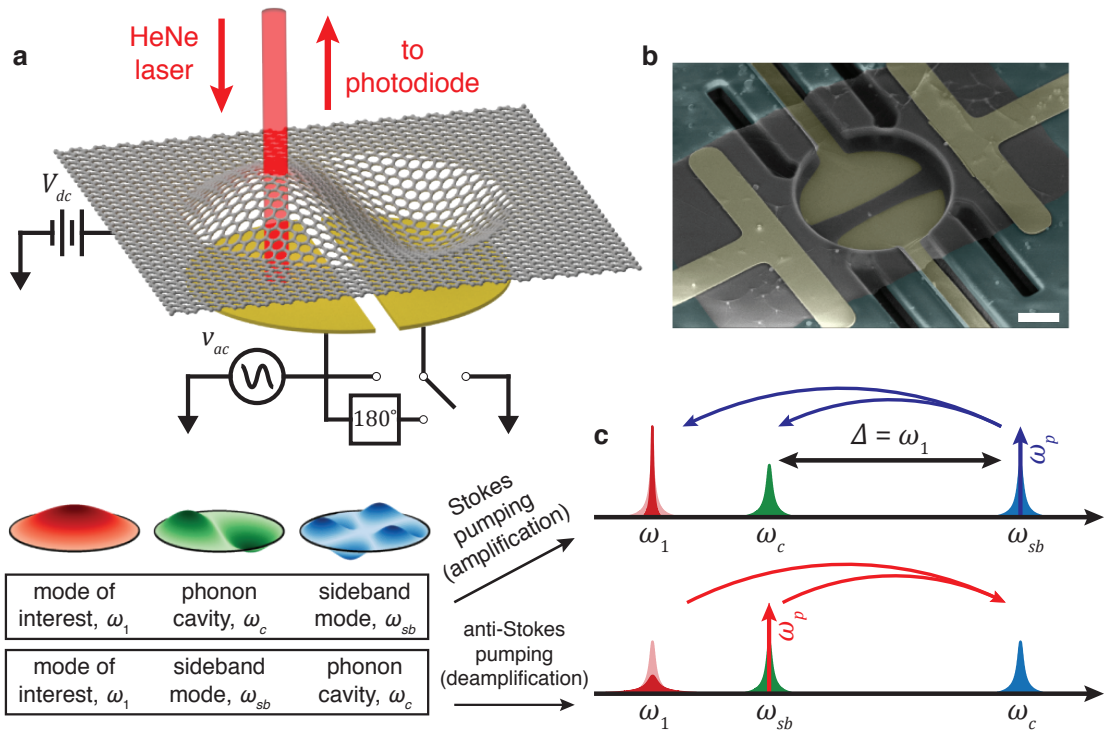

Figure 3.1: **The nonlinear graphene system.** (a) A schematic of the experimental set-up. Graphene motion is driven electrostatically by two metallic back-gates and detected through optical interferometry. The gates can be driven in various configurations to favor excitation of the fundamental mode, higher-frequency modes or both. (b) False-color electron micrograph of Device 1. Scale bar, 2 μm. (c) Schematic of the three modes necessary for efficient sideband pumping and their relative positions in frequency space. The curved arrows indicate the direction of energy flow when the system is pumped at ω_p.

membranes – most notably, mutual coupling to a resonance of the surrounding substrate [90]. Such systems enable parametric membrane control in a manner qualitatively similar to the coupling studied here, but also necessitate the 3-mode alignment described above, which can be a challenge if the spectrum is not experimentally tunable. Moreover, a unique feature of the graphene system is the tunability of the coupling rate itself, $G \propto x_0$, which is present neither in

the substrate-coupled case nor in standard optomechanical systems.

We have fabricated circular graphene drums with diameter d ranging from 5 to 20 μm; we report measurements of two such drums – "Device 1" ($d = 8\,\mu$m) and "Device 2" ($d = 20\,\mu$m) – although the effects reported have been observed across a wide number of samples. A diagram of the experimental setup and micrograph of Device 1 are shown in Fig. 3.1 (a,b). Motion is driven electrostatically via an applied gate voltage $V_{dc} + v_{ac} \sin \omega t$ and detected optically through laser interferometry [12]. Unlike previous generations of graphene resonators, our structures feature two independent back-gates, which enable efficient actuation of several modes. The gate-graphene separation is 1.7 μm. Most measurements were performed with one gate grounded and a drive voltage applied to the other, although other configurations (shown in Fig. 3.1 (a)) can be used to favor either the fundamental or higher modes.

Device 1 has 6 modes that can be readily excited (Fig. 3.2 (a,b)). The frequency dispersion of this spectrum with V_{dc} is shown in Fig. 3.2 (a). Between $V_{dc} = 0 - 7.5\,\mathrm{V}$, there is significant overlap of modes 1, 2, 6 and their respective sidebands (Fig. 3.2 (d)); therefore this is where we expect the strongest phonon cavity effect. At $V_{dc} = 5V$, the graphene has natural frequencies and Q's of: $\omega_1/2\pi = 8.6\,\mathrm{MHz}, \omega_2/2\pi = 12.4\,\mathrm{MHz}, \omega_6/2\pi = 21.0\,\mathrm{MHz}, Q_1 = \omega_1/\gamma_1 = 57, Q_2 = 48$, and $Q_6 = 37$.

The general Hamiltonian for two coupled modes in a uniformly tensioned membrane is

$$\begin{aligned} H = \sum_{n=i,j} \Big(\frac{p_n^2}{2m} + \frac{1}{2} m\omega_n^2 x_n^2 + L_n x_n + S_n x_n^2 + T_n x_n^3 + F_n x_n^4 \Big) \\ + T_{ij} x_i x_j^2 + T_{ji} x_j x_i^2 + F_{ij} x_i^2 x_j^2 \end{aligned} \tag{3.1}$$

where m, p_n are the membrane mass and momentum of mode n; a derivation

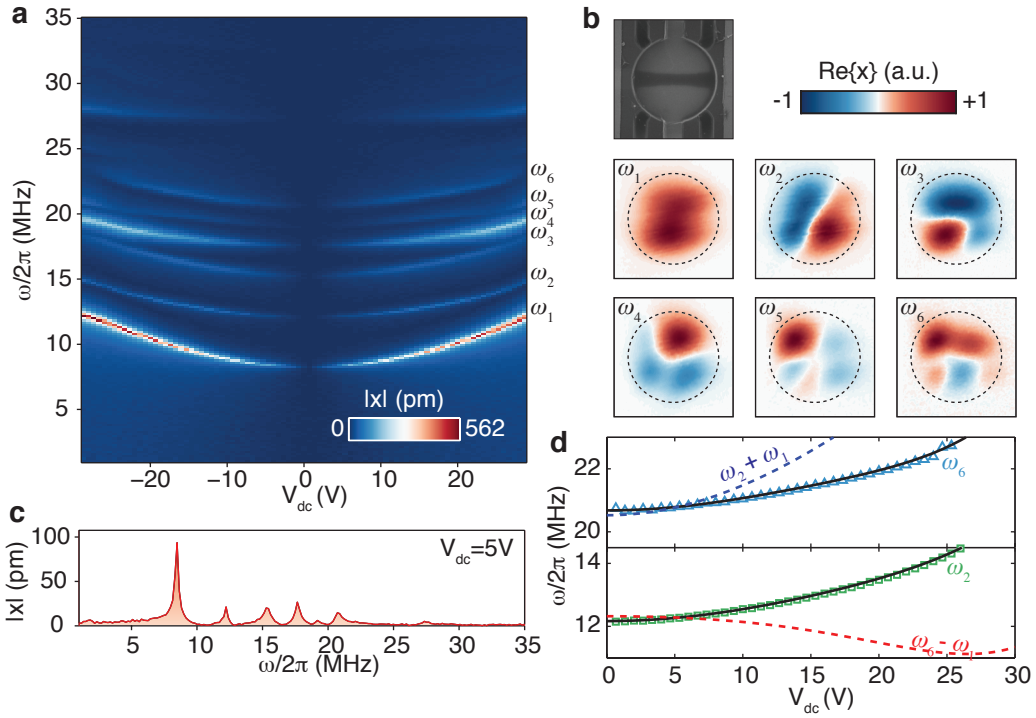

Figure 3.2: **Multimode membrane characterization.** (a) Frequency dispersion with V_{dc} for the lowest six modes in Device 1. (b) Mechanical mode shapes at $V_{dc} = 5\,\mathrm{V}$ measured by scanning the detection laser across the membrane surface while driving on resonance; color denotes the real part of the complex amplitude x, that is, the quadrature of x that is 90°out of phase with the applied a.c. voltage. The electron micrograph is given as a reference for orientation. (c) Frequency spectrum at $V_{dc} = 5\,\mathrm{V}$. (d) Resonant frequencies of mode 2 and mode 6 extracted from (a) in comparison with their sidebands with mode 1. Appreciable overlap between these frequencies occurs for $V_{dc} = 0{-}7.5\,\mathrm{V}$ and strong phonon-cavity effects are thus expected in this range.

of Equation 3.1 can be found in Section 3.3. The fourth-order nonlinearity F_i is the stretching-induced Duffing term, and is proportional to the membrane stiffness C. The remaining terms L_i, S_i, and T_i originate from the same geometric nonlinearity as F_i, combined with a static displacement x_0. Although the exact derivation requires the full solution of the elastic problem for the membrane, L_i, S_i, T_i can be viewed roughly as resulting from a binomial expansion of $F_i(x_0 +$

$x_i \cos \omega_i t)^4$. The coupling terms F_{ij} and T_{ij} have similar origins, resulting in $T_{ij} \propto x_0$. In Section 3.3 we present a calculation of these nonlinear coefficients for circular membranes and for a general membrane geometry.

In order to understand how each term in Equation 3.1 influences membrane mechanics, it is useful to consider the forces acting on mode i ($-\partial H/\partial x_i$) and examine each term in isolation. Using this approach, we see that L_i has no effect other than to exert a constant force on mode i, while S_i modifies the linear spring constant $m\omega_i^2$, and T_i, F_i contribute to a nonlinear spring constant. The coupling term F_{ij} alters the mode i spring constant by an amount proportional to $|x_j|^2$. Only the third-order term T_{ij} generates a phonon cavity effect on mode i. This is a result of its combined influence on i and j: if mode i is driven at ω_i while mode j is driven at $\omega_j \pm \omega_i$, mode j experiences a force $T_{ij} x_i x_j \propto \cos \omega_j t$ which produces motion at the cavity resonance ω_j. The two frequency components of j then mix to exert a back-action force $T_{ij} x_j^2 \propto \cos \omega_i t$ on mode i, which will amplify or dampen its motion depending on the phase of this force (*i.e.* whether the + or − sideband was driven). The remaining term T_{ji} has no appreciable impact on mode i, but enables cavity effects on mode j.

Referring again to i, j as modes $1, \mathrm{c}$, the cavity coupling rate (in a linearized approximation) is $G = d\omega_\mathrm{c}/dx_1 \approx T_{1\mathrm{c}}/m\omega_\mathrm{c}$. To measure this coupling, we drive our graphene membrane with a probe signal at frequency $\omega \approx \omega_1$ and a pump signal at ω_p. In terms of the cavity detuning $\Delta = \omega_\mathrm{p} - \omega_\mathrm{c}$ and the pumped vibration amplitude x_p, the effective resonant frequency and damping of mode

1 are:

$$\omega_{1,\text{eff}} = \Omega_1 + \frac{2G^2 \left|x_\text{p}\right|^2 \Delta \left[\gamma_\text{c}^2/4 - \omega^2 + \Delta^2\right]}{\left[\gamma_\text{c}^2/4 + (\omega - \Delta)^2\right]\left[\gamma_\text{c}^2/4 + (\omega + \Delta)^2\right]} \tag{3.2}$$

$$\gamma_{1,\text{eff}} = \gamma_1 - \frac{4G^2 \left|x_\text{p}\right|^2 \gamma_\text{c} \Delta\Omega_1}{\left[\gamma_\text{c}^2/4 + (\omega - \Delta)^2\right]\left[\gamma_\text{c}^2/4 + (\omega + \Delta)^2\right]} \tag{3.3}$$

$$m\omega_1\Omega_1 = m\omega_1^2 + 2S_1 - 12\frac{T_1\left(T_{1\text{c}}\left|x_\text{p}\right|^2 + L_1/2\right)}{m\omega_1^2 + 4S_1} + 4F_{1\text{c}}\left|x_\text{p}\right|^2 \tag{3.4}$$

where Ω_1 describes the combined effects of L_1, S_1, T_1, and F_{1c} on the mode 1 spring constant. The vibration amplitude of Device 1, mode 1 is shown in Fig. 3.3 (a,b) as ω_p is swept from ω_2 to ω_6. The $\left|x_\text{p}\right|^2$ terms in Equation 3.4 generate a downward frequency shift when any mode is pumped directly on resonance; this is most visible at $\omega_\text{p}/2\pi \approx 16\,\text{MHz}$. Sideband amplification and deamplification are also seen, and occur when pumping the blue sideband of mode 2 and red sideband of mode 6, respectively (Fig. 3.3 (a)). Amplification also occurs at $\omega_\text{p} = 2\omega_1$, and is most notable at $V_{dc} = 10\,\text{V}$, where $2\omega_1 \approx \omega_4$; this effect is studied in further detail in Section 3.7.

The amplitude of mode 1 upon sideband pumping, shown in Fig. 3.3 (d), is nearly linear with pump amplitude – in contrast to the $\left|x_\text{p}\right|^2$ dependence predicted by Equation 3.3. Analyzing the effective damping $\gamma_{1,\text{eff}}$ at the cavity sidebands reveals the source of this disagreement (Fig. 3.3 (e)). Suppression of the sideband effects is observed around $\omega = \omega_1$, indicating a broadening of the sideband mode due to the probe amplitude x_1. For the case of $\omega_c = \omega_2, \omega_{sb} = \omega_6$, motion at ω_1 and a non-zero coupling T_{62} result in increased mode 6 damping $\gamma_{6,\text{eff}}$, hindering its ability to amplify mode 1. This quenching of the cavity effects can be avoided by probing mode 1 with lower amplitudes, and speaks to the dynamic range of a micromechanical filter/amplifier based on phonon cavity cou-

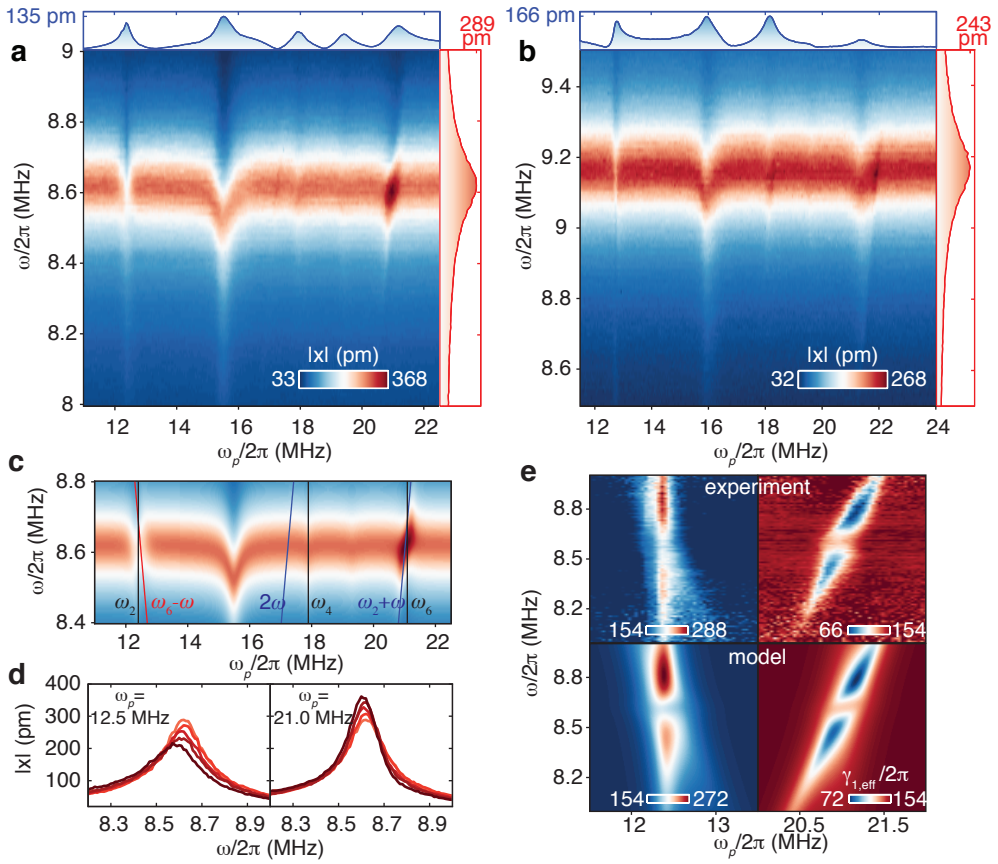

Figure 3.3: **Phonon pumping in Device 1.** (a,b) Mode 1 amplitude versus ω_p and ω at V_{dc} = 5 V (a) and 10 V (b). Right panels: Vertical slices through the data at the highest ω_p value. Upper panels: Motion in the membrane at ω_p measured simultaneously with the main panel. Measurements for both V_{dc} values were performed with equal excitation forces ($F \propto V_{dc} v_{ac}$) at the pump frequency; probe frequency forces were also equal. Cavity amplification and deamplification of mode 1 are stronger in (a), where there is better mode-sideband alignment. (c) Modeled behavior in (a) based on Equations 3.2 - 3.4. Solid lines denote the relevant frequencies for sideband effects. (d) Measured response at the cavity sidebands for V_{dc} = 5 V with linearly increasing pump strength (darkening lines). (e) Effective mode 1 damping as measured in (a) (top) and modeled by Equation 3.3 (bottom) expressed in kHz (color scales). The colors in the upper panel are truncated to the intrinsic damping $\gamma_1/2\pi$ = 154 kHz. Quenching of the cavity effect near $\omega = \omega_1$ is due to the large mode 1 amplitude and a non-zero $T_{sb,c}$ coupling. Only two free parameters (T_{1c} and $T_{sb,c}$) were used to produce each of the lower panels.

pling. Careful engineering of device modes such that $T_{sb,c} \approx 0$ would counteract this effect, and can potentially be achieved by using a more sophisticated membrane clamping scheme [72] or altering the membrane shape [93]. A detailed analysis of this quenching is presented in Section 3.8. Correcting for this effect (Figure 3.12) shows that the coupling rates in this device are $G = 6\,\mathrm{MHz/nm}$ for blue sideband pumping (amplification) and $G = 8\,\mathrm{MHz/nm}$ for red sideband pumping (deamplification). At the single quantum level, these correspond to $g_0 = G|x_{1,zpm}| = 300\,\mathrm{Hz}$ and $g_0 = 400\,\mathrm{Hz}$ respectively, where $x_{1,zpm} = \sqrt{\hbar/2m\omega_1}$.

Stronger phonon cavity effects have been measured in Device 2, where the larger device diameter permits the use of much weaker probe signals while maintaining comparable signal/noise. Measurements were performed with $V_{dc} = 4\,\mathrm{V}$, so that $\omega_1 + \omega_2 \approx \omega_5$. Fig. 3.4 shows the membrane response upon pumping at $\omega_p = \omega_1 + \omega_2 = 2\pi \times 6.76\,\mathrm{MHz}$ with a voltage v_p ramped linearly from $0 - 400\,\mathrm{mV_{pk}}$. Mode 1 is probed with $v = 0.4\,\mathrm{mV_{pk}}$, and its motion undergoes amplification by a factor of 8.5 (19 dB) before entering instability ($\gamma_{1,\mathrm{eff}} \leq 0$) at $v_p = 300\,\mathrm{mV_{pk}}$. Above this pump strength, mode 1 undergoes self-oscillation and locks onto the probe signal with a flat frequency response. The width of this flat region is 4 kHz, significantly narrower than the unpumped linewidth, $\gamma_1/2\pi = 45\,\mathrm{kHz}$. Amplification of mode 1 continues to rise for higher pump strengths, reaching a factor of 18 (25 dB) at the highest value tested.

In this configuration the graphene membrane also acts as a frequency mixer, generating motion at $\omega_\mathrm{p}+\omega$ and $\omega_\mathrm{p}-\omega$ (Fig. 3.4 (b,c)). Motion at $\omega_\mathrm{p}-\omega \approx \omega_2$ signifies occupation of the cavity mode as a result of down-scattered pump phonons, and so is significantly larger (10×) than motion at $\omega_\mathrm{p} + \omega$, where there is no mechanical resonance. Both of these mixed tones inherit the flat-top spectrum of

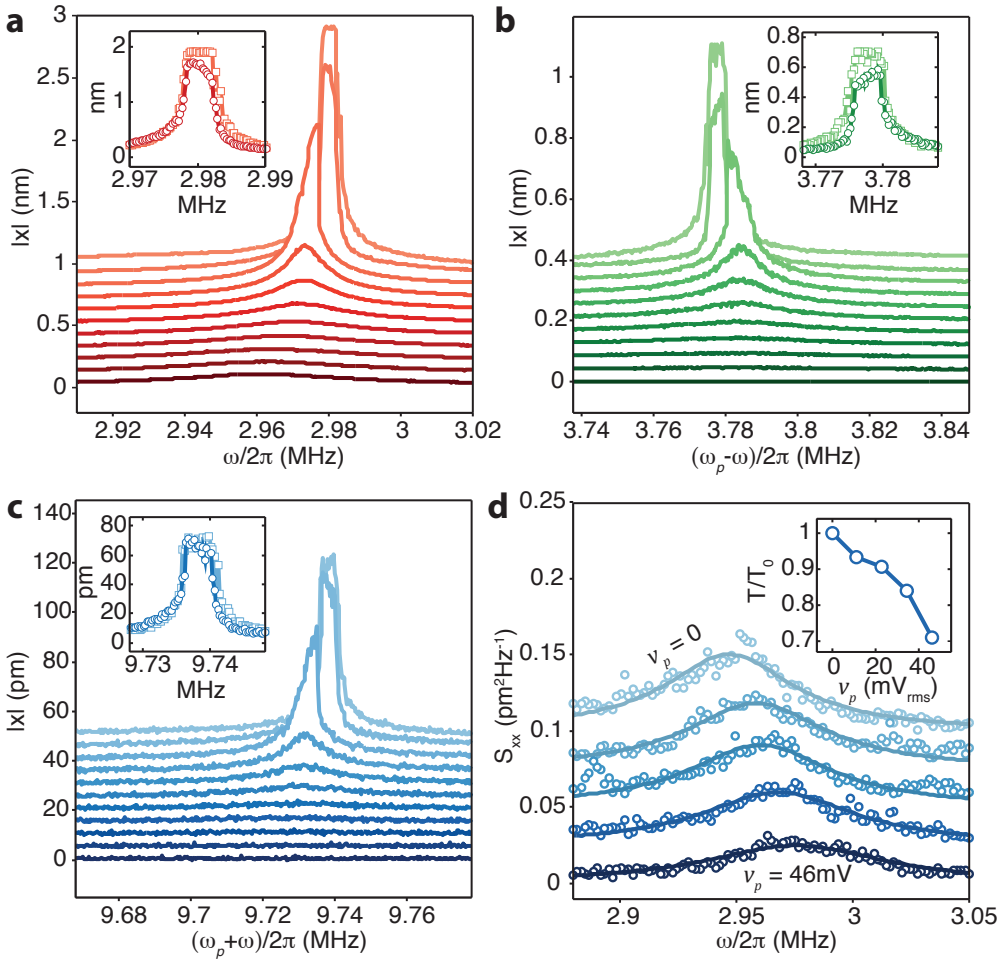

Figure 3.4: **Parametric self-oscillation and cooling in Device 2.** (a) Amplification of mode 1 ($\omega_1/2\pi = 3.0\,\text{MHz}, \gamma_1/2\pi = 45\,\text{kHz}$) and the transition to mechanical lasing ($\gamma_{1,\text{eff}} \leq 0$) via mode coupling. Mode 1 is probed with a weak drive ($v_{ac} = 0.4\,\text{mV}$) as mode 2 is pumped at its Stokes sideband ($\omega_\text{p} = 6.8\,\text{MHz}$) with increasing pump strength ($v_{ac,\text{p}} = 0 - 400\,\text{mV}$). The curves are vertically offset for clarity. Inset: Saturation of the vibrational amplitude and the flat-top response of the self-oscillating mode; no vertical offset is applied. (b,c) Frequency mixing via mechanics. Measured membrane motion at $\omega_\text{p} - \omega$ (b) and $\omega_\text{p} + \omega$ (c) recorded simultaneously with (a). (d) Measured spectral noise density near ω_1 on pumping the anti-Stokes sideband of mode 5 ($\omega_\text{p}/2\pi = 3.8\,\text{MHz}$). The curves are vertically offset for clarity. Inset: the effective temperature of mode 1 (normalized by $T_0 = 293\,\text{K}$), corresponding to the area under the S_{xx} fits. The frequency spectrum of Device 2 is given in Section 3.4.

mode 1 once it is in the self-oscillating regime.

Similar to deamplification in Device 1, red sideband pumping in Device 2 has been used to cool thermal motion of mode 1 to 200 K (Fig. 3.4 (d)). As in previous phonon cavity studies [80], the low cavity frequency $\omega_c - \omega_1$ (and high thermal phonon occupation) limits cooling in the all-mechanical system. Cooling motion towards the quantum ground state thus remains a task best suited for optical/microwave cavities, where $\omega_c \gg \omega_1$. However, interesting prospects arise if optical cavities and phonon cavities are utilized simultaneously to control graphene motion. For instance, optically cooling the phonon cavity enhances its capacity to mechanically cool the fundamental mode – in such a case cooling is limited only by the cooperativities $G^2|x_p|^2/\gamma_1\gamma_c$ of the two cavities. Moreover, the mechanical pump grants experimental control over the interaction strength of the two modes. Microwave-cavity-coupled graphene systems [13, 14, 87] are therefore ideal testbeds for quantum entanglement, squeezing, thermalization, and information exchange between modes near their ground state. The greatly enhanced Q factors of graphene at dilution refrigerator temperatures [10, 30] will only serve to strengthen these effects.

We have demonstrated tension-mediated coupling between mechanical modes in suspended graphene, and its potential for parametric control of this system. Sideband cooling and amplification of membrane motion, up to self-oscillation, have been observed within a single device. The potential for graphene membranes as frequency mixers with intrinsically flat pass-bands has also been shown. As graphene, transition metal dichalcogenides, and related two-dimensional materials continue to be developed and exploited for their unique mechanical properties, these inherent membrane nonlinearities can ulti-

mately be utilized to artificially enhance the Q's of future sensors and electronics, facilitate bitwise logic operations between coupled membrane modes [4], and open new possibilities in the study of coupled quantum systems.

3.3 Mode coupling in a 2D circular membrane with electrostatic drive – Theory

The static deformation and the dynamics of the circular membrane are described in terms of the following Lagrangian, for which we have assumed that the induced tension can be averaged over the membrane geometry, effectively leading to a description in terms of a mean-field model:

$$\begin{aligned} L = \frac{\rho}{2}\int dA\,\dot{x}^2 - \frac{D}{2}\int dA(\Delta x)^2 - \frac{C}{16}\left[\frac{1}{A}\int dA(\nabla x)^2\right]\cdot\int dA(\nabla x)^2 \\ - \frac{T_0}{2}\int dA(\nabla x)^2 + \frac{\epsilon_0 V_g^2}{2}\int \frac{dA}{d-x} \end{aligned} \tag{3.5}$$

where ρ is the surface density, D is the flexural rigidity, C the in-plane stiffness, T_0 the built-in tension, V_g the gate voltage, d the gate-sheet separation, x the deformation. If the description of the system can be performed in terms of a continuum model, we have

$$C = \frac{Eh}{1-\nu^2} \tag{3.6}$$

$$D = \frac{Eh^3}{12(1-\nu^2)}. \tag{3.7}$$

where h is the membrane thickness and E, ν are the Young's modulus and Poisson ratio, respectively. The first term in Equation 3.5 represents the kinetic energy associated with the dynamics of the membrane, the second its flexural elastic energy, the third the energy associated with the deformation-induced tension (treated on a mean-field level), the fourth the energy due to built-in tension and last term corresponds to the capacitive coupling with the back gate.

By expanding x into static and resonant components $x(\vec{r},t) = x_0(\vec{r}) + \sum_i x_i(t)\xi_i(\vec{r})$ – where $\xi_i(\vec{r})$ is the dimensionless profile of mode i, normalized such

that $\frac{1}{A}\int dA|\xi_i(\vec{r})|^2 = 1$ – it is straightforward to show that Equation 3.5 leads to the Hamiltonian given by Equation 3.1 in Section 3.2, with nonlinear coefficients

$$L_i = \left[T_0 + \frac{C}{4A}\int dA(\nabla x_0)^2\right]\cdot\int dA(\nabla x_0\nabla\xi_i) \tag{3.8}$$

$$S_i = \frac{C}{4A}\left[\int dA(\nabla x_0\nabla\xi_i)\right]^2 \tag{3.9}$$

$$T_i = \frac{C}{4A}\left[\int dA(\nabla x_0\nabla\xi_i)\right]\cdot\int dA(\nabla\xi_i)^2 \tag{3.10}$$

$$F_i = \frac{C}{16A}\left[\int dA(\nabla\xi_i)^2\right]^2 \tag{3.11}$$

$$S_{ij} = \frac{C}{2A}\left[\int dA(\nabla x_0\nabla\xi_i)\right]\cdot\int dA(\nabla x_0\nabla\xi_j) \tag{3.12}$$

$$T_{ij} = \frac{C}{4A}\left[\int dA(\nabla x_0\nabla\xi_i)\right]\cdot\int dA(\nabla\xi_j)^2 \tag{3.13}$$

$$F_{ij} = \frac{C}{8A}\left[\int dA(\nabla\xi_i)^2\right]\cdot\int dA(\nabla\xi_j)^2 \tag{3.14}$$

Above we have assumed displacements are large such that the flexural rigidity is negligible: $x \gg h$.

It is important to note that the terms listed in Equations 3.8 - 3.14 (and included terms in Equation 3.1 of Section 3.2) are the only nonlinear terms expected from the Lagrangian 3.5. Terms of the type $F_{ij}x_i x_j^3$, $T_{ijk}x_i x_j x_k$, and $F_{ijk}x_i x_j x_k^2$ do not appear in this calculation due to mode orthogonality and are therefore excluded from Equation 3.1. From this perspective, our analysis differs from that performed in Reference [66], where the full Föppl-von Kármán equations are solved in the limit of vanishing flexural rigidity. In our case, while taking into account the effect of finite flexural rigidity, owing to the smallness of the membrane displacement, we neglect spatial inhomogeneities of the tension.

We now proceed to calculate the nonlinear coefficients L, S, T, F explicitly for a circular membrane geometry. From Equation 3.5 it is possible to derive an

equation for the static displacement of the membrane

$$\Delta^2\zeta_0 - \tau\Delta\zeta_0 = \kappa_0 V_g^2 \tag{3.15}$$

where ζ_0 represents the static displacement (expressed in units of r_0) of the membrane in presence of a time-independent external voltage V_g, $\kappa_0 = \epsilon_0 r_0^3/\left[2(d-x)^2 D\right]$ and $\tau(= Tr_0^2/D)$ is the (dimensionless) membrane tension, whose value has to be determined from the solution of the following equation

$$\tau = \tau_0 + \frac{2\epsilon}{\pi}\int d\Omega(\nabla\zeta_0)^2. \tag{3.16}$$

The solution of Equation 3.15 is given by

$$\zeta_0 = \frac{\kappa_0 V_g^2}{4\tau}\left[1 - r^2 + 2\frac{I_0(\sqrt{\tau}r) - I_0(\sqrt{\tau})}{\tau I_1(\sqrt{\tau})}\right]. \tag{3.17}$$

In order to determine τ, the result given in Equation 3.17 is substituted into Equation 3.16, yielding the following self-consistent equation for τ

$$\tau = \tau_0 + \frac{\epsilon\kappa_0^2 V_g^4}{4\tau^2}\left(\frac{16}{\tau} - \frac{2R_0(\tau)}{\sqrt{\tau}} - R_0^2(\tau) + 3\right) \tag{3.18}$$

with $R_0(\tau) = I_0(\sqrt{\tau})/I_1(\sqrt{\tau})$ ($I_n(x)$ is the modified Bessel function of the first kind of order n). From the non-dimensionalized version of the Lagrangian given in Equation 3.5, it is possible to obtain the Hamiltonian $\mathcal{H}$ describing the dynamics of small oscillations around ζ_0 in terms of the operators a_i, $a_\mathrm{i}^\dagger$, $X \doteq a_\mathrm{i} + a_\mathrm{i}^\dagger$

$$\begin{aligned}\mathcal{H} = {} & \widetilde{\omega}_\mathrm{a}\hat{a}_\mathrm{a}^\dagger\hat{a}_\mathrm{a} + \widetilde{\omega}_b\hat{a}_\mathrm{b}^\dagger\hat{a}_\mathrm{b} \\ & + \mathcal{L}_\mathrm{a}\hat{X}_\mathrm{a} + \mathcal{S}_\mathrm{a}\hat{X}_\mathrm{a}^2 + \mathcal{T}_\mathrm{a}\hat{X}_\mathrm{a}^3 + \mathcal{F}_\mathrm{a}\hat{X}_\mathrm{a}^4 \\ & + \mathcal{L}_\mathrm{b}\hat{X}_\mathrm{b} + \mathcal{S}_\mathrm{b}\hat{X}_\mathrm{b}^2 + \mathcal{T}_\mathrm{b}\hat{X}_\mathrm{b}^3 + \mathcal{F}_\mathrm{b}\hat{X}_\mathrm{b}^4 \\ & + \mathcal{T}_\mathrm{ab}\hat{X}_\mathrm{b}^2\hat{X}_\mathrm{a} + \mathcal{T}_\mathrm{ba}\hat{X}_\mathrm{a}^2\hat{X}_\mathrm{b} + \mathcal{F}_\mathrm{ab}\hat{X}_\mathrm{a}^2\hat{X}_\mathrm{b}^2\end{aligned} \tag{3.19}$$

where

$$\mathcal{L}_{\mathrm{i}} = \frac{r_0^2 T}{D}\bar{B}_{\mathrm{i}}(T)\tilde{x}_{\mathrm{i}} \tag{3.20}$$

$$\mathcal{S}_{\mathrm{i}} = \frac{2\epsilon}{\pi}\bar{B}_{\mathrm{i}}^2(T)\tilde{x}_{\mathrm{i}}^2 \tag{3.21}$$

$$\mathcal{T}_{\mathrm{i}} = \frac{2\epsilon}{\pi}\alpha_{\mathrm{i}}^2\bar{B}_{\mathrm{i}}(T)\tilde{x}_{\mathrm{i}}^3 \tag{3.22}$$

$$\mathcal{F}_{\mathrm{i}} = \frac{\epsilon}{2\pi}\alpha_{\mathrm{i}}^4\tilde{x}_{\mathrm{i}}^4 \tag{3.23}$$

$$\mathcal{T}_{\mathrm{ij}} = \frac{2\epsilon}{\pi}\alpha_{\mathrm{j}}^2\bar{B}_{\mathrm{i}}(T)\tilde{x}_{\mathrm{j}}^2\tilde{x}_{\mathrm{i}} \tag{3.24}$$

$$\mathcal{F}_{\mathrm{ij}} = \frac{\epsilon}{\pi}\alpha_{\mathrm{i}}^2\alpha_{\mathrm{j}}^2\tilde{x}_{\mathrm{i}}^2\tilde{x}_{\mathrm{j}}^2, \tag{3.25}$$

with $\mathrm{i},\mathrm{j} \in \{a, b\}$, $\tilde{x}_{\mathrm{i}} = \sqrt{\frac{1}{2\mu\widetilde{\omega}_{\mathrm{i}}}}$, and α_i being the Bessel function zero associated with the i^{th} circular membrane mode (≈ 2.4048 for the fundamental). Moreover we have

$$\bar{B}_{\mathrm{i}}(T) = B_{\mathrm{i}}(\tau) = \frac{\sqrt{\pi}\kappa_0 V_g^2}{\tau}\alpha_{\mathrm{i}}\left[\frac{2}{\alpha_{\mathrm{i}}^2} - \frac{\sqrt{\tau}}{\tau + \alpha_{\mathrm{i}}^2}R_0(\tau)\right] \tag{3.26}$$

and

$$\epsilon = \frac{3r_0^2}{2h^2} \tag{3.27}$$

$$\widetilde{\omega}_{\mathrm{i}} = \frac{\alpha_{\mathrm{i}}\hbar}{r_0 D}\sqrt{\frac{T}{\rho}} = \omega_i\frac{\hbar}{D} \tag{3.28}$$

$$\mu = \frac{\rho r_0^4 D}{\hbar^2}. \tag{3.29}$$

The dimensionless coefficients $\mathcal{L}$,$\mathcal{S}$,$\mathcal{T}$,$\mathcal{F}$ can be re-dimensionalized according to: $L_{\mathrm{i}} = \mathcal{L}_{\mathrm{i}}D/(r_0\tilde{x}_{\mathrm{i}})$, $S_{\mathrm{i}} = \mathcal{S}_{\mathrm{i}}D/(r_0\tilde{x}_{\mathrm{i}})^2$, $T_{\mathrm{ij}} = \mathcal{T}_{\mathrm{ij}}D/(r_0^3\tilde{x}_{\mathrm{i}}\tilde{x}_{\mathrm{j}}^2)$, $F_{\mathrm{ij}} = \mathcal{F}_{\mathrm{ij}}D/(r_0^4\tilde{x}_{\mathrm{i}}^2\tilde{x}_{\mathrm{j}}^2)$. Moreover, in Equation 3.19 and the discussion that follows, the second order coupling $\mathcal{S}_{\mathrm{ij}}$ has been excluded as only the fundamental mode has appreciable overlap with the static deformation x_0.

For large values of the induced tension the values of T and $\bar{B}_{\mathrm{i}}(T)$ are given

by

$$T = \frac{1}{4}\left[\frac{r_0^2\epsilon_0^2 C}{(d-x)^4}\right]^{1/3} V_g^{4/3} \tag{3.30}$$

$$\bar{B}_{\mathrm{i}}(T) = \frac{4\sqrt{\pi}}{\alpha_{\mathrm{i}}}\left[\frac{\epsilon_0 r_0}{(d-x)^2 C}\right]^{1/3} V_g^{2/3}. \tag{3.31}$$

In Equation 3.19 $\mathcal{L}_{\mathrm{i}}$ is a term that can be trivially "displaced" away, $\mathcal{T}_{\mathrm{ij}}$, $\mathcal{T}_{\mathrm{i}}$ and $\mathcal{F}_{\mathrm{i}}$, $\mathcal{F}_{\mathrm{ij}}$ are the terms relevant for the radiation-pressure and Duffing physics, while $\mathcal{S}_{\mathrm{i}}$ represents a shift in frequency of the mode considered.

As an example, we focus our attention on 3 different modes of a circular membrane: $(0,1)$ (hereafter mode a) , $(1,1)$ (mode b for the red-detuned case), $(3,1)$ (mode b for the blue-detuned case). This choice is related to the necessity of having three modes for which $\omega_1 \simeq \omega_2 + \omega_3$. This condition is optimal in terms of radiation pressure-like coupling between modes. The $(0,1)$ mode plays the role of the mechanical mode, while modes $(1,1)$, $(3,1)$ play the role of the driving tone (cavity) and cavity (driving tone) for red- (blue-) sideband detuning respectively. Due to the large density of states at the cavity resonance, driving the system close to one of its resonances (which has non-negligible overlap with the cavity resonance) allows for an efficient excitation of the sideband, leading to a stronger optomechanical coupling, for a given input drive, as compared to the case for which the resonance close to the pump frequency is absent.

The physics leading to the frequency and damping shift of the fundamental mode can be essentially explained with the same analysis performed for optomechanical systems. The driving around ω_{p} can be interpreted as the "optical pump", detuned away from a "cavity" by the mechanical resonant frequency.

The calculation goes as follows: the strong drive field β_{in} around ω_{p} is determined by the solution of the I/O equations for a free (*i.e.* uncoupled to other

modes) mode, this mode will then be considered as the sideband (with respect to ω_c) drive in the I/O equations for the coupled system whose unitary dynamics are described by the Hamiltonian 3.19. The analysis of these quantum Langevin equations (QLEs) will be performed in terms of a standard linearisation procedure, in complete analogy to what is done in the context of optomechanical systems.

With the approximations mentioned above, the cavity field around ω_p can be written as

$$\beta = \frac{\sqrt{\gamma_p}\beta_{in}}{\frac{\gamma_p}{2} - i(\omega - \omega_p)} \tag{3.32}$$

The value of β represents thus, on one hand, the oscillation amplitude when the resonator is driven close to the resonance ω_p, and, on the other the amplitude of oscillations at a frequency which is detuned by $\omega_p - \omega_c \simeq \omega_f$ ($\omega_f = \omega_a$). The relative values of ω_a, ω_{b1} and ω_{b2} allow us therefore to have a strong field β, since we are driving the system on resonance, and at the same time, exploit the optomechanical-like sideband physics.

In order to describe the nonlinear sideband physics, we write the QLEs associated with the Hamiltonian 3.19

$$\begin{aligned}\dot{a} =& -i\omega_a a - i\mathcal{L}_a - i2\mathcal{S}_a(a^\dagger + a) - i3\mathcal{T}_a(a^\dagger + a)^2 - i4\mathcal{F}_a(a^\dagger + a)^3 \\ & - i\mathcal{T}_{ab}(b^\dagger + b)^2 - i2\mathcal{F}_{ab}(a^\dagger + a)(b^\dagger + b)^2 \\ & - \frac{\gamma_a}{2}a + \sqrt{\gamma_a}a_{in}\end{aligned} \tag{3.33}$$

$$\begin{aligned}\dot{b} =& -i\omega_b b - i4\mathcal{F}_b(b^\dagger + b)^3 \\ & - i\mathcal{T}_{ab}(a^\dagger + a)(b^\dagger + b) - i2\mathcal{F}_{ab}(a^\dagger + a)^2(b^\dagger + b) - \frac{\gamma_b}{2}b + \sqrt{\gamma_b}b_{in}.\end{aligned} \tag{3.34}$$

We can solve Equations 3.33, 3.34 perturbatively, assuming that we can expand a and b as $a \to \alpha + a$ and $b \to \beta + b$, where α represents the coherent oscilla-

tion amplitude of the fundamental mode induced by β whose value is given by Equation 3.32. The value of α can be obtained as the solution of the zeroth-order term in the expansion of Equation 3.33, which can be written as

$$\begin{aligned}\dot{\alpha} =& -i\omega_a\alpha - i\mathcal{L}_a - i2\mathcal{S}_a(\alpha^* + \alpha) - i3\mathcal{T}_a(\alpha^* + \alpha)^2 - i4\mathcal{F}_a(\alpha^* + \alpha)^3 \\ & - i\mathcal{T}_{ab}(\beta^* + \beta)^2 - i2\mathcal{F}_{ab}(\alpha^* + \alpha)(\beta^* + \beta)^2 - \frac{\gamma_a}{2}\alpha + \sqrt{\gamma_a}\alpha_{in}.\end{aligned} \tag{3.35}$$

In the substitution $a \rightarrow \alpha + a$ we have assumed that $\dot{\alpha} = 0$. This assumption is justified when the conditions $\omega_a < 2\omega_b$, and $\gamma_a < (\omega_a - \omega_b)$ are fulfilled, (rotating wave approximation), leading to

$$\alpha = -2\frac{\mathcal{T}_{ab}|\beta|^2 + \mathcal{L}_a/2}{(\omega_a + 4\mathcal{S}_a)} \tag{3.36}$$

where higher-order terms have been neglected, and we have assumed, without loss of generality $\alpha^* = \alpha$.

The first-order term in the expansion of Equations 3.33, 3.34 can be written as

$$\begin{aligned}\dot{a} =& -i\omega_a a - i2\mathcal{S}_a(a^\dagger + a) - i6\mathcal{T}_a(\alpha^* + \alpha)(a^\dagger + a) - i12\mathcal{F}_a(\alpha^* + \alpha)^2(a^\dagger + a) \\ & - i2\mathcal{T}_{ab}(\beta^* b + \beta b^\dagger) - i2\mathcal{F}_{ab}\left[(\beta^* + \beta)^2(a^\dagger + a) + (\alpha^* + \alpha)(\beta^* + \beta)(b^\dagger + b)\right] \\ & - \frac{\gamma_a}{2}a + \sqrt{\gamma_a}a_{in}\end{aligned} \tag{3.37}$$

$$\begin{aligned}\dot{b} =& -i\omega_b b - i3\mathcal{F}_b(\beta^* + \beta)^2(b^\dagger + b) - i\mathcal{T}_{ab}\left[(\beta^* + \beta)^2(a^\dagger + a) + (\alpha^* + \alpha)(\beta^* + \beta)(a^\dagger + a)\right] \\ & - i\mathcal{F}_{ab}\left[2(\alpha^* + \alpha)^2(b^\dagger + b) + (\alpha^* + \alpha)(\beta^* + \beta)(a^\dagger + a)\right] - \frac{\gamma_b}{2}b + \sqrt{\gamma_b}b_{in}.\end{aligned} \tag{3.38}$$

Neglecting again higher-order terms, Equations 3.37, 3.38 can be written as

$$\begin{aligned}\dot{a} =& -i\omega_a a - i\left[2\mathcal{S}_a - 12\frac{\mathcal{T}_a(\mathcal{T}_{ab}|\beta|^2 + \mathcal{L}_a/2)}{\omega_a + 4\mathcal{S}_a} + 4\mathcal{F}_{ab}|\beta|^2\right]a \\ & - i2\mathcal{T}_{ab}(\beta^* b + \beta b^\dagger) - \frac{\gamma_a}{2}a + \sqrt{\gamma_a}a_{in}\end{aligned} \tag{3.39}$$

$$\dot{b} = -i\omega_b b - i2\mathcal{T}_{ab}\beta(a^\dagger + a) - \frac{\gamma_b}{2}b + \sqrt{\gamma_b}b_{in} \tag{3.40}$$

where RWA has been used for a, b, and β. Equations 3.39, 3.40 can be written more compactly as

$$\dot{a} = -i\Omega_a a - i(G^* b + G b^\dagger) - \frac{\gamma_a}{2} a + \sqrt{\gamma_a} a_{in} \tag{3.41}$$

$$\dot{b} = -i\omega_b b - iG(a^\dagger + a) - \frac{\gamma_b}{2} b + \sqrt{\gamma_b} b_{in} \tag{3.42}$$

where

$$\Omega_a = \omega_a + 2\mathcal{S}_a - 12\frac{\mathcal{T}_a(\mathcal{T}_{ab}|\beta|^2 + \mathcal{L}_a/2)}{\omega_a + 4\mathcal{S}_a} + 4\mathcal{F}_{ab}|\beta|^2 \tag{3.43}$$

$$G = 2\mathcal{T}_{ab}\beta. \tag{3.44}$$

Equations 3.41, 3.42 are the equation of motion of two linearly coupled harmonic oscillators, and are equivalent to the linearised equation of motion for an optomechanical system. It can be shown that in this setup the mode a undergoes a frequency shift and a damping shift given by

$$\omega_{\text{eff}} = \sqrt{\Omega_a^2 + \frac{4|G|^2\Delta\Omega_a\left[\gamma_b^2/4 - \omega^2 + \Delta^2\right]}{\left[\gamma_b^2/4 + (\omega - \Delta)^2\right]\left[\gamma_b^2/4 + (\omega + \Delta)^2\right]}} \tag{3.45}$$

$$\gamma_{\text{eff}} = \gamma_a - \frac{4\gamma_b|G|^2\Delta\Omega_a}{\left[\gamma_b^2/4 + (\omega - \Delta)^2\right]\left[\gamma_b^2/4 + (\omega + \Delta)^2\right]}. \tag{3.46}$$

From Equations 3.41 and 3.45, it is clear how the observed frequency shifts have 2 different sources. On the one hand, it is determined by "geometric" nonlinearities, *i.e.* effects which are essentially determined by the eigenmode shapes,dictating the value of Ω_a in Equation 3.43, on the other it depends on the mechanical analogue of optomechanical effects ω_{eff}.

As a final note on the nonlinear parameters $\mathcal{L}$,$\mathcal{S}$,$\mathcal{T}$,$\mathcal{F}$, we provide a numerical comparison of these quantities (based on Equations 3.20 - 3.25) for a graphene drum with dimensions equal to Device 1. The values quoted in Table 3.1 have been obtained by fitting the ω vs. V_g dependence for the funda-

mental mode, assuming the (dimensionless) built-in tension τ_0 and the surface density of the drum as free parameters. From the fit, we have obtained $\omega|_{Vg=0} = 2\pi \cdot 8.52\text{MHz}$, $T_0 = 0.051\text{N/m}$. The value of $\mathcal{L}_1$ has been expressed in nN since it represents the static forced induced by V_{dc} on the resonator. Values shown are calculated at the single phonon level. Perhaps more significantly we

Table 3.1: Size comparison of the competing nonlinear terms

$\mathcal{L}_1 \frac{D}{x_{\text{zpm}}}$	$\mathcal{S}_1 \frac{D}{\hbar}$	$\mathcal{T}_1 \frac{D}{\hbar}$	$\mathcal{F}_1 \frac{D}{\hbar}$	$\mathcal{T}_{12} \frac{D}{\hbar}$	$\mathcal{F}_{12} \frac{D}{\hbar}$
0.86nN	8.18kHz	0.3018Hz	1.441μHz	0.4814Hz	2.29μHz

can show that the effective coupling (3.44) takes the following values for different driving amplitudes:

Table 3.2: $G = 2\mathcal{T}_{\alpha\beta}\beta$, when expressed in Hz.

	$x_\beta = x_{\text{zpm}}$	$x_\beta = 0.1\text{nm}$	$x_\beta = 10\text{nm}$
$G\frac{D}{\hbar}\frac{x_\beta}{x_{\text{zpm}}}$	0.97Hz	2.15kHz	215kHz

Moreover, the correction to the frequency ω_{a} on the first line of Equation 3.39 is given by:

Table 3.3: Overall frequency shift $\delta\omega$ from other nonlinear terms.

	$x_\beta = x_{\text{zpm}}$	$x_\beta = 0.1\text{nm}$	$x_\beta = 10\text{nm}$
$\delta\omega = 2\mathcal{S}_{\text{a}} - 12...$	1.3027kHz	1.3098kHz	71.4kHz

3.4 Characterization of Devices 1 and 2

The graphene devices studied in this chapter are shown in Figure 3.5. Their physical properties are given in Table 3.4. The mass density of these membranes is $\approx 10\times$ that of bare graphene due to surface contaminants (most likely PMMA from fabrication [33]). Mass density here has been measured by fits to the AC amplitude of motion as V_{dc} is varied, described in Section 3.5 and presented in Figure 3.7. These values can also be obtained from fits to the resonant frequency dispersion $f(V_{dc})$, as has been described in numerous works previously [10, 12, 71, 72]. The intrinsic tension T_0 is calculated from $f = (\alpha/2\pi r_0)\sqrt{T/\rho}$, where $\alpha \approx 2.404$.

A spectrum for Device 2 at $V_{dc} = 4$V is given in Figure 3.6. The pumping conditions used in Figure 3.4 are also shown.

Device #	diameter (μm)	$\rho/\rho_{\text{graphene}}$	$f_1(V_{dc} = 0)$(MHz)	T_0(N/m)
1	7.8	11 ± 2	8.35	0.060
2	19.9	9.5 ± 1	2.9	0.040

Table 3.4: Graphene device properties

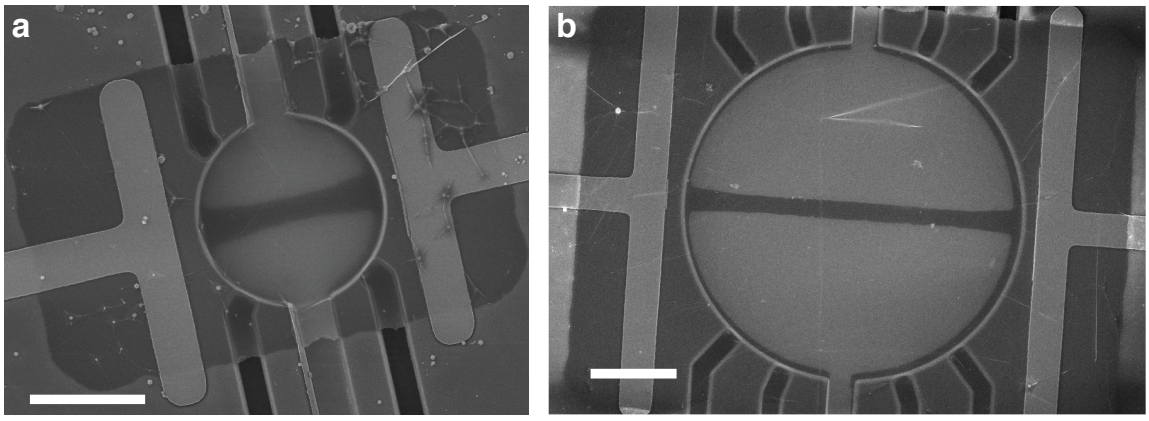

Figure 3.5: **Scanning electron micrograph of Device 1 and 2.** Scale bars are 5 μm. In both cases graphene is suspended above a 1.7 μm-deep circular trench in SiO_2. Linear trenches (6 in (a) and 10 in (b)) allow fluid to drain from under the graphene during device fabrication. All but two trenches terminate in a thin SiO_2 bridge so as not to affect the membrane boundary conditions. The remaining two trenches carry 50 nm-thick platinum leads to the split back-gates. Platinum source and drain leads contact the graphene bottom surface.

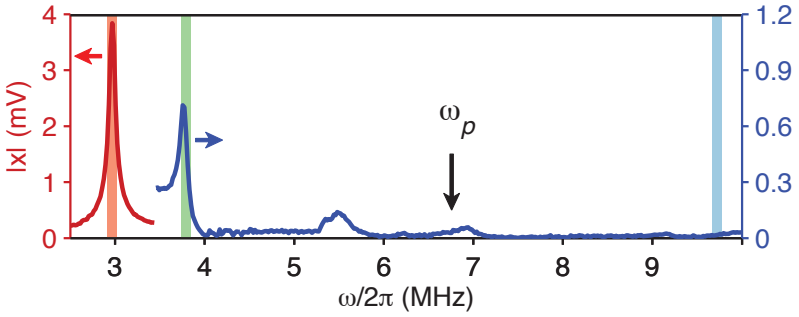

Figure 3.6: **Frequency spectrum of Device 2.** The pump configuration used to obtain Figure 3.4 (a-c) is shown. Vertical bands denote the three frequency ranges in which motion was measured while pumping ω_p.

3.5 Calibration of optical detection system

Calibration of the electrical and optical components of our setup were performed by pulling on Device 1 with a varying DC gate voltage (and fixed AC voltage) while measuring both the AC and DC components of our reflected laser power. As described below, this process allows us to determine the absolute deflection of our graphene membrane (both the static and resonant components), as well as the effective AC gate voltage that is experienced by the graphene, v_{ac}. This latter value is substantially smaller than the applied AC voltage, V_{ac}, due to parasitic losses of our cables and wire bonds, contact resistance of the graphene, and other unavoidable losses. The DC gate voltage, V_{dc}, does not suffer this effect, as the graphene-gate capacitor (C) will reach the experimentally applied voltage within a few RC time constants, where R encompasses all series resistances.

Following an approach reported previously [12], the graphene is considered to be situated in an optical standing wave generated by the incident laser light and reflection from the metallic back-gate. Because of the graphene's 2.3% optical absorption [61], the overall reflected power out of the system is sensitive to the graphene position within this standing wave; this sensitivity enables us to detect graphene motion. The DC component of our reflected laser power depends on graphene position, x, as

$$P_{dc} = P_0 + \Delta P \sin\left(\frac{4\pi}{\lambda}x + \theta\right) \tag{3.47}$$

where λ is the wavelength of light used (633nm) and P_0, ΔP, θ are the average power, modulation depth, and phase of the standing wave at the graphene, respectively. The position x can be altered by pulling the graphene towards the back-gate with a bias voltage, $V = V_{dc} + v_{ac}\sin\omega t$. If $v_{ac} \ll V_{dc}$, and ω is far below

any mechanical resonance of the graphene, the ac portion of our reflected laser power is:

$$P_{ac} = \Delta P \cos\left(\frac{4\pi}{\lambda}x + \theta\right) \cdot \frac{4\pi}{\lambda}\frac{dx}{dV_{dc}}v_{ac}. \tag{3.48}$$

In principle P_0, ΔP, and θ can be calculated from the incident power, refractive index of graphene and back-gate, and the graphene-gate separation. However, this calculation is complicated by: (1) the quality and size of our laser spot (diameter $\approx 1\mu$m), (2) the thickness, roughness, and refractive index of surface contaminants on the graphene [33], and (3) graphene adherence to the vertical walls of the trench [27], among other uncertainties. These parameters must therefore be measured experimentally – in this case by pulling the graphene a significant fraction of the distance $\lambda/4$. To simplify calculations, the membrane deflection profile is assumed to be a paraboloid $x(r) = x_0(1 - r^2/r_0^2)$, where r, r_0 are radial position and membrane radius, and x_0 is the height of the membrane center. The membrane position can then be calculated from the balance of tension and electrostatic forces:

$$4\pi T_0 x_0 + \frac{4\pi E}{r_0^2}x_0^3 = \frac{1}{2}C'V_{dc}^2. \tag{3.49}$$

Above, T_0 and E are the 2D membrane tension and 2D Young's modulus (in N/m), respectively, and $C' = dC/dx$. This is a modified version of force equations reported elsewhere[12, 27], adjusted for the paraboloid approximation. The tension T_0 can be recast as the membrane mass density ρ by knowledge of the resonant frequency: $\rho = T_0(2.404/(\omega_1 r_0))^2$.

Equations 3.47 - 3.49 thus provide a means to model our optical system as the bias voltage V_{dc} is varied. Figure 3.7 shows a representative data set from which P_0, ΔP, θ, ρ, and v_{ac}/V_{ac} are measured for Device 1. Here, V_{dc} is swept (0 – 35V) while a constant V_{ac} (200mV$_{\text{pk}}$, $\omega = 2\pi \times 100$kHz) is applied to both back-gates.

AC data is fitted first, by numerically finding the roots of Equation 3.49 and applying them to Equation 3.48; results are shown in Figure 3.7 (a). This fit provides values for ρ, $\Delta P \cdot v_{ac}$, and θ. With these parameters determined, P_{dc} is fitted to Equation 3.48 to obtain P_0 and ΔP; this is shown in Figure 3.7 (b). The excellent agreement of this second, more constrained fit verifies the validity of this model. With all the parameters of Equations 3.47 - 3.49 determined, we can plot the DC and AC membrane deflection for this data set, as shown in Figure 3.7 (c,d). Interesting features in these curves are: 1) In Figure 3.7 (d), the transition from quadratic to sub-linear DC deflection above $V_{dc} \approx 25$V caused by the E term in Equation 3.49. 2) The resulting maximum in AC deflection that this transition produces, as shown in Figure 3.7 (c).

In performing these fits, the measured modulus of similarly produced CVD graphene[91] is used, $E = 55$N/m. Moreover, for the purposes of Equations 3.47 and 3.48, it is assumed that our laser spot performs a "point-like" measurement of x at the membrane's center of mass, $r_{cm} = r_0/\sqrt{2}$. Equation 3.49 was corrected for this off-center measurement, $x(r_{cm}) = x_0/2$. The resulting mass density of Device 1 is $\rho/\rho_g = 11 \pm 2$, where $\rho_g = 0.75\text{mg/m}^2$ is the density of monolayer graphene; the extra mass is attributed to polymer contaminants from fabrication. The AC gate voltage "felt" by the graphene is $v_{ac} = 11\text{mV}_{\text{pk}}$, or $v_{ac}/V_{ac} = 5.5\%$. From similar fits, Device 2 is found to have $\rho/\rho_g = 9.5$ and $v_{ac}/V_{ac} = 3.8\%$.

In Section 3.2, resonant motion is converted from μV (generated by our photodiode) to pm using the above measured values of ρ and v_{ac}/V_{ac} to calculate the applied force during any measurement, and the resulting motion of the fundamental mode. This value is then compared to the measured amplitude (in μV)

on resonance. It should be noted that because this calibration uses only mode 1 as a reference, the relative amplitude measured for each of the higher modes depends upon the position of our laser spot. AC voltages given in Section 3.2 represent the voltage experienced by the graphene, v_{ac}, so as to be independent of the particular electrical losses of our experimental setup.

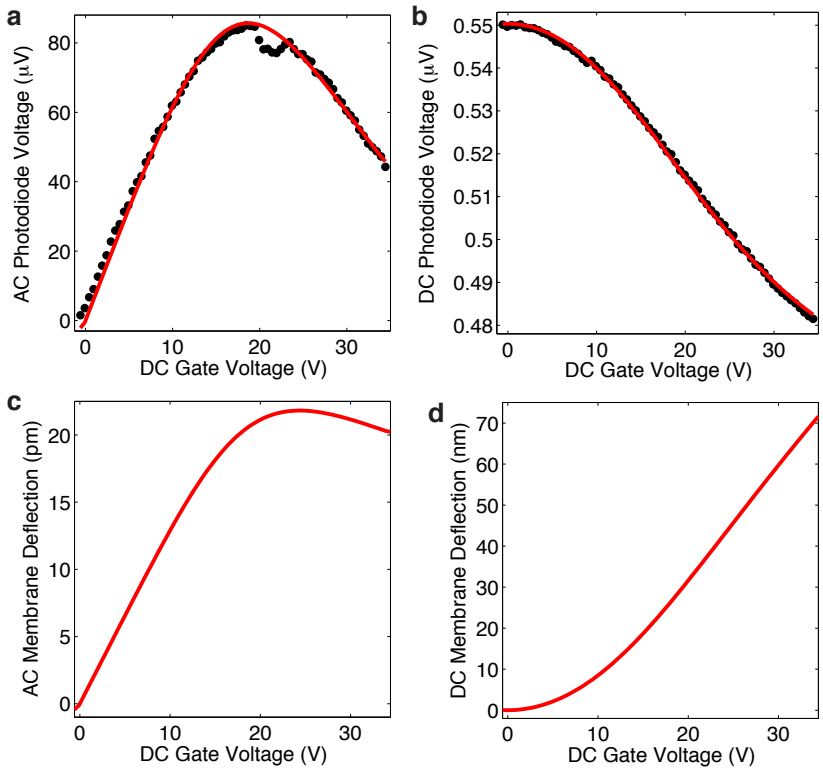

Figure 3.7: **Optical calibration for mode-coupling experiment.** (a) Measured ac reflected laser power as graphene is driven far below resonance at fixed V_{ac} and varying V_{dc}. Red line: Three-parameter fit, as described in the text. (b) Measured dc reflected laser power collected in synchrony with (a) (black points). Red line: two-parameter fit, using values taken from fit to (a). (c,d) Calculated membrane deflection at $\omega = 2\pi \times 100$kHz and $V_{ac} = 200\text{mV}_{\text{pk}}$ resulting from the fits in (a) and (b). The responsivity and transimpedance gain specified for our photodiode (New Focus 1801-fs-ac) are used to convert between measured voltage and input laser power.

3.6 Measurement of effective damping and frequency

In order to fully characterize the effects of mode coupling on the frequency and damping of mode 1, its response amplitude $|x_1|$ and phase ϕ_1 must both be measured. Below we show that when compared to the amplitude and phase of a "reference state" of the same resonator, these two numbers can be used to infer the effective damping and resonant frequency of the mode.

The equation of motion for mode 1 in the absence of nonlinearities is

$$\ddot{x} + \gamma\dot{x} + \omega_0^2 x = \frac{F}{m}e^{i\omega t} \tag{3.50}$$

where the '1' subscripts have been excluded for brevity and ω_0, γ are the natural frequency and damping. F, m are the applied electrostatic force and membrane mass. In the presence of mode coupling and Stokes (or anti-Stokes) pumping, only ω_0 and γ are altered:

$$\ddot{x} + \gamma_{\text{eff}}\dot{x} + \omega_{0,\text{eff}}^2 x = \frac{F}{m}e^{i\omega t}. \tag{3.51}$$

Assuming F is real, the driven response of mode 1 then becomes

$$x(t) = \frac{F/m}{\omega_{0,\text{eff}}^2 - \omega^2 + i\gamma_{\text{eff}}\omega}e^{i\omega t}. \tag{3.52}$$

Expressing $x(t)$ by its quadratures $\mathbb{R}\text{e}\{\text{x}\} = \text{X}\cos\omega\text{t}$ and $\mathbb{I}\text{m}\{\text{x}\} = \text{Y}\sin\omega\text{t}$, and amplitude $|x| = R$, the effective resonant frequency and damping can be determined from:

$$\omega_{0,\text{eff}}^2 = \omega^2 + \frac{FX}{mR^2} \tag{3.53}$$

$$\gamma_{\text{eff}} = -\frac{FY}{m\omega R^2}. \tag{3.54}$$

In generating Figure 3.3 (e) of Section 3.2, motion was calibrated based on a "reference" region of (ω, ω_p) space where mode coupling effects are negligible:

$\omega_p/2\pi = 22 - 22.5$MHz. Data from this region was fitted to Equation 3.52 to calibrate the amplitude of motion R (according to Section 3.4), as well as adjust the measured phase such that $X = 0$ on resonance. Equations 3.53 - 3.54 were then used to convert X, Y to $\omega_{1,\text{eff}}$, $\gamma_{1,\text{eff}}$ for each point in (ω, ω_p) space, as shown in Figure 3.8.

It should be noted that Equations 3.53 - 3.54 can easily be modified to account for a Duffing nonlinearity in the "reference" region. Slight variations in the optical detection efficiency can also be modeled quite effectively, as was necessary for Figures 3.3 (e) & 3.8 (c,d). A slow drift in the position of our laser spot resulted in a roughly linearly decreasing detection efficiency as $\omega/2\pi$ was ramped from 8MHz to 9MHz. Figure 3.9 compares the signal in our "reference" region with and without renormalizing to correct for the slowly evolving detection efficiency. This renormalization is used only in computing $\omega_{1,\text{eff}}$ and $\gamma_{1,\text{eff}}$. All other figures here and throughout this chapter depict raw data.

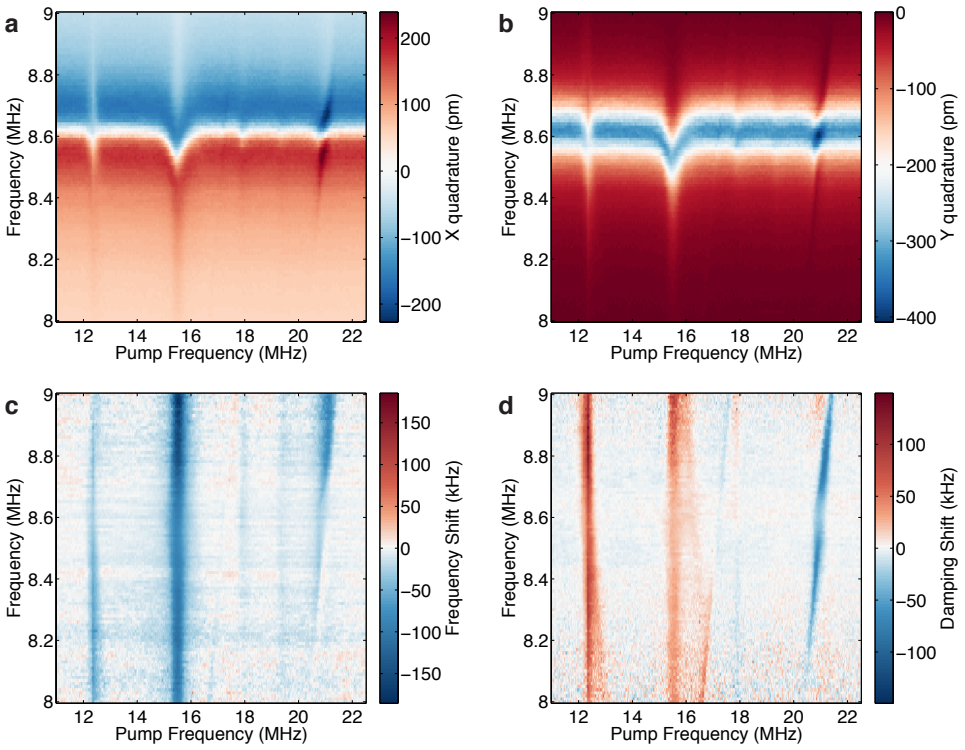

Figure 3.8: **Extraction of effective frequency and damping.** (a,b) X & Y quadrature of Device 1 motion corresponding to Figure 3.3 (a). (c,d) $\Delta\omega_1$ and $\Delta\gamma_1$ calculated from from X & Y according to Equations 3.53 - 3.54. Note that these two are ≈ 0 (by definition) in the "reference" region $\omega_p/2\pi = 22 - 22.5$MHz, as well as most other regions. In these lower panels, the color scales are symmetric about 0kHz so that zero shift appears white. The intrinsic parameter values for mode 1 are $\omega_1/2\pi = 8.62$MHz and $\gamma_1/2\pi = 150$kHz.

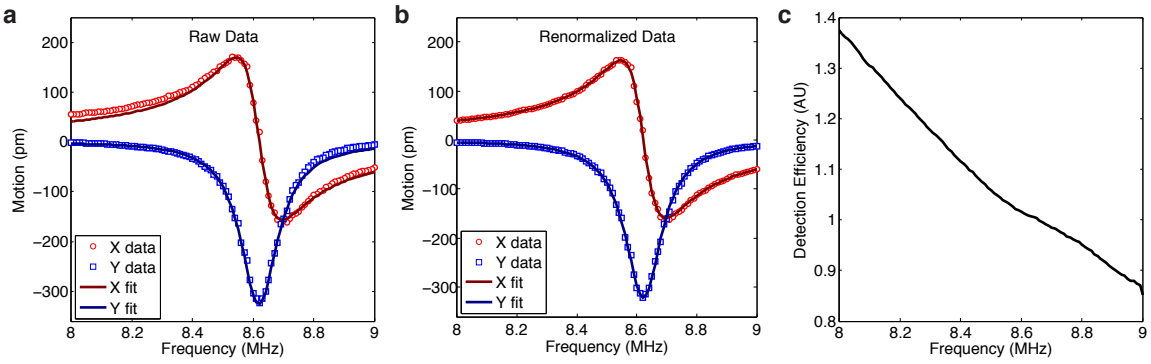

Figure 3.9: **Correction of raw data.** (a) Raw data (X & Y quadratures) compared to a fit of Equation 3.52. Discrepancies are caused by a slowly decreasing detection efficiency over time (the frequency sweep shown was performed over $\sim$ 1 hour). (b) The same data, corrected for the changing detection efficiency. The near-perfect agreement between data and model is needed to ensure $\Delta\omega_1, \Delta\gamma_1 = 0$ in this "reference" region of (ω, ω_p) space (see Figure 3.8). (c) Detection efficiency used to renormalize the data and produce Figures 3.8 (c,d) & 3.3 (e).

3.7 Additional mode coupling effects in Device 1

Measurements for Device 1 were taken at V_{dc} = 2.5V, 5V, 7.5V, 10V, and 15V. As seen in Figure 3.2 (d) of Section 3.2, significant overlap between the frequencies of modes 2,6 and their respective sidebands occurs in the range $V_{dc} = 0 - 7.5$V. Therefore coupling rates between the modes should be roughly constant in this range, which is verified in Figure 3.10. Here care was taken to ensure equivalent drive forces ($F \propto V_{dc}V_{ac}$) were applied to the pump (as well as the probe) for each V_{dc} value. At V_{dc} = 10V and above, the sideband overlap diminishes and enhancement at the pump frequency no longer occurs.

As the graphene devices studied here have two independent back-gates, several driving conditions can be realized (depicted in Figure 3.1 (a)). For the

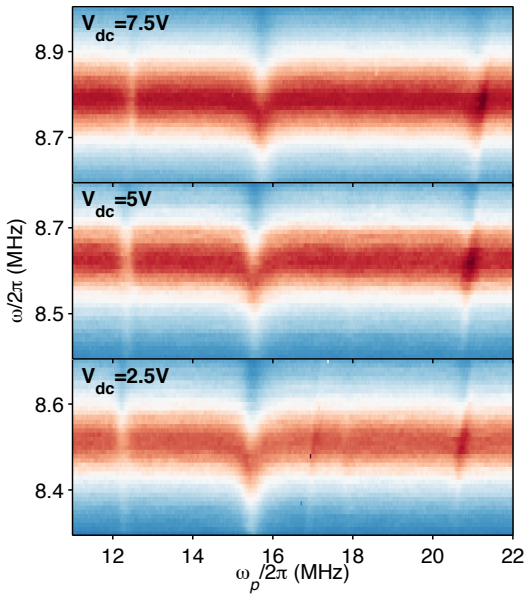

Figure 3.10: **Mode coupling in Device 1 at 3 different V_{dc} values.** Drive forces applied at the pump frequency (and probe frequency) are equal across the three data sets. Apart from a steady increase in ω_1 with V_{dc}, the coupling rates leading to amplification and cooling remain roughly constant.

results shown in Figures 3.3 & 3.10, one back-gate is driven while the other is grounded. This configuration enables efficient actuation of all 6 membrane modes, as opposed to driving both back-gates in phase (which benefits the fundamental mode) or 180° out of phase (which benefits the higher modes). Figure 3.11 shows the results of driving the back-gates out of phase in Device 1 at $V_{dc} = 10\text{V}$. Interestingly, this strong driving of mode 4 (as well as its overlap with $2 \times \omega_1$) results in strong amplification of mode 1. This coupling between modes 1 and 4 is due to the $T_{14} x_1 x_4^2$ term in the membrane Hamiltonian, Equation 3.1. Strong coupling between two mechanical modes i, j where $\omega_j = 2 \times \omega_i$ has been studied previously in carbon nanotube systems [84].

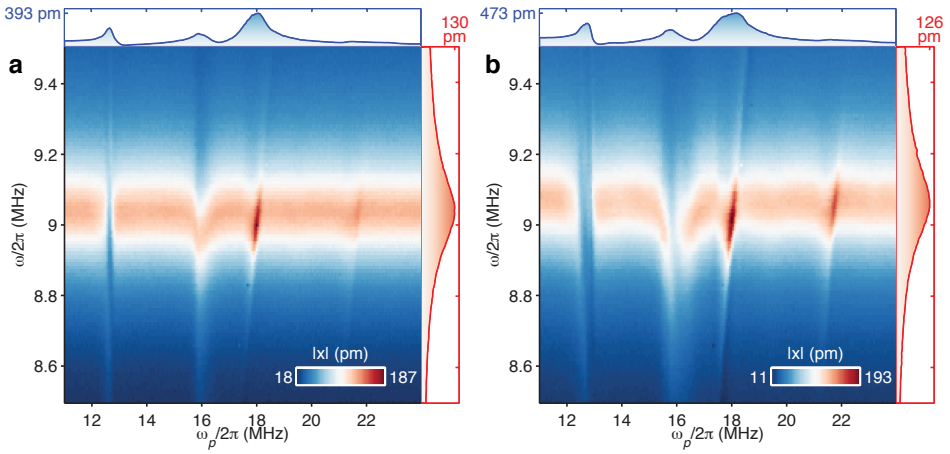

Figure 3.11: **Mode coupling measurements with back-gates driven** 180° **out of phase.** The pump voltage v_{ac} is doubled between (a) and (b). Both plots show parametric amplification at $\omega_p = 2 \times \omega_1$. For very strong pumping ((b)), there is also increased damping at $\omega_p = \omega_3 \approx 16\text{MHz}$. This is a separate effect from sideband cooling, and not yet fully understood. This feature is also seen in Figure 3.8 (d).

3.8 Large-amplitude quenching of phonon cavity and sideband mode

As discussed in Section 3.2 and seen in Figure 3.3, Device 1 exhibits quenching of the sideband amplification and cooling effects due to the large vibration amplitudes of mode 1. This is caused by nonzero couplings T_{16} and T_{61} which lead to effective cooling of either sideband mode due to motion of mode 1. The experimental data was modeled by (for the case of $\omega_c = \omega_2$, $\omega_{sb} = \omega_6$) using Equations 3.2 & 3.3 to solve for the effective frequency and damping of mode 1, $\omega_{1,\text{eff}}$ and $\gamma_{1,\text{eff}}$, while concurrently solving identical equations for $\omega_{6,\text{eff}}$ and $\gamma_{6,\text{eff}}$. In this case, mode 2 acts like a phonon cavity for mode 6, and mode 1 is pumping its red sideband $\omega_2 - \omega_6$; mode 6 is thus cooled while mode 1 is being amplified. If this process is initiated with a sufficiently small mode 1 vibration amplitude, significant amplification can occur such that $\gamma_{1,\text{eff}} \rightarrow 0$ before the sideband mode experiences much cooling (as is the case in our measurements of Device 2).

Figure 3.12 demonstrates our method for fitting the measured $\gamma_{1,\text{eff}}$, and demonstrates predicted behavior with and without quenching.

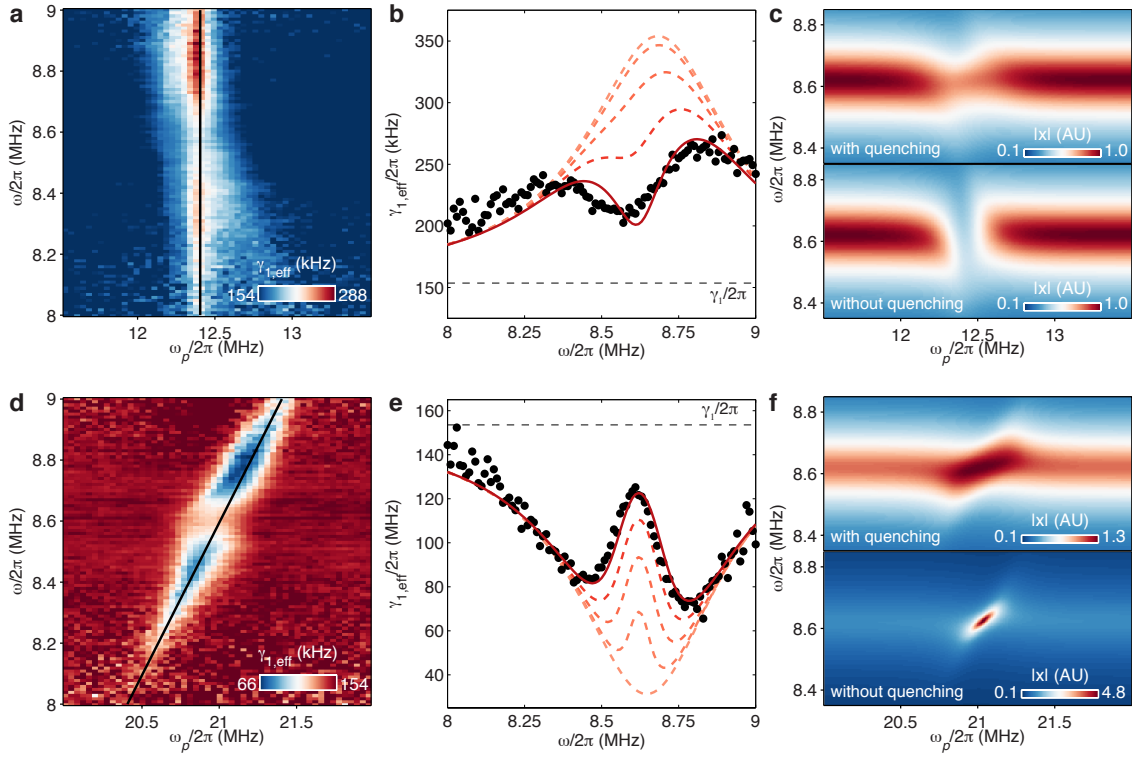

Figure 3.12: **Modeling the effective damping.** (a) The measured mode 1 damping (obtained by the analysis described in Section 3.6) during sideband cooling. (b) Fit to the data in (a). Black points represent a slice through the data in (a) at the solid black line. The fit (solid red line) has two free parameters, T_{16} and T_{26}, where the latter signifies quenching of mode 2. Dashed lines denote the same model for decreasing mode 1 amplitude (or equivalently, decreasing T_{26}) at 75%, 50%, 25%, and 0% of the experimental value. (c) Simulated data with the fit parameters from (b). Amplitudes are normalized to 1 when no cavity effects are present. (d-f) Similar results for the sideband amplification effect.

3.9 Mode coupling in a third device

The parametric cooling and amplification effects described in the previous sections have been observed in several graphene membranes of various diameters. These effects are shown in Figure 3.13 for a third device (for which optical calibration has not been performed, and so motional amplitude is reported in photodetector μV).

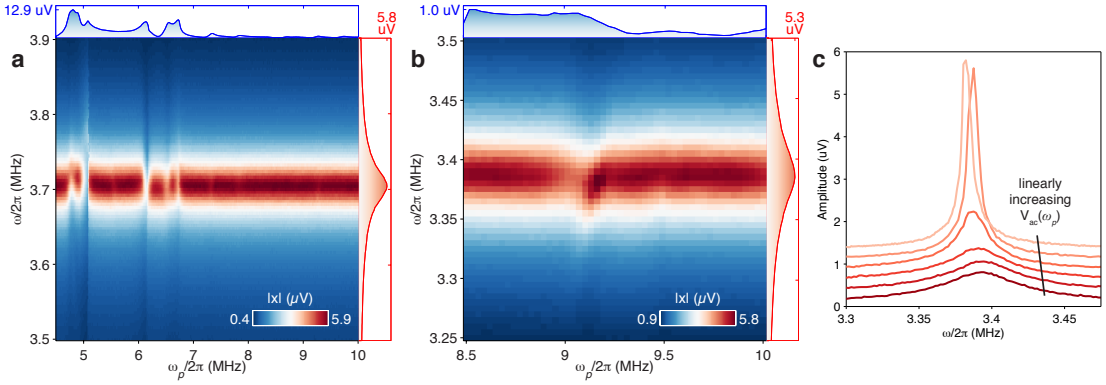

Figure 3.13: **Mode coupling in a 3rd device, diameter 16 μm.** (a) Mode coupling in this device at V_{dc} = 10V. Note the nontrivial spectrum of higher modes in the upper panel. Each mode coincides with increased damping of mode 1, suggesting sideband cooling via coupling to cavity modes in the $\omega_p/2\pi$ = 9 – 10MHz range. Modes in this range are not clearly visible (upper panel), possibly due to poor capacitive actuation to these modes. (b) Mode coupling in the same device at V_{dc} = 5V. Some sideband amplification is visible. (c) Amplification of mode 1 at V_{dc} = 5V upon pumping the sideband at $\omega_p/2\pi \approx$ 9.25MHz shown in (b).

3.10 Duffing response & nonlinear damping

As suggested by Equation 3.1, motion-induced tension modulation results in other types of mechanical nonlinearity aside from inter-modal coupling. To demonstrate this, the response of Device 1, mode 1 was measured for strong drive amplitudes at $V_{dc} = 5\text{V}$ and $V_{dc} = 10\text{V}$, as shown in Figure 3.14. Interestingly, for $V_{dc} = 5\text{V}$, the resonance peak transitions from left-leaning at intermediate drive values to right-leaning at the highest drives. The intermediate amplitude behavior can be explained by a negative Duffing coefficient generated by T_a and F_a in Equation 3.1, while the transition to right-leaning is indicative of a higher order Duffing-like term (possibly $H \propto x_a^5$ or x_a^6). In Figure 3.14 (a) and 3.14 (c), data has been modeled by a resonant frequency $\omega_{1,\text{eff}}^2 = \omega_1^2 + D_1|x_1|^2 + D_2|x_1|^3 + D_3|x_1|^4$, which reproduces the curved spine observed in the data of Figure 3.14 (a). Data in Figures 3.14 (d) and 3.14 (f) were modeled using only $\omega_{1,\text{eff}}^2 = \omega_1^2 + D|x_1|^2$.

Figure 3.14 also suggests that Device 1 undergoes nonlinear damping, as has been observed previously in graphene and carbon nanotube resonators [34]. The source of this nonlinear damping has thus far not been determined, and warrants further study. The fits shown in Figure 3.14 (c) and 3.14 (f) also include a nonlinear damping term $\gamma_{1,\text{eff}} = \gamma_1 + N|x_1|^2$, which reproduces the data well. However, the decreasing amplitude observed in Figures 3.14 (b) and 3.14 (e) may be partly due to a decreasing detection efficiency over time (the data was acquired over a span of 15 minutes), as described in Section 3.6.

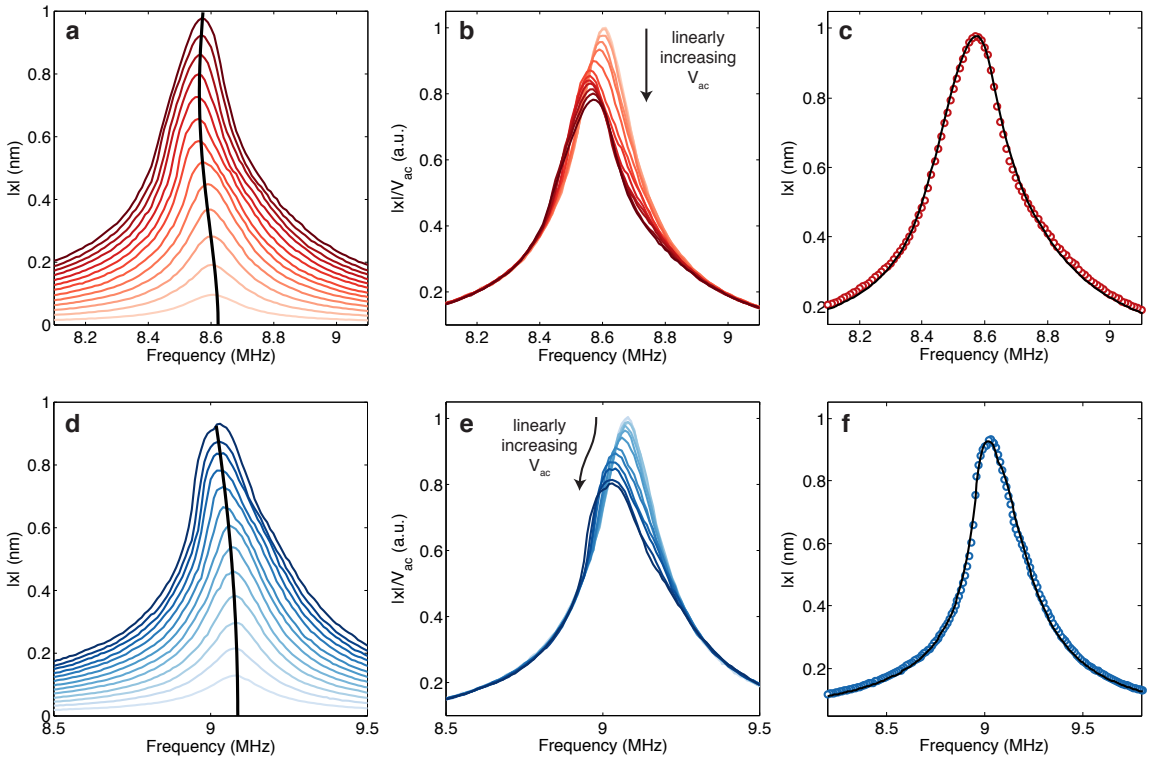

Figure 3.14: **Duffing response of Device 1.** (a) Mode 1 response as drive amplitude is ramped from v_{ac} = 4mV$_{\text{rms}}$ to 56mV$_{\text{rms}}$ (colored lines) at V_{dc} = 5V. The black central line is a spine extracted from (a) fit to the highest curve (shown in (c)). (b) The same data from (a), normalized by ac drive voltage. The decreasing peak height is indicative of nonlinear damping. (c) A fit the highest curve in (a), with Duffing terms and nonlinear damping included. (d-f) Similar data at V_{dc} = 10V and v_{ac} = 3mV$_{\text{rms}}$ to 30mV$_{\text{rms}}$.

Chapter 4

Low-power photothermal self-oscillation of bimetallic nanowires

In this chapter we investigate the nonlinear mechanics of a bimetallic, optically absorbing SiN-Nb nanowire in the presence of incident laser light and a reflecting Si mirror. Situated in a standing wave of optical intensity and subject to photothermal forces, the nanowire undergoes self-induced oscillations at low incident light thresholds of $< 1\,\mu$W due to engineered strong temperature-position (T-z) coupling. Along with inducing self-oscillation, laser light causes large changes to the mechanical resonant frequency ω_0 and equilibrium position z_0 that cannot be neglected. We present experimental results and a theoretical model for the motion under laser illumination. In the model, we solve

the governing nonlinear differential equations by perturbative means to show that self-oscillation amplitude is set by the competing effects of direct T-z coupling and $2\omega_0$ parametric excitation due to T-ω_0 coupling. We then study the linearized equations of motion to show that the optimal thermal time constant τ for photothermal feedback is $\tau \to \infty$ rather than the widely reported $\omega_0\tau = 1$. Lastly, we demonstrate photothermal quality factor (Q) enhancement of driven motion as a means to counteract air damping. Understanding photothermal effects on nano- and micro-mechanical devices, as well as nonlinear aspects of optics-based motion detection, can enable new device applications as oscillators or other electronic elements with smaller device footprints and less stringent ambient vacuum requirements.

This chapter is published online in Ref. 45.

4.1 Introduction

Self-oscillating systems (*i.e.* those that oscillate without a harmonic drive force applied) are abundant throughout the manmade and natural world. They can be observed in the sideways wobble of railway wheels [94], vertical oscillations in the payloads of jet fighter aircraft [95], instability in the mirrors of gravitational wave detectors at high laser powers [96], and cycles in predator-prey populations [97]. They have also been observed across a range of Micro-Electro Mechanical Systems (MEMS) experiments in recent years. These include: 1) MEMS resonators under the influence of thermal forces due to absorption of laser light [17, 42], 2) MEMS resonators comprising one end of a two-mirror optical cavity and experiencing radiation pressure forces [98], and 3) MEMS resonators comprising one or both legs of a Superconducting QUantum Interference Device (SQUID) experiencing magnetic forces [99, 100]. In each case, mechanical motion is coupled to some other system parameter – either (1) resonator temperature, (2) intra-cavity laser power, or (3) magnetic flux through the SQUID – in such a way that motion of the resonator modulates this parameter, which then exerts a time-delayed back-action force on the motion. Engineering this back-action force to be out-of-phase with the motion is one way to suppress thermal excitations and effectively cool a resonator into the quantum regime – this has been achieved in some systems and is a very active field of research. Coupled systems in which the back-action force is in phase, on the contrary, can be used to enhance the effective quality factor Q of the mechanical resonator, leading to potentially improved performance in MEMS-based sensors and electrical filters.

When used to sense mass, force, acceleration, or strain, MEMS resonators typically operate based on changes of their resonant frequency [2, 101–103].

Self-oscillation based on a DC (direct current) energy source would negate the need for bulky drive circuitry without affecting sensitivity to the test variable. It also enables these resonators to be used as reference oscillators for time keeping, signal processing, or sensing [104–106]. Though not as temperature-stable as traditional quartz crystal oscillators, MEMS oscillators with their smaller footprint, on-chip integrability, and heavily tailorable nonlinear properties can excel in new device applications.

4.2 Experimental & theoretical results

Micro- and nano-mechanical resonators are widely studied for applications including electro-mechanical circuit elements and sensing of ultra-weak forces [107], masses [3], and displacements [7]. An integral part of these systems is the detection method employed to readout motion, which must itself be extremely sensitive and inevitably imparts its own force on the resonator, influencing the dynamics. The phase relation between mechanical motion and the resulting detector back-action determines whether this interaction will serve to dampen vibrations or amplify them, potentially leading to self-oscillation if the detector supplies enough energy per cycle to overcome mechanical damping.

Feedback due to external amplifiers has been used to generate self-oscillation of micro-mechanical resonators [11, 24, 108–110]; in such systems the oscillation amplitude R is set either by nonlinearity of the amplifier or of the resonator. Systems in which mechanical motion influences the amount of laser light circulating in an optical cavity [17, 42, 98, 111] or magnetic flux through a Superconducting QUantum Interference Device [99, 100] (SQUID) have also been shown to self-oscillate under the right experimental conditions. In these systems R is set largely by the periodicity of the detection scheme – either $R \approx \lambda/4$ where λ is the laser wavelength or $R \approx \Phi_0/2$ where Φ_0 is the displacement needed to change the SQUID flux by one flux quantum. In the case of a mechanical resonator coupled to an optical cavity, back-action can arise either from radiation pressure or photothermal force – that is, thermally-induced deflection caused by optical absorption. The effects of these two forces are identical if the cavity resonance (with frequency Ω_c and width κ) is sufficiently broad [42, 98, 112–114]; however if κ is much smaller than the mechanical vibration frequency ω_m

the optomechanical system is said to be in the "sideband-resolved regime," and radiation-pressure effects are enhanced at laser frequencies of $\Omega_c \pm \omega_m$ [15, 115]. Radiation-pressure-based feedback with red detuning ($\Omega_c - \omega_m$) is currently one of the most promising experimental techniques for suppressing thermal motion and thereby accessing quantum behavior in mechanical systems [116]. Such low-κ optical systems can, however, be difficult to attain and miniaturize.

Photothermal feedback places less stringent requirements on the optical system (as we show in this chapter), and has been explored in a broad range of mechanical device geometries through experiment [12, 17, 41, 42, 111, 117, 118], simulation [16, 119], and theoretical studies [17, 41, 120]. While these works provide many insights into the underlying physics, some neglect the thermally-induced change in resonator equilibrium position z_0, while others neglect the change in resonant frequency ω_0. In this work we have developed bimetallic nanowires that are designed to be especially susceptible to the photothermal force – devices in which optically-induced changes to z_0 and ω_0 cannot be neglected. Temperature-position coupling dz/dT is provided by supporting bimetallic cantilevers at either end of the nanowire (shown in Fig. 4.1 (a)), and induces self-oscillation as well as changes in z_0. At room temperature these cantilevers apply an upward torque on the nanowire and change its z position when its tension changes due to thermal expansion. Temperature-frequency coupling $d\omega_0/dT$, also due to thermal expansion, produces an overall shift in ω_0 (Fig. 4.1 (c)) and modifies motion through $2\omega_0$ parametric excitation of the resonant frequency. We adapt the perturbation theory first discussed in Ref. 17, and present our results for a general optical intensity profile $g(z)$. We then linearize the governing coupled z, T equations to study nanowire behavior at laser powers below the threshold for self-oscillation.

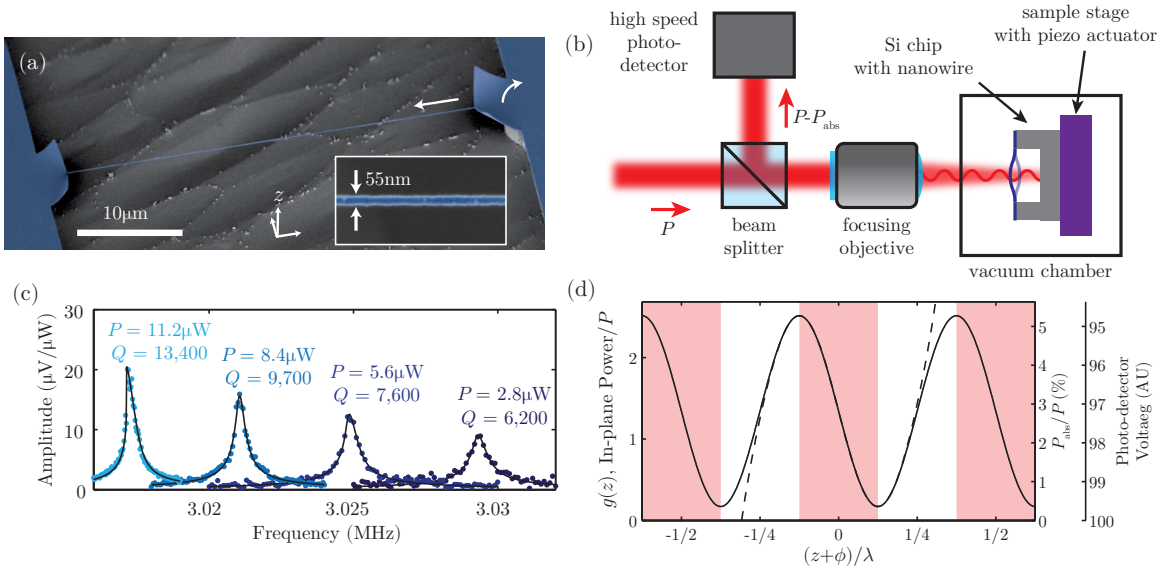

Figure 4.1: **The optomechanical system and experimental setup.** (a) False-color scanning electron micrograph of our suspended device; blue: the SiN/Nb bilayer. Arrows indicate the competing tensile force and bimetallic "torque" that provide dz/dT coupling. Inset: magnified top-down image of the nanowire. (b) The experimental setup: nanowire absorption modulates the reflected laser power, which is recorded by a high-speed photodetector. (c) Nanowire resonance at laser powers below the threshold for self-oscillation, driven inertially by a piezo actuator; solid lines are Lorentzian fits. Considerable frequency softening $d\omega_0/dT$ and Q-enhancement can be seen as P increases. (d) The optical intensity profile $g(z)$ versus distance $z + \phi$ to the Si mirror. Because the nanowire is much narrower than the incident laser beam, only $\approx 3\%$ of laser light interacts with the nanowire; of this 3%, the nanowire absorbs $\approx 70\%$. Self-oscillation occurs if the static nanowire is located in a shaded region and the power P is sufficiently high. A dashed line indicates the Taylor-series approximation for $g(z)$ used in the perturbation theory.

Our optomechanical system is depicted in Figure 4.1 (a,b). The nanowire has dimensions of $\sim (50\,\text{nm})^2 \times 40\,\mu\text{m}$ and is suspended $8\,\mu$m above a Si backplane. Incident laser light (beam diameter $d_L \approx 2.5\,\mu$m) is focused near the wire

center, and reflects off of the underlying Si to form a standing wave of optical intensity; our one-mirror optical system thus functions similarly to a very low-finesse two-mirror cavity. The total optical power (or more precisely, the electric field energy density $|\vec{E}(z)|^2$) in a plane parallel to the mirror at a distance z is given by $Pg(z)$, where $g(z)$ is the dimensionless intensity profile and P is the incident beam power; all P values given throughout this chapter signify this total beam power. Because the nanowire is extremely narrow, it covers only $\approx 3\%$ of the incident beam by area and can therefore be assumed not to influence $g(z)$. It does, however, absorb a small portion of the local power P_{abs}, and nanowire motion generates fluctuations in the reflected laser beam that can be measured using a high-speed photodetector. The detected signal is proportional to $P - P_{\text{abs}}$, as shown in Fig. 4.1 (d). This detection method has the benefit of utilizing the same light which induces self-oscillation, but is highly nonlinear for oscillation amplitudes $R \gtrsim \lambda/8$, where $\lambda = 660\,\text{nm}$ is the laser wavelength used. If the optical field profile $g(z)$ is known, this detector nonlinearity can be used to deduce the absolute size of mechanical motion (see Section 4.8).

Self-oscillation of the nanowire is shown in Figure 4.2. Measured in the time domain (Fig. 4.2 (a)), purely sinusoidal motion with $R \approx \lambda/4$ results in a detected signal that saturates as z traverses the extremes of $g(z)$. This results in detected harmonics of the vibration frequency that can readily be measured in the frequency domain. Figure 4.2 (b) shows the nanowire motion as measured by a multi-channel lock-in amplifier whose reference frequency is centered at the resonant frequency $\omega_0 \approx 2\pi \times 3\,\text{MHz}$ with a 10 kHz bandwidth for three different laser powers; the three harmonics shown ($\omega_0, 2\omega_0, 3\omega_0$) were measured simultaneously. The reference frequency was adjusted at each power to follow the resonance. Nanowire motion is plotted as X and Y quadratures, or in-phase

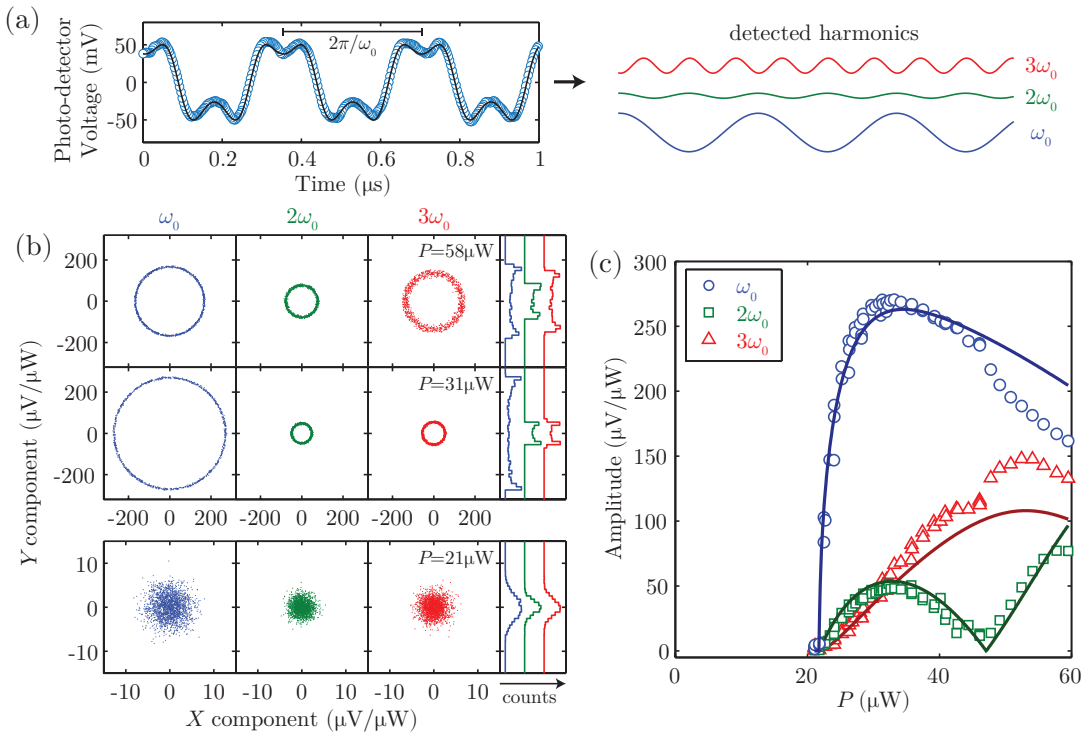

Figure 4.2: **Photothermal self-oscillation.** (a) Measured photo-detector signal during nanowire self-oscillation (circles), and its decomposition into Fourier components (solid lines). Although the nanowire motion is a near-pure sinusoid, the nonlinear optical readout results in detected harmonics at integer multiples of the oscillation frequency. (b) Phase portraits of undriven nanowire motion as measured in the frequency domain by a multi-channel lock-in amplifier centered about the resonant frequency. X and Y denote cosine and sine components of motion. The critical power needed for self-oscillation is $P_{\text{crit}} = 22\,\mu$W. Data below this power (lowest row) is a combination of thermal motion and detector noise, while data above this power (upper rows) has a well-defined nonzero amplitude. (c) Data points: amplitudes of the self-oscillation signals shown in (b) versus laser power P. Solid lines are a best fit based on the IPT model described in the text.

and out-of-phase components relative to a fixed phase. The lower panel displays nanowire motion just below the critical power ($P_{\text{crit}} = 22\,\mu\text{W}$), which is a combination of thermal motion and electrical noise about the origin; this has the expected Gaussian distribution. As P is increased above P_{crit}, all three harmonics demonstrate sharply-defined nonzero amplitudes. This optically-induced motion has a phase that randomly cycles through all possible angles as time progresses at nearly constant amplitude. All plots show 1,000 data points except for the lower panels which each contain 2,000 points. Figure 4.2 (c) shows the amplitude of these harmonics ($\sqrt{X^2 + Y^2}$) for many values of P. Solid lines are a best fit (with a total of 4 free parameters) based on the model described below. Deviations of the fit at high powers could be due to aberrations of the optical plane wave $g(z)$ caused by the nanowire, as studied previously by Refs. 118, 121. All measured signals are normalized by P, the laser power used.

The governing differential equations for the position and temperature of our photothermal system are [17]:

$$\ddot{z} + \gamma\dot{z} + \omega_0^2(1 + CT)(z - DT) = 0 \tag{4.1}$$

$$\dot{T} + \frac{1}{\tau}T = PAg(z) \tag{4.2}$$

Here ω_0, γ are the intrinsic resonant frequency and damping of the nanowire. T denotes the temperature above ambient and C, D are the changes in resonator frequency and position per unit temperature, respectively. The second equation is Newton's law of cooling, where τ denotes the thermal diffusion time constant, and the right-hand-side describes heat absorption from the incident laser. A includes the thermal mass and optical absorption of the nanowire, as well as its $\approx 3\%$ area coverage of the incident laser beam. Detailed calculations of the thermal parameters in Eqs. 4.1 & 4.2 based on the materials and dimensions of

our system are presented in Section 4.6.

Because the nanowire does not interact appreciably with the incident laser, we can approximate the optical field to be:

$$g(z) = \alpha + \beta \sin^2\left(\frac{2\pi(z+\phi)}{\lambda} - \frac{\pi}{4}\right) \tag{4.3}$$

Here α, β are determined by the reflection coefficient of the Si back-plane, and ϕ is the $P = 0$ nanowire position within the standing wave. The factor of $-\pi/4$ is added to center the self-oscillation region (negative dg/dz region, Fig. 4.1 (d)) about $z + \phi = 0$. The total mirror-nanowire distance is $z + \phi + (\lambda/2)(n - 1/4)$, where the integer n is irrelevant to our measurements.

In other device geometries, large mechanical resonators can generate significant internal and external optical reflections, producing a Fabry-Perot interference effect which results in $g(z)$ having sharper peaks and wider valleys, or skewing its peaks left or right. For this reason we present our theoretical results for a general intensity profile $g(z)$. In all cases, however, $g(z)$ is periodic in $\lambda/2$.

During self-oscillation, the resonator position is well modeled by $z(t) = z_0 + R\cos(\omega t)$ where z_0 is the temperature-dependent equilibrium position. This value can be estimated by solving Eqs. 4.1 & 4.2 for the case of a static nanowire, which give the implicit equation $z_0 = \tau DPAg(z_0)$. Near $P = 0$ this formula has only one solution for z_0, but more solutions become available as P increases. For high enough P values, solutions nearest $z = 0$ can cease to be valid; this suggests that the static wire exhibits discontinuous jumps in z_0 as P is increased quasi-statically. The static solution to Eqs. 4.1 & 4.2 is studied further in Section 4.4. While the static solution for z_0 (and the corresponding temperature $T_0 = z_0/D$) is a useful starting point for analyzing the self-oscillating nanowire,

in what follows we will show that typical oscillation amplitudes R produce sizeable changes in T_0 (and z_0).

Although Eqs. 4.1-4.3 are nonlinear and cannot be solved exactly, perturbative methods can be applied. Here we employ the Poincaré-Lindstedt method, which requires scaling γ, C, and D in Eq. 4.1 by a small dimensionless parameter $\varepsilon \ll 1$. Eqs. 4.1 & 4.2 can then be solved for $z(t), T(t)$, and ω_1 (the self-oscillation frequency) to any desired order in ε. The method also requires approximating $g(z)$ by the first few terms of its Taylor series. We expand $g(z)$ about $z + \phi = 0$ and keep enough terms such that the optical field is accurately modeled over an entire period $|z + \phi| < \lambda/4$:

$$\begin{aligned} g(z) \approx k_0 + k_1(z+\phi) + k_3(z+\phi)^3 \\ +k_5(z+\phi)^5 + k_7(z+\phi)^7 \end{aligned} \tag{4.4}$$

where $k_0 = (\alpha + \beta/2)$, $k_1 = -2\pi\beta$, $k_3 = (16/3)\pi^3\beta$, $k_5 = -(64/15)\pi^5\beta$, and $k_7 = (512/315)\pi^7\beta$. A comparison of this approximation with the exact $g(z)$ is shown in Fig. 4.1 (d). The perturbation theory is presented in its entirety in Section 4.3, but the main results are given below.

Using Eq. 4.4 and solving Eqs. 4.1 & 4.2 to order ε^1 gives the following equation for R:

$$0 = c_0 + c_1R^2 + c_2R^4 + c_3R^6 \tag{4.5}$$

where

$$
\begin{aligned}
c_0 &= \frac{\omega_1^2 D}{1+\omega_1^2\tau^2}\, g_{z_0}^{(1)} + \frac{\gamma}{\tau^2 PA} \\
c_1 &= \frac{\omega_1^2 D}{1+\omega_1^2\tau^2}\, \frac{g_{z_0}^{(3)}}{2^2 1!2!} - \frac{\omega_0^2 C}{1+4\omega_1^2\tau^2}\, \frac{g_{z_0}^{(2)}}{2^1 0!2!} \\
c_2 &= \frac{\omega_1^2 D}{1+\omega_1^2\tau^2}\, \frac{g_{z_0}^{(5)}}{2^4 2!3!} - \frac{\omega_0^2 C}{1+4\omega_1^2\tau^2}\, \frac{g_{z_0}^{(4)}}{2^3 1!3!} \\
c_3 &= \frac{\omega_1^2 D}{1+\omega_1^2\tau^2}\, \frac{g_{z_0}^{(7)}}{2^6 3!4!} - \frac{\omega_0^2 C}{1+4\omega_1^2\tau^2}\, \frac{g_{z_0}^{(6)}}{2^5 2!4!}
\end{aligned}
$$

Here we have introduced $\omega_1^2 = \omega_0^2(1 + CT_0)$ as the new resonant frequency and $g_{z_0}^{(n)}$ as the n^{th} derivative of $g(z)$ evaluated at $z = z_0$. This result is hereafter referred to as the First Order Perturbation Theory (FOPT) solution. The number of terms in Eq. 4.5 increases if more terms are kept in the Taylor expansion Eq. 4.4 (following the clear pattern in $c_0 \ldots c_3$), however the terms shown are sufficient to accurately model our experimental data.

Eq. 4.5 indicates that R is influenced by both the temperature-position coupling D and the temperature-frequency coupling C. Interestingly, D influences self-oscillation via temperature fluctuations at the oscillation frequency ω_1, while C does so via temperature fluctuations at $2\omega_1$; the effect of C is thus equivalent to parametric $2\omega_1$ excitation of the resonant frequency. Eq. 4.5 also suggests that as z_0 changes, C dominates near points of $g(z_0)$ with even symmetry (extrema) while D dominates near points with odd symmetry (inflection points). The threshold for self-oscillation occurs when $R = 0$ in Eq. 4.5; this leads to $c_0 = 0$ and gives a critical laser power of:

$$
P_{\text{crit}} = -\frac{\gamma\left(1+\omega_1^2\tau^2\right)}{\omega_1^2\tau^2 DA g_{z_0}^{(1)}} \tag{4.6}
$$

This expression reveals the source of low critical power in our nanowire: a combination of low thermal mass A, long thermal time constant $\omega_1\tau \approx 400$, and

large coupling $D = 1.64\,\mathrm{nm/°C}$ afforded by our cantilevers. Further, because γ, D, A are all positive, a negative optical gradient is needed for self-oscillation. While the sensitivity of P_{crit} on τ is rather weak for $\omega_1\tau > 1$, it is noteworthy that short time constants $\tau \to 0$ inhibit self-oscillation. We revisit this later in this section when we discuss operation of the wires in the presence of N_2 gas. For the case $D = 0, C \neq 0$ Eq. 4.5 still supports limit cycle oscillations, but has no $R = 0$ solution. This suggests that $z(t) = z_0$ remains a stable equilibrium point even for $P > P_{\mathrm{crit}}$, and only initial conditions of $(z, \dot{z})$ sufficiently close to $z(t) = z_0 + R\cos(\omega t)$ will lead to oscillation. One can therefore draw an attractor diagram to describe which initial conditions lead to limit cycle behavior and which approach the stable equilibrium [42].

As mentioned above, FOPT predicts a change in the time-averaged temperature of the nanowire due to self-oscillation. This addition to T_0 is

$$\delta T_0 = -T_0 + \tau PA \sum_{n=0}^{3} \frac{R^{2n} g_{z_0}^{(2n)}}{2^{2n}(n!)^2} \tag{4.7}$$

The nanowire equilibrium position thus relocates to $z_0 = D(T_0 + \delta T_0)$ during self-oscillation. Although one could proceed to order ε^2 in perturbation theory to account for this equilibrium shift, the resulting algebraic expressions quickly become cumbersome. An approach that is easier to implement and was used to fit the data in Fig. 4.2 (c) is to recursively perform FOPT while updating T_0 and z_0 with successive δT_0 values. Starting with the static nanowire solution ($z_0 = \tau DPAg(z_0)$), R and δT_0 are iteratively calculated until R converges on a fixed value and δT_0 converges on zero. This scheme is hereafter referred to as Iterated Perturbation Theory (IPT). We find in practice that IPT converges most reliably if δT_0 is multiplied by a small scaling factor (0.05 was used) before being added to T_0; convergence typically occurs within 20-100 iterations.

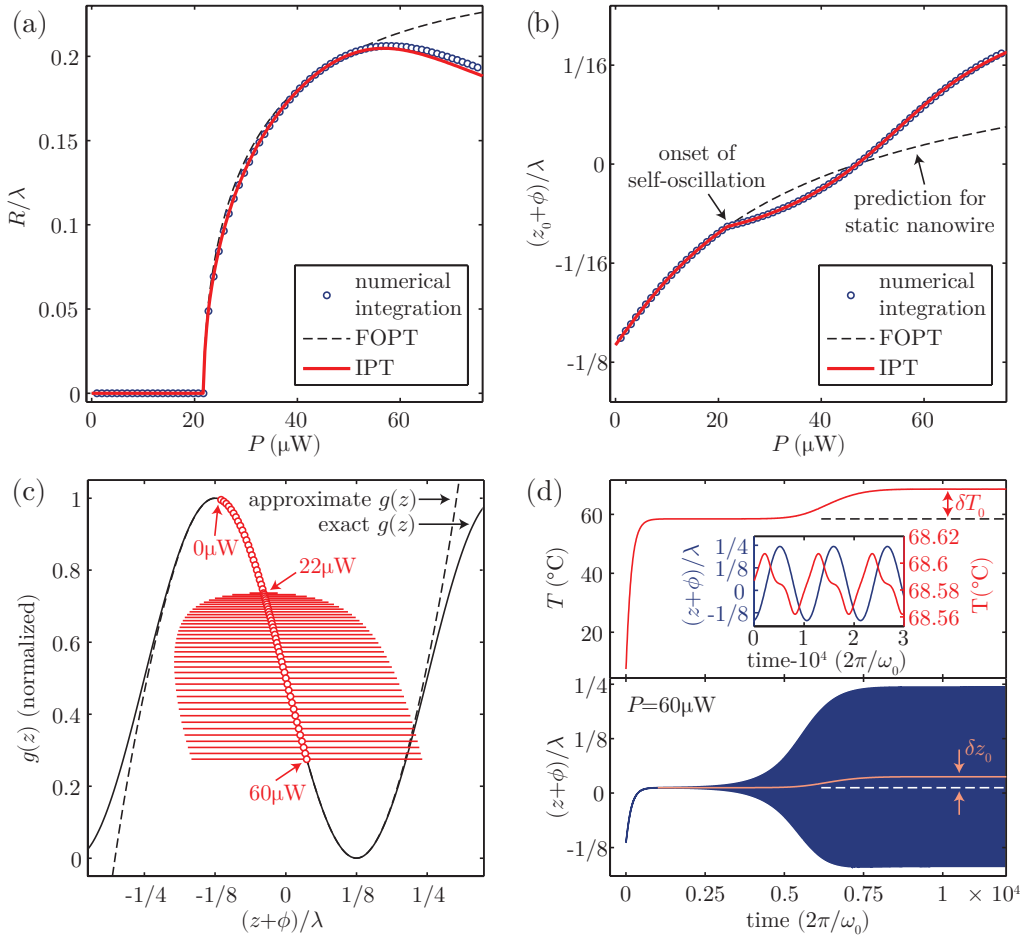

Figure 4.3: **Detailed behavior of the nanowire according to fits of the experimental data.** (a,b) Comparison of the oscillation amplitude R and equilibrium position z_0 calculated by perturbation theory and numerical integration, with $\phi/\lambda = -0.114$. Note that $z_0 = 0$ at $P = 0$. The shift in z_0 due to self-oscillation is clearly visible in (b). (c) Nanowire position within the optical field $g(z)$ as P increases. Red points (spaced every $1\,\mu$W) indicate the changing z_0 value, while horizontal lines indicate the extent of R. (d) Numerical integration results at $P = 60\,\mu$W with the initial condition $(z, \dot{z}, T) = (0, 0, 0)$; only the upper and lower envelopes of oscillation are shown. In the lower panel, a solid line signifies the peak-peak moving average, which is an indication of z_0. The shift in z_0 after $t = 5 \times 10^3$ closely follows the trend in $T(t)$ shown in the upper panel. Inset: magnified image of these results near $t = 10^4$, showing the harmonic content of $z(t)$ and $T(t)$.

A comparison of FOPT, IPT, and numerical integration of Eqs. 4.1–4.3 is shown in Figure 4.3 (a,b). The parameters used are derived from the IPT fit to experimental data in Fig. 4.2 (c) – in this fit the only free parameters were ϕ, τ, d_L, and an overall vertical scaling factor. It should be noted that while IPT reproduces the results of numerical integration almost exactly, the former required only ~1 second of computation time while the latter required 4 – 5 hours. Fig. 4.3 (c) shows the nanowire position as it moves through the optical field. The deviation of z_0 away from its static value due to δT_0 is clearly visible in Fig. 4.3 (b). Interestingly, z_0 trajectories from numerical integration and static theory intersect at $z_0 + \phi = 0$ – *i.e.* at the inflection point of $g(z)$; here the odd symmetry of $g(z)$ results in $\delta T_0 = 0$ in Eq. 4.7. The inflection point is crossed by z_0 at $P \approx 47\,\mu$W, while the maximum R value occurs at the slightly higher power of $P \approx 56\,\mu$W.

As shown in the numerical integration results of Fig. 4.3 (d), self-oscillation requires roughly 10^4 oscillation cycles to reach steady state at $P = 60\,\mu$W. We note that this "equilibration time" drastically increases for P values approaching $P_{\text{crit}} = 22\,\mu$W; a maximum of 3×10^5 cycles were required just above the transition. Also shown in Fig. 4.3 (d), the shift $\delta z_0 = 0.0251\lambda$ due to self-oscillation exactly matches the observed change in temperature $\delta T_0 = \delta z_0 / D = 10.1°$C, where $D = 1.64\,$nm/°C for this system. The numerical results in the Fig. 4.3 (d) inset show that during self oscillation $z(t)$ is a nearly pure tone at frequency ω_1. A Fourier series fit to this data (not shown) reveals that the next largest harmonic component is $2\omega_1$, with 0.001% the amplitude of ω_1 motion. It is the pureness of this tone that leads to the excellent agreement between numerical integration and IPT – after all the perturbation theory is predicated on the assumption $z(t) = z_0 + R\cos(\omega_1 t)$. Numerical results for $P > 60\,\mu$W reveal that higher harmon-

ics of the ω_1 motion grow steadily as P increases ($2\omega_1$ reaching 0.004% at 80 μW), possibly explaining the growing deviation from IPT seen in Fig. 4.3 (a). The oscillation frequency in the Fig. 4.3 (d) inset is $0.93\,\omega_0$, in close agreement with the expected $\omega_1 = \omega_0\sqrt{1+CT_0} \approx 0.92\,\omega_0$, where $C = -0.0022$ and $T_0 = 68.58$°C. The 1% increase in frequency is likely due to ω_2, the ϵ^1-order correction to the oscillation frequency, which is calculated in Section 4.3.

Perturbation theory can also be used to predict whether the onset of self-oscillation will be exhibit hysteresis. Such behavior is referred to as a subcritical Hopf bifurcation, and would manifest as a continuation of stable self-oscillation for some range of powers as P is decreased below P_{crit}. The distinction between a hysteretic or non-hysteretic transition (subcritical or supercritical bifurcation) depends upon whether c_1 in Eq. 4.5 is negative or positive. Therefore

$$\frac{\omega_1^2 D g_{z_0}^{(3)}}{1+\omega_1^2\tau^2} < \frac{2\omega_0^2 C g_{z_0}^{(2)}}{1+4\omega_1^2\tau^2} \tag{4.8}$$

is the necessary condition for hysteresis. Because $C < 0$ in this experiment, we would expect hysteretic behavior when z_0 is near a maximum of $g(z)$. The width of the hysteresis region (*i.e.* how low P can be while still maintaining self-oscillation) is calculated in Section 4.5.

Lastly, we focus on the behavior of our nanowire for laser powers $P < P_{\text{crit}}$. Since the vibration amplitude in this case is typically much smaller than $\lambda/4$, it suffices to approximate $g(z)$ by a linear expansion about $z = z_0$ in Eq. 4.2: $g(z) \approx g(z_0) + g_{z_0}^{(1)}(z - z_0)$. Furthermore, we can neglect any time-dependent CT terms in Eq. 4.1. This then leads to the linearized equations

$$\ddot{x} + \gamma\dot{x} + \omega_1^2(x - Du) = f_d e^{i\omega t} \tag{4.9}$$

$$\dot{u} + \frac{1}{\tau}u = PAg_{z_0}^{(1)}x \tag{4.10}$$

where we have introduced the new variables $x = z - z_0$, $u = T - T_0$ and added the driving term f_d at frequency ω. In this linearized system we can safely use the complex solutions $x = \tilde{x}e^{i\omega t}$ and $u = \tilde{u}e^{i\omega t}$. Based on Eq. 4.10, these are related by $u = x(\tau PAg_{z_0}^{(1)})/(1 + i\omega\tau)$. Substituting this into Eq. 4.9 and collecting real and imaginary terms, one can recast the mechanical system as $\ddot{x} + \gamma_{\text{eff}}\dot{x} + \omega_{\text{eff}}^2 x = f_d e^{i\omega t}$ where the effective resonant frequency ω_{eff} and damping γ_{eff} are:

$$\omega_{\text{eff}}^2 = \omega_1^2\left(1 - \frac{\tau DPAg_{z_0}^{(1)}}{1 + \omega^2\tau^2}\right) \tag{4.11}$$

$$\gamma_{\text{eff}} = \gamma + \frac{\omega_1^2\tau^2 DPAg_{z_0}^{(1)}}{1 + \omega^2\tau^2} \tag{4.12}$$

Firstly, we note that the photothermal terms in ω_{eff} constitute a roughly 1 part in 10^6 correction for the experimental parameters used in this work; thus to very good approximation $\omega_{\text{eff}} = \omega_1$. Next, we should expect self-oscillation to occur when $\gamma_{\text{eff}} = 0$. Substituting $P = P_{\text{crit}}$ from perturbation theory (Eq. 4.6) and $\omega = \omega_1$ indeed gives $\gamma_{\text{eff}} = 0$, showing compatibility of these two models. Interestingly, the photothermal damping shift on resonance is $\Delta\gamma = |\gamma_{\text{eff}} - \gamma| \propto \frac{\tau^2}{1+\omega_1^2\tau^2}$, which increases monotonically as $\tau \to \infty$. Long time constants $\omega_1\tau \gg 1$ therefore strengthen the photothermal effect. This can also be seen by setting $\frac{1}{\tau} = 0$ in Eq. 4.10, which results in $u \propto ix$. In this case, u is perfectly out of phase with x, meaning it contributes entirely to damping in Eq. 4.9.

These results appear to be counter to those of previous theoretical studies which model the photothermal effect as a time-delayed back-action force $F(x)$ that responds to changes in x after a time constant τ [41, 42]. Such a model produces the result $\Delta\gamma \propto \frac{\tau}{1+\omega^2\tau^2}\frac{dF}{dx}$, which is maximized (in magnitude) when $\omega\tau = 1$ and vanishes as $\tau \to \infty$. The discrepancy here lies in dF/dx. Adapting our Eqs. 4.9 & 4.10 to such a model reveals that the thermal force magnitude (*i.e.* the asymptotic value after a change in x) is $F(x) = kDu = kD\tau PAg_{z_0}^{(1)}x$, where k

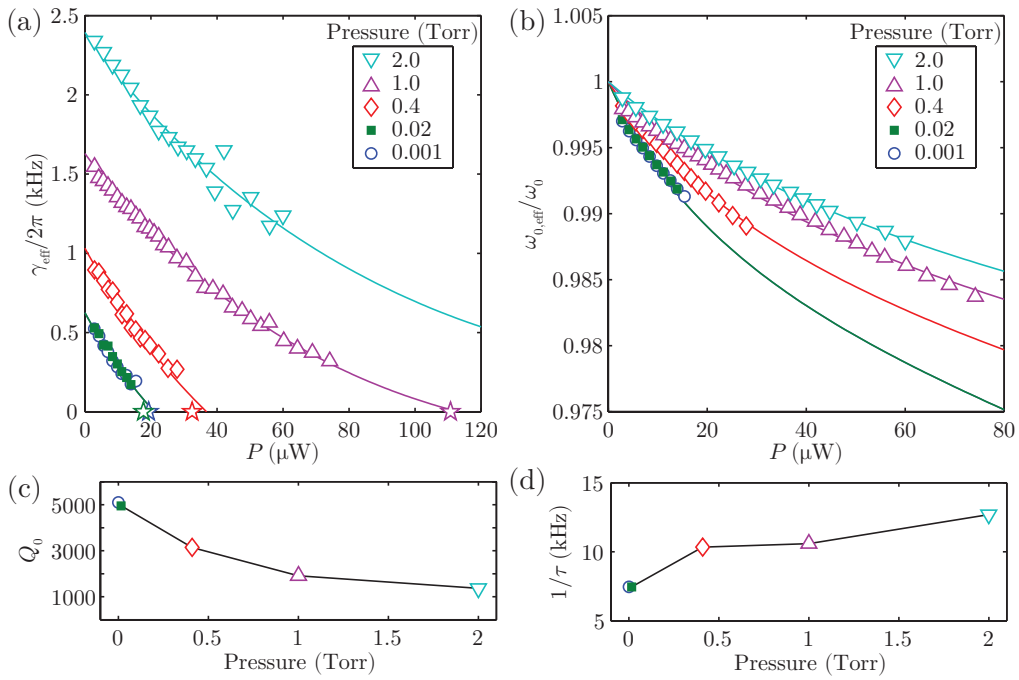

Figure 4.4: **Nanowire behavior for $P < P_{crit}$ under various N_2 pressures.** (a,b) Nanowire effective damping γ_{eff} and resonant frequency ω_{eff}. These values were obtained from Lorentzian fits to piezo-driven resonance peaks such as those shown in Fig. 4.1 (c). Stars in (a) indicate the measured onset of self-oscillation. Solid lines are fits to Eqs. 4.11 & 4.12. (c) Q factors at $P = 0$ extrapolated from fits in (a,b). (d) Thermal diffusion rate $1/\tau$ versus gas pressure.

is the mechanical spring constant. This then leads to $\Delta\gamma \propto \frac{\tau^2}{1+\omega^2\tau^2}$, in agreement with our earlier result.

We have experimentally tested Eqs. 4.11 & 4.12 for several values of γ as shown in Figure 4.4. In these measurements γ was varied by introducing pure N_2 gas into our sample test chamber; doing so added drag to the nanowire motion, resulting in higher intrinsic damping γ and lowered Q factors (Fig. 4.4 (c)). All preceding measurements were performed with pressure $\ll 10^{-3}$ Torr. The fits shown in Fig. 4.4 (a,b) were constrained at the lowest two pressures

to maintain consistent thermal parameters with the fit in Fig. 4.2 (c). At higher pressures τ was allowed to vary, as nanowire interaction with ambient gas likely increases its thermal dissipation rate. The laser waist diameter d_L and initial optical field position ϕ were also allowed to differ from Fig. 4.2 (c) as each change in pressure required manual refocusing, and the roughness of the Si back-plane led to changes in ϕ based on exact laser positioning. Here $\phi/\lambda = 0.044$ compared to the value of -0.114 in Fig. 4.2 (c); $d_L = 2.5\,\mu$m for the two highest pressures and $d_L = 2.0\,\mu$m for all lower pressures.

Curvature in the γ_{eff} and ω_{eff} fits is due to the changing equilibrium position z_0 as P increases, and the resulting change in $g^{(1)}_{z_0}$. Because of this curvature, the γ_{eff} trajectory for 2.0 Torr is not expected to enter self-oscillation at higher P values. It is however possible that if z_0 can extend to the next negative region of $g^{(1)}_{z_0}$, near $z + \phi = \lambda/2$, P would be large enough to support self-oscillation. We note that for the four values of pressure where self-oscillation is seen, the two lowest pressures yield $P_{\text{crit}} \approx 22\,\mu$W identical to the value with no N_2 gas added, and are consistent with the Q value seen with no added gas. For the case of the two higher pressures, 0.4 Torr and 1 Torr, the introduction of gas increases the damping (higher γ_{eff}) and shortens the τ, requiring an additional power to overcome damping. Above this pressure, self-oscillation cannot be reached in our present setup. Even so, the results of Fig. 4.4 demonstrate the capability of photothermal feedback to counteract air damping at low pressures. Such optical Q-enhancement could lower the stringent vacuum requirements of typical micro-electro-mechanical device applications.

We have presented an experimental and theoretical study of photo-thermal feedback in mechanical nanowires. While the device tested self-oscillates un-

der the illumination of a $22\,\mu$W laser beam, only $\sim$ 3% of this beam is incident on the ultra-fine nanowire – suggesting that incident powers of $< 1\,\mu$W are ultimately necessary to induce motion. This is significantly lower than the $300\,\mu$W to few mW required in previously studied free-space photothermal structures [17, 118, 122], and lower still than the $\approx 10\,\mu$W reported for an optical-cavity-coupled photothermal structure [42], where the two-mirror cavity results in much higher optical field gradients dg/dz. The low power needed in our system is attributable to the low thermal mass of the nanowire and large temperature-position coupling D afforded by the supporting cantilevers. A simple beam-theory calculation suggests that D scales with cantilever length L and width w as L^3/w (see Section 4.7), suggesting that even stronger photothermal effects can readily be achieved. We have observed that the equilibrium position z_0 of this system is strongly tunable with incident laser power and can drastically affect nanowire dynamics. Self-oscillation in this system is due in part to temperature oscillations at the vibration frequency ω_1 and to parametric $2\omega_1$ oscillations of the resonant frequency. The perturbation theory used here can readily be adapted for systems in which micro-mechanical resonators are coupled to magnetic SQUID circuits, optical cavities, or other periodic external systems.

It is well established that a self-oscillating system can become entrained if a sufficiently strong driving force is applied – *i.e.* the system will oscillate at the driver frequency rather than its own natural frequency [111, 123–125]. Such a system is promising for a number of electro-mechanical applications, including narrow bandpass filters and related electrical signal processing devices. Although we have observed such behavior in our nanowires (not shown here), further work is needed to extend the perturbation theory to predict the entrainment bandwidth as a function of driver strength and laser power.

4.3 Perturbation theory for photothermal self-oscillation

The governing equations of motion are:

$$\ddot{z} + \gamma\dot{z} + \omega_0^2(1 + CT)(z - DT) = 0 \tag{4.13}$$

$$\dot{T} + \frac{1}{\tau}T = APg(z) \tag{4.14}$$

$$g(z) = \alpha + \beta \sin^2\left(\frac{2\pi(z + \phi)}{\lambda} - \frac{\pi}{4}\right) \tag{4.15}$$

Eqs. 4.13 & 4.14 have the static solution $z_0 = \tau DAPg(z_0)$ and $T_0 = z_0/D$. We can define a new coordinate system as deviations from this equilibrium $x = z - z_0$ and $u = T - T_0$, which leads to:

$$\ddot{x} + \gamma\dot{x} + \omega_0^2(1 + CT_0 + Cu)(x - Du) = 0 \tag{4.16}$$

$$\dot{u} + \frac{1}{\tau}u = -\frac{1}{\tau}T_0 + APg(x + z_0) \tag{4.17}$$

$$g(x + z_0) = \alpha + \beta \sin^2\left(\frac{2\pi(x + z_0 + \phi)}{\lambda} - \frac{\pi}{4}\right) \tag{4.18}$$

where we have introduced $x_0 = \phi - z_0$. For convenience we now rescale our units of time and displacement such that the resonant frequency $\omega_0 = 1$ and laser wavelength $\lambda = 1$:

$$\ddot{x} + \frac{1}{Q}\dot{x} + (1 + CT_0 + Cu)(x - D'u) = 0 \tag{4.19}$$

$$\dot{u} + \frac{1}{\tau'}u = -\frac{1}{\tau'}T_0 + A'Pg(x + z_0) \tag{4.20}$$

$$g(x + z_0) = \alpha + \beta \sin^2\left(2\pi(x + z_0 + \phi) - \frac{\pi}{4}\right). \tag{4.21}$$

Here the quantities x, z_0, ϕ are now expressed in units of λ and we have introduced the quality factor $Q = \omega_0/\gamma$. Furthermore, we have defined $D' = D/\lambda$, $\tau' = \tau\omega_0$, and $A' = A/\omega_0$. Hereafter we will work exclusively with these rescaled parameters, and for brevity we will not write the primes.

In performing the perturbation theory, we will be required to approximate $g(x+z_0)$ by a polynomial. We choose to expand $g(x+z_0)$ in a Taylor series about $x+z_0 = -\phi$ so that the coefficients of our series are independent of ϕ. We will truncate this series at $N+1$ terms, and refer to the truncated series as $h(x) \approx g(x+z_0)$:

$$h(x) = \sum_{n=0}^{N} \frac{g^{(n)}(-\phi)}{n!}(x+z_0+\phi)^n = \sum_{n=0}^{N} k_n (x+z_0+\phi)^n \tag{4.22}$$

where $g^{(n)}(-\phi)$ denotes the n^{th} derivative of $g(x+z_0)$ evaluated at $x+z_0 = -\phi$. Note that if $N \to \infty$ we have $h(x) = g(x+z_0)$. The first few coefficients k_n are given by:

$$\begin{aligned} k_0 &= \alpha + \frac{\beta}{2} \\ k_1 &= -2\pi\beta \\ k_3 &= \frac{16}{3}\pi^3\beta \\ k_5 &= -\frac{64}{15}\pi^5\beta \\ k_7 &= \frac{512}{315}\pi^7\beta \\ k_n &= 0, \quad \text{even } n > 0 \end{aligned} \tag{4.23}$$

Thus, finally, we will seek a solution to the coupled differential equations:

$$\ddot{x} + \frac{1}{Q}\dot{x} + (1 + CT_0 + Cu)(x - Du) = 0 \tag{4.24}$$

$$\dot{u} + \frac{1}{\tau}u = -\frac{1}{\tau}T_0 + APh(x) \tag{4.25}$$

We will solve Eqs. 4.24 & 4.25 via the Poincaré-Lindstedt perturbation method. To do this, we must scale $1/Q, Cu$, and Du by a small dimensionless parameter $\epsilon \ll 1$. This will yield solutions for $x(t)$ and $u(t)$ that are power series in ϵ: $x = x_1 + x_2\epsilon + x_3\epsilon^2 + \cdots$ and $u = u_1 + u_2\epsilon + u_3\epsilon^2 + \cdots$. In order to perturbatively solve for the oscillation frequency $\omega = \omega_1 + \omega_2\epsilon + \omega_3\epsilon^2 + \cdots$ we must once more

scale the time dimension by ω. This leads to the coupled system:

$$\omega^2 \ddot{x} + \frac{\epsilon\omega}{Q}\dot{x} + (1 + CT_0 + \epsilon Cu)(x - \epsilon Du) = 0 \tag{4.26}$$

$$\omega\dot{u} + \frac{1}{\tau}u = -\frac{1}{\tau}T_0 + APh(x) \tag{4.27}$$

Setting $\epsilon = 0$ gives us the lowest order of the perturbation:

$$\omega_1^2 \ddot{x}_1 + (1 + CT_0)x_1 = 0 \tag{4.28}$$

$$\omega_1\dot{u}_1 + \frac{1}{\tau}u_1 = -\frac{1}{\tau}T_0 + APh(x_1) \tag{4.29}$$

Choosing $\omega_1^2 = 1+CT_0$ in Eq. 4.28 results in the solution $x_1 = R\cos t$. This solution is now substituted into Eq. 4.29 to solve for u_1. Because $h(x_1)$ is a polynomial in x_1, this leads to:

$$\omega_1\dot{u}_1 + \frac{1}{\tau}u_1 = u_{10} + \sum_{n=1}^{N} u_{1n}\cos nt \tag{4.30}$$

where the coefficients u_{10} and u_{1n} depend on T_0, R, and the details of $h(x_1)$. We will derive these coefficients later in this section, but for now we proceed assuming they are known.

Solving Eq. 4.30, the steady-state solution for u_1 is:

$$u_1(t) = \tau u_{10} + \sum_{n=1}^{N} \frac{\tau u_{1n}}{1 + n^2\omega_1^2\tau^2}(\cos nt + n\omega_1\tau \sin nt) \tag{4.31}$$

Thus the time-averaged value of u (to order ϵ^0 in perturbation theory) increases by an amount τu_{10} during oscillation.

We now proceed to order ϵ^1 of perturbation theory by substituting $x = x_1 + \epsilon x_2$, $u = u_1 + \epsilon u_2$ and $\omega = \omega_1 + \epsilon\omega_2$ into Eq. 4.26 and neglecting terms of order ϵ^2 and higher:

$$\epsilon\omega_1^2\ddot{x}_2 + \epsilon\omega_1^2 x_2 + 2\epsilon\omega_1\omega_2\ddot{x}_1 + \frac{\epsilon\omega_1}{Q}\dot{x}_1 - \epsilon\omega_1^2 Du_1 + \epsilon Cu_1x_1 = 0 \tag{4.32}$$

Rearranging terms, this equation can be written in the more familiar form:

$$\ddot{x}_2 + x_2 = -\frac{2\omega_2}{\omega_1}\ddot{x}_1 - \frac{1}{\omega_1 Q}\dot{x}_1 + Du_1 - \frac{C}{\omega_1^2}u_1 x_1 \tag{4.33}$$

Thus x_2 represents a simple harmonic oscillator with forcing terms given by the right hand side of Eq. 4.33. In order for x_2 not to grow without bound, secular terms must be removed. In other words the forcing terms at frequency $\omega = 1$ must vanish. Thus we proceed by substituting $x_1 = R\cos t$ and Eq. 4.31 for u_1, collecting terms proportional to $\cos t$ and $\sin t$, and equating them to zero. Collecting $\sin t$ terms in Eq. 4.33 leads to

$$\frac{\omega_1^2 D u_{11}}{1 + \omega_1^2\tau^2} - \frac{CRu_{12}}{1 + 4\omega_1^2\tau^2} + \frac{R}{\tau^2 Q} = 0 \tag{4.34}$$

which can be solved for R, bearing in mind that the coefficients u_{11} and u_{12} are dependent on R. Collecting $\cos t$ terms in Eq. 4.33 gives

$$\frac{2\tau\omega_1^2 D u_{11}}{1 + \omega_1^2\tau^2} - \frac{\tau CRu_{12}}{1 + 4\omega_1^2\tau^2} + 4R\omega_1\omega_2 - 2\tau CRu_{10} = 0 \tag{4.35}$$

which can be solved for ω_2 once R is known.

According to Eq. 4.34, the oscillation amplitude R is determined by the coefficients u_{11} and u_{12}, which are the forcing terms for u at frequency ω and 2ω in Eq. 4.30. Moreover, the average temperature change is determined by u_{10}. We will now proceed to calculate these terms based on $h(x)$ in Eq. 4.29.

Deriving u_{10}, u_{11}, and u_{12} is most easily done if we first rewrite $h(x)$ as a series in x rather than $x + z_0 + \phi$. Thus we have

$$h(x) = \sum_{n=0}^{N} \frac{h_0^{(n)}}{n!} x^n \tag{4.36}$$

where $h_0^{(n)}$ is the n^{th} derivative of $h(x)$ evaluated at $x = 0$. Note that this Taylor series terminates at order x^N because $h(x)$ is by definition an N^{th} order polynomial (see Eq. 4.22). If we take $h(x)$ to be 7^{th} order, as is done in Section 4.2, then

the derivatives $h_0^{(n)}$ are related to the factors k_n in Eq. 4.22 by:

$$\begin{aligned}
h_0^{(0)} &= k_0 + k_1 x_0 + k_3 x_0^3 + k_5 x_0^5 + k_7 x_0^7 \\
h_0^{(1)} &= k_1 + 3k_3 x_0^2 + 5k_5 x_0^4 + 7k_7 x_0^6 \\
h_0^{(2)} &= 6k_3 x_0 + 20k_5 x_0^3 + 42k_7 x_0^5 \\
h_0^{(3)} &= 6k_3 + 60k_5 x_0^2 + 210k_7 x_0^4 \\
h_0^{(4)} &= 120k_5 x_0 + 840k_7 x_0^3 \\
h_0^{(5)} &= 120k_5 + 2520k_7 x_0^2 \\
h_0^{(6)} &= 5040k_7 x_0 \\
h_0^{(7)} &= 5040k_7
\end{aligned} \tag{4.37}$$

where we have defined $x_0 = z_0 + \phi$. Equating the right hand sides of Eqs. 4.29 & 4.30 then gives:

$$u_{10} + \sum_{m=1}^{N} u_{1m} \cos mt = -\frac{1}{\tau} T_0 + AP \sum_{n=0}^{N} \frac{h_0^{(n)}}{n!} x_1^n \tag{4.38}$$

In order to calculate u_{10}, u_{11}, and u_{12} we now substitute $x_1 = R\cos t$ and invoke the power formulas for cosines

$$\text{even } n: \qquad \cos^n t = \frac{1}{2^n}\binom{n}{n/2} + \frac{1}{2^{n-1}} \sum_{k=0}^{(n/2)-1} \binom{n}{k} \cos[(n-2k)t] \tag{4.39}$$

$$\text{odd } n: \qquad \cos^n t = \frac{1}{2^{n-1}} \sum_{k=0}^{(n-1)/2} \binom{n}{k} \cos[(n-2k)t] \tag{4.40}$$

where $\binom{a}{b} = a!/(b!(a-b)!)$ is a binomial coefficient. For even n, the constant term arising from $\cos^n t$ is simply $(1/2^n)\binom{n}{n/2}$. Furthermore, because only $\cos^n t$ with even n will lead to $\cos mt$ with even m, the u_{10} term in Eq. 4.38 is

$$\begin{aligned}
u_{10} &= -\frac{1}{\tau} T_0 + AP \sum_{n=0,2,4,\ldots}^{N} \frac{h_0^{(n)}}{n!} \left(\frac{R}{2}\right)^n \frac{n!}{(n/2)!(n/2)!} \\
&= -\frac{1}{\tau} T_0 + AP \sum_{m=0}^{M_0} \frac{h_0^{(2m)}}{(m!)^2} \left(\frac{R}{2}\right)^{2m}
\end{aligned} \tag{4.41}$$

where $M_0 = \text{floor}(N/2)$. The value of u_{11} can similarly be found by substituting Eq. 4.40 into Eq. 4.38 with $n - 2k = 1$. Only odd $n \geq 1$ contribute to this sum. This gives

$$\begin{aligned} u_{11} &= AP \sum_{n=1,3,5,\ldots}^{N} \frac{h_0^{(n)}}{n!} \left(\frac{R^n}{2^{n-1}}\right) \frac{n!}{(\frac{n-1}{2})!(\frac{n+1}{2})!} \\ &= 2AP \sum_{m=0}^{M_1} \frac{h_0^{(2m+1)}}{m!(m+1)!} \left(\frac{R}{2}\right)^{2m+1} \end{aligned} \tag{4.42}$$

where $M_1 = \text{floor}((N-1)/2)$. Lastly, u_{12} is found by substituting $n - 2k = 2$ into Eq. 4.39 and Eq. 4.38. Only even $n \geq 2$ contribute to this sum:

$$\begin{aligned} u_{12} &= AP \sum_{n=2,4,6,\ldots}^{N} \frac{h_0^{(n)}}{n!} \left(\frac{R^n}{2^{n-1}}\right) \frac{n!}{(\frac{n}{2}-1)!(\frac{n}{2}+1)!} \\ &= 2AP \sum_{m=0}^{M_2} \frac{h_0^{(2m+2)}}{m!(m+2)!} \left(\frac{R}{2}\right)^{2m+2} \end{aligned} \tag{4.43}$$

where $M_2 = \text{floor}((N-2)/2)$. Interestingly, if we take $N \to \infty$ these sums bear remarkable resemblance to modified Bessel functions of the first kind:

$$I_\alpha(x) = \sum_{m=0}^{\infty} \frac{1}{m!(m+\alpha)!} \left(\frac{x}{2}\right)^{2m+\alpha} \tag{4.44}$$

Thus for the case of $N \to \infty$ we may write $u_{10} \ldots u_{12}$ as:

$$u_{10} = -\frac{1}{\tau} T_0 + API_0 \left(R\frac{d}{dx}\right) \cdot h(x)\Big|_{x=0} \tag{4.45}$$

$$u_{11} = 2API_1 \left(R\frac{d}{dx}\right) \cdot h(x)\Big|_{x=0} \tag{4.46}$$

$$u_{12} = 2API_2 \left(R\frac{d}{dx}\right) \cdot h(x)\Big|_{x=0} \tag{4.47}$$

In fact, it can be shown that for all $n > 0$ the temperature variation at frequency $n\omega$ is given by:

$$u_{1n} = 2API_n \left(R\frac{d}{dx}\right) \cdot h(x)\Big|_{x=0} \tag{4.48}$$

Of course, in the $N \to \infty$ limit we also have $h(x) = g(x + z_0)$.

If we truncate $h(x)$ at $N = 7$, then we have $M_0 = 3$ in Eq. 4.41. Therefore by Eq. 4.30, the time-averaged change in temperature is given by:

$$\tau u_{10} = -T_0 + \tau AP \sum_{m=0}^{3} \frac{h_0^{(2m)}}{(m!)^2} \left(\frac{R}{2}\right)^{2m} \tag{4.49}$$

Furthermore, when $N = 7$ we have $M_1 = 3$ and $M_2 = 2$ in Eqs. 4.42 & 4.43. Thus u_{11} contains all odd powers of R from R^1 to R^7, and u_{12} contains all even powers from R^2 to R^6. Upon substituting u_{11} and u_{12} into Eq. 4.34, we then finally arrive at our equation for R:

$$0 = c_0 + c_1 R^2 + c_2 R^4 + c_3 R^6 \tag{4.50}$$

where

$$\begin{aligned}
c_0 &= \frac{\omega_1^2 D}{1 + \omega_1^2 \tau^2} h_0^{(1)} + \frac{1}{\tau^2 APQ} \\
c_1 &= \frac{\omega_1^2 D}{1 + \omega_1^2 \tau^2} \frac{h_0^{(3)}}{2^2 1!2!} - \frac{C}{1 + 4\omega_1^2 \tau^2} \frac{h_0^{(2)}}{2^1 0!2!} \\
c_2 &= \frac{\omega_1^2 D}{1 + \omega_1^2 \tau^2} \frac{h_0^{(5)}}{2^4 2!3!} - \frac{C}{1 + 4\omega_1^2 \tau^2} \frac{h_0^{(4)}}{2^3 1!3!} \\
c_3 &= \frac{\omega_1^2 D}{1 + \omega_1^2 \tau^2} \frac{h_0^{(7)}}{2^6 3!4!} - \frac{C}{1 + 4\omega_1^2 \tau^2} \frac{h_0^{(6)}}{2^5 2!4!}
\end{aligned}$$

The results shown above are expressed in dimensionless units. When re-dimensionalized, they reproduce Eq. 4.5 of Section 4.2. The ϵ^1-order correction to the resonant frequency is (upon rearranging Eq. 4.35)

$$\omega_2 = \frac{\tau C}{2\omega_1} u_{10} - \frac{\omega_1 \tau D}{1 + \omega_1^2 \tau^2} \frac{u_{11}}{2R} + \frac{\tau C}{1 + 4\omega_1^2 \tau^2} \frac{u_{12}}{4\omega_1} \tag{4.51}$$

When $h(x)$ is truncated at $N = 7$ this becomes

$$\omega_2 = d_0 + d_1 R^2 + d_2 R^4 + d_3 R^6 \tag{4.52}$$

where (again in dimensionless units)

$$
\begin{aligned}
d_0 &= -\frac{\omega_1 \tau D}{1+\omega_1^2\tau^2}\,\frac{APh_0^{(1)}}{2^1 0!1!} + \frac{\tau C}{2\omega_1}\left(-\frac{1}{\tau}T_0 + APh_0^{(0)}\right) \\
d_1 &= -\frac{\omega_1 \tau D}{1+\omega_1^2\tau^2}\,\frac{APh_0^{(3)}}{2^3 1!2!} + \frac{\tau C}{1+4\omega_1^2\tau^2}\,\frac{APh_0^{(2)}}{2^3 0!2!\omega_1} \\
d_2 &= -\frac{\omega_1 \tau D}{1+\omega_1^2\tau^2}\,\frac{APh_0^{(5)}}{2^5 2!3!} + \frac{\tau C}{1+4\omega_1^2\tau^2}\,\frac{APh_0^{(4)}}{2^5 1!3!\omega_1} \\
d_3 &= -\frac{\omega_1 \tau D}{1+\omega_1^2\tau^2}\,\frac{APh_0^{(7)}}{2^7 3!4!} + \frac{\tau C}{1+4\omega_1^2\tau^2}\,\frac{APh_0^{(6)}}{2^7 2!4!\omega_1}
\end{aligned}
$$

4.4 Static nanowire behavior

From Eqs. 4.13 & 4.14 the static nanowire must satisfy

$$z_0 = DT_0 \tag{4.53}$$

$$\frac{1}{\tau}T_0 = \tau APg(z_0) \tag{4.54}$$

Rearranging these shows that the nanowire equilibrium is determined by the roots of the following equation:

$$0 = APg(z_0) - \frac{z_0}{\tau D} \tag{4.55}$$

Near $P = 0$ this equation has only one root, but as P increases more roots develop. This function is plotted for multiple P values in Fig. 4.5 (a) for $\phi = 0$. The upper panel displays the lowest valid solution of Eq. 4.55, which has a discontinuous jump in z_0 from one crest of $g(z)$ to the next as P increases quasi-statically. These results suggest that for high enough P values, z_0 will reside only in regions of $g(z)$ with negative slope dg/dz – *i.e.* in regions conducive to self-oscillation. It should be noted that in this experiment (and in the function plotted in Fig. 4.5), a positive D value is assumed. In an experiment where $D < 0$, the equilibrium z_0 would shift towards negative values for increasing P, and the tendency of z_0 to reside only in regions conducive to self-oscillation (regions of positive dg/dz in this case) would still be observed.

Fig. 4.5 (b-d) show the expected equilibrium position for our nanowire based on Eq. 4.55 for varying ϕ and P values. Fig. 4.5 (b) displays the equilibrium shift relative to the $P = 0$ position (*i.e.* z_0), which is periodic in $\lambda/2$ as expected. Fig. 4.5 (c) displays the absolute nanowire position within the standing wave (*i.e.* $z_0 + \phi$), and the slope dg/dz at this absolute position is shown in Fig. 4.5 (d). The latter

clearly indicates that above $P \approx 50\,\mu$W the nanowire is most likely to be found in a region with negative dg/dz.

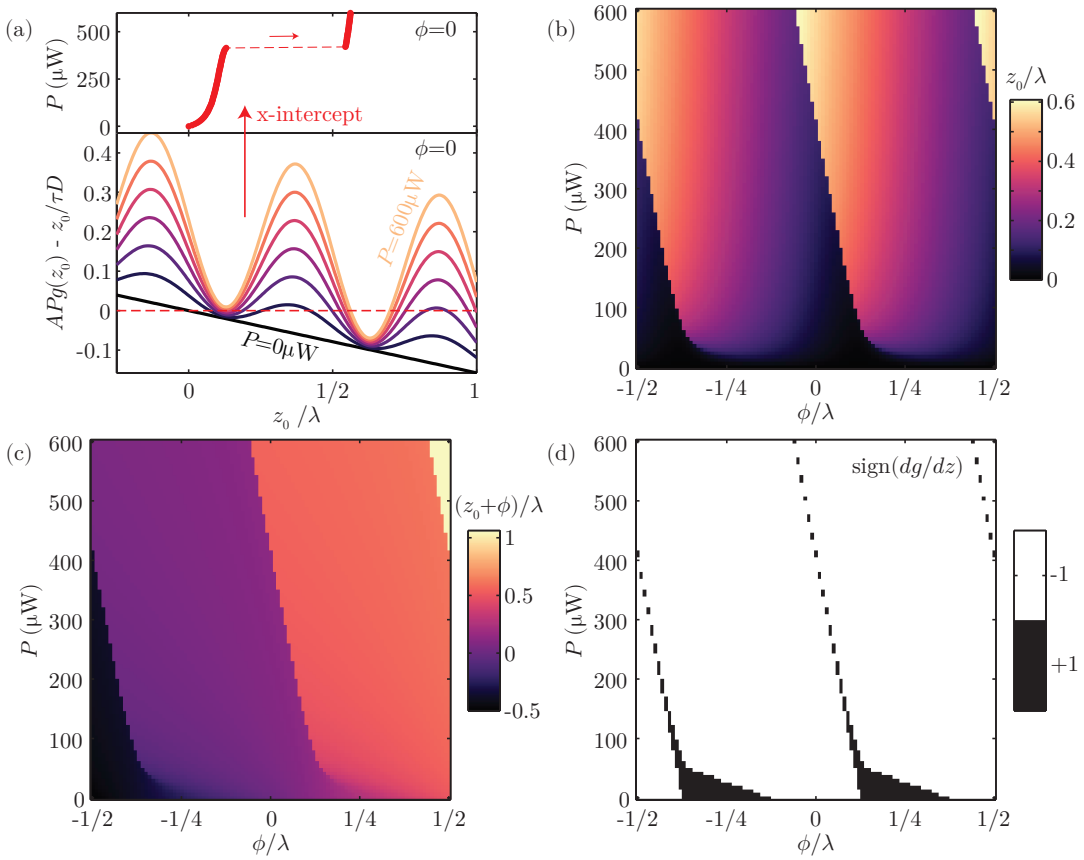

Figure 4.5: Equilibrium position of the static nanowire vs laser power P and initial position ϕ

4.5 Critical power and hysteresis

Reproducing a result from Section 4.3, the amplitude R of self-oscillation is (in dimensionful units):

$$0 = c_0 + c_1 R^2 + c_2 R^4 + c_3 R^6 \tag{4.56}$$

where

$$\begin{aligned}
c_0 &= \frac{\omega_1^2 D}{1+\omega_1^2\tau^2}\, g_{z_0}^{(1)} + \frac{\gamma}{\tau^2 A P} \\
c_1 &= \frac{\omega_1^2 D}{1+\omega_1^2\tau^2}\, \frac{g_{z_0}^{(3)}}{2^2 1!2!} - \frac{\omega_0^2 C}{1+4\omega_1^2\tau^2}\, \frac{g_{z_0}^{(2)}}{2^1 0!2!} \\
c_2 &= \frac{\omega_1^2 D}{1+\omega_1^2\tau^2}\, \frac{g_{z_0}^{(5)}}{2^4 2!3!} - \frac{\omega_0^2 C}{1+4\omega_1^2\tau^2}\, \frac{g_{z_0}^{(4)}}{2^3 1!3!} \\
c_3 &= \frac{\omega_1^2 D}{1+\omega_1^2\tau^2}\, \frac{g_{z_0}^{(7)}}{2^6 3!4!} - \frac{\omega_0^2 C}{1+4\omega_1^2\tau^2}\, \frac{g_{z_0}^{(6)}}{2^5 2!4!}
\end{aligned}$$

Here we have made the approximation $h(x) = g(x + z_0)$. This can be rearranged to express P as a function of R:

$$P = \frac{-\gamma/(\tau^2 A)}{b + c_1 R^2 + c_2 R^4 + c_3 R^6} \tag{4.57}$$

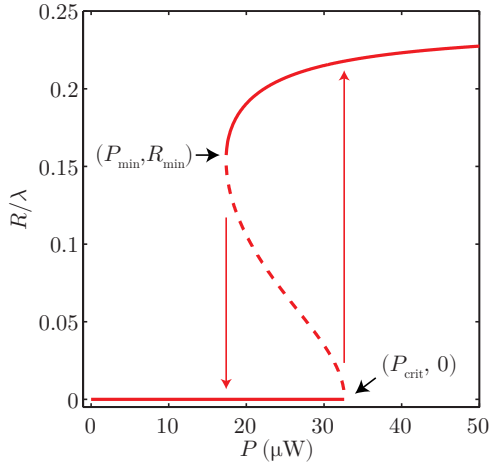

Figure 4.6: A subcritical Hopf bifurcation. A dashed line indicates unstable behavior.

where $b = (\omega_1^2 D g_{z_0}^{(1)})/(1+\omega_1^2\tau^2)$. The critical laser power P_{crit} is simply the $R = 0$ value of this function:

$$P_{\text{crit}} = -\frac{\gamma\left(1+\omega_1^2\tau^2\right)}{\omega_1^2\tau^2 D A g_{z_0}^{(1)}} \tag{4.58}$$

Whether the transition to self-oscillation will be hysteretic or non-hysteretic (*i.e.* whether the Hopf bifurcation will be subcritical or supercritical) is determined by the curvature d^2P/dR^2 at $R = 0$. Upon differentiating Eq. 4.57 twice, one finds that this curvature is given by

$$\left.\frac{d^2P}{dR^2}\right|_{R=0} = \frac{2\gamma c_1}{\tau^2 A b^2} \tag{4.59}$$

Because physical values of γ and A must be positive, this result suggests that $c_1 < 0$ is the necessary condition for a hysteretic transition. Such a transition is depicted in Fig. 4.6. The parameters used to produce this figure are identical to the experimental values of our nanowire, except C has been increased by a factor of 100; ϕ is near $\lambda/8$, where $|g_{z_0}^{(2)}|$ is maximal. In this figure z_0 (the time-averaged position) has been held fixed over the entire P range to simplify the results.

The width of the hysteresis region can be found by analyzing the first derivative of P:

$$\frac{dP}{dR} = \frac{\gamma}{\tau^2 A}\,\frac{2c_1R + 4c_2R^3 + 6c_3R^5}{\left(b + c_1R^2 + c_2R^4 + c_3R^6\right)^2} \tag{4.60}$$

As seen in Fig. 4.6, the minimum P value at which self-oscillation is sustainable coincides with a turning point in $P(R)$ – *i.e.* it occurs when $dP/dR = 0$. Note that $dP/dR = 0$ also occurs at $R = 0$ – *i.e.* at the critical power $P = P_{\text{crit}}$. The lower edge of the self-oscillation region is thus found by solving the following equation for the minimum amplitude R_{min}

$$0 = 2c_1 + 4c_2R^2 + 6c_3R^4 \tag{4.61}$$

and substituting the resulting value back into Eq. 4.57 for P to give $P_{\min} = P(R_{\min})$. This calculation seems straightforward if c_1, c_2, and c_3 are taken as constants, but in actuality these quantities are dependent on z_0, which depends on P; this makes calculation of $P_{\min}$ much more difficult. Therefore one approach to calculating $P_{\min}$ would be to iteratively solve Eqs. 4.61, 4.57 & 4.55 for R, P, and z_0 until they converge on fixed values.

4.6 Estimation of thermal parameters

The mechanical and thermal parameters of our system (ω_0, τ, C, D) can be accurately estimated by knowledge of the material composition of our nanowire and the cantilevers by which it is suspended. The optical parameters (A, α, β) require also knowledge of our laser spot size and the refractive index of the reflective silicon back-plane.

The resonant frequency of a tensioned wire composed of a single material with Young's modulus E and internal strain ε is

$$\omega_0 = \frac{\pi}{L}\sqrt{\frac{E\varepsilon}{\rho}} \tag{4.62}$$

where L is the wire length and ρ is the mass per unit volume. This equation neglects terms due to bending of the wire, and is valid only in the high tension limit. For a wire composed of two distinct materials, this becomes

$$\omega_0 = \frac{\pi}{L}\sqrt{\frac{\sigma_{\text{tot}}}{\mu_{\text{tot}}}} = \frac{\pi}{L}\sqrt{\frac{E_1A_1\varepsilon_1 + E_2A_2\varepsilon_2}{\rho_1A_1 + \rho_2A_2}} \tag{4.63}$$

where $\sigma_{\text{tot}}, \mu_{\text{tot}}$ are the total tensile force and mass per unit length of the wire. The subscripts $1, 2$ have been used to distinguish between the two materials and A_n is the cross-sectional area of either material.

The parameter C, which denotes the fractional frequency change per unit temperature in Eq. 4.13 can be approximated by

$$C = \frac{1}{\sigma_{\text{tot}}}\left(\frac{d\sigma_{\text{tot}}}{dT}\right) \approx -\frac{E_1A_1\alpha_1 + E_2A_2\alpha_2}{E_1A_1\varepsilon_1 + E_2A_2\varepsilon_2} \tag{4.64}$$

Here α_n is the linear thermal expansion coefficient of material n, and this effect is entirely attributed to tension change within the wire. We have assumed here that as the temperature changes both materials are free to expand and do not

influence one another. This is not entirely physical (especially for large T), but we will see that this rough approximation agrees well with the experimentally measured value.

The parameter D describes coupling between temperature and the vertical position of our nanowire. This coupling is caused by the bimetalic cantilevers on either end of the nanowire, which at room temperature ($\approx 300\,\mathrm{K}$) curve upward due to unbalanced stresses between the Nb film (top layer) and the underlying SiN. A detailed calculation of D based on cantilever dimensions is presented in Section 4.7. Here we estimate D for a single nanowire based on angled-SEM (Scanning Electron Microscopy) measurements of the cantilever length l_c and equilibrium angle θ above the horizontal. If θ is known, an estimate for D can be obtained by modeling the cantilever as acting under the influence of an internal torque $\mathcal{T}_c$ which pulls it up and nanowire tension σ_{tot} which pulls it along the horizontal. Relative to a rotation axis at the cantilever clamped edge, the torque exerted by the nanowire is $\sigma_{\mathrm{tot}} l_c \sin\theta$; in equilibrium we must therefore have $\mathcal{T}_c = \sigma_{\mathrm{tot}} l_c \sin\theta$. The vertical position of the cantilever free end is $z = l_c \sin\theta$. If the two cantilevers supporting the nanowire have differing lengths l_{c1}, l_{c2} and equilibrium angles θ_{c1}, θ_{c2}, then the vertical position of the nanowire center is:

$$z = \frac{l_{c1}\sin\theta_{c1} + l_{c2}\sin\theta_{c2}}{2} = \frac{\mathcal{T}_{c1} + \mathcal{T}_{c2}}{2\sigma_{\mathrm{tot}}} \tag{4.65}$$

The change in vertical position of the nanowire per unit temperature change is then

$$D \approx -\left(\frac{\mathcal{T}_{c1} + \mathcal{T}_{c2}}{2\sigma_{\mathrm{tot}}^2}\right)\left(\frac{d\sigma_{\mathrm{tot}}}{dT}\right) \approx \left(\frac{\mathcal{T}_{c1} + \mathcal{T}_{c2}}{2}\right)\frac{E_1 A_1 \alpha_1 + E_2 A_2 \alpha_2}{(E_1 A_1 \varepsilon_1 + E_2 A_2 \varepsilon_2)^2} \tag{4.66}$$

This formula holds only for small deviations away from the equilibrium angles θ_{c1}, θ_{c2}. As with C, this parameter is proportional to the change in total wire tension per unit temperature.

For a heated mechanical resonator composed of a single material, the thermal time constant τ would simply be:

$$\tau = \frac{L_{\text{eff}}}{\Lambda A_{\text{eff}}} \rho c V_{\text{eff}} \tag{4.67}$$

where Λ, c are the thermal conductivity and specific heat of the material, and $L_{\text{eff}}, A_{\text{eff}}$ are the effective length and cross section of the conductive channel. V_{eff} is the effective volume of heated material, and the combination $\rho c V_{\text{eff}}$ is the thermal mass. The combination $L_{\text{eff}}/(\Lambda A_{\text{eff}})$ is the thermal resistance.

In our system, heat flows from the nanowire midpoint (where the laser is focused) out to the clamped edges of the two cantilevers. It flows in parallel paths through the SiN (material 1) and Nb (material 2), along two possible directions out from the midpoint. The thermal resistance of the nanowire (from midpoint to endpoint) is $R_w = (1/2)L/(\Lambda_1 A_1 + \Lambda_2 A_2)$. The resistance of either cantilever is $R_c = l_c/(\Lambda_1 A_{c1} + \Lambda_2 A_{c2})$. Because of the two directions outward from the midpoint, the total resistance is $R_{\text{tot}} = (R_w + R_c)/2$. The total thermal mass μ of the system (assuming cantilevers of equal length l) is given by $\mu_{\text{tot}} = c_1\rho_1(LA_1 + 2l_cA_{c1}) + c_2\rho_2(LA_2 + 2l_cA_{c2})$. Therefore the thermal time is

$$\tau = \mu_{\text{tot}} R_{\text{tot}} \tag{4.68}$$

The A parameter in Eq. 4.14 can be expressed as:

$$A = \frac{a}{\mu_{\text{tot}}} = \frac{[1 - \exp(-4\pi k_{Nb} t_{Nb}/\lambda)]\,\text{erf}\left(\sqrt{2}\, w/d_L\right)}{\mu_{\text{tot}}} \tag{4.69}$$

Here, a denotes the fraction of local laser light absorbed by the nanowire; k_{Nb}, t_{Nb} are the extinction coefficient and thickness of the Nb film, and w is the width of the nanowire. The diameter of our Gaussian laser beam is denoted by d_L, and the error function erf($\sqrt{2}w/d_L$) represents the fraction of laser beam cross-sectional area that is covered by the thin nanowire (assuming it lies along the

center of the laser beam). The terms in square brackets denote the fraction of light within that thin area that is absorbed by the Nb film.

The nanowire sits in an optical standing wave generated by interference between incident light from our laser and light reflected from the silicon backplane. If we approximate the light as plane waves, it can be shown that in the presence of such a reflector the optical intensity varies with distance as

$$P(z) = P_0(1 - \sqrt{R_0})^2 + 4P_0\sqrt{R_0}\sin^2\frac{2\pi z}{\lambda} \tag{4.70}$$

where P_0 corresponds to the incident laser power and R_0 is the reflection coefficient. Note that $P(z)$ here denotes the total energy density $P(z) = |\vec{E}(z)|^2$ of the light in plane z, where $\vec{E}$ is the combined electric field of the incident and reflected beams. Similarly, $P_0 = |\vec{E}_0|^2$ for the incident beam.

This is related to the index of refraction of the silicon, $n_{Si} = 3.83$ at 660 nm, by

$$R_0 = \left|\frac{n_{Si} - 1}{n_{Si} + 1}\right|^2 \tag{4.71}$$

Thus the two remaining parameters in Eq. 4.14 are given by

$$\alpha = (1 - \sqrt{R_0})^2 \tag{4.72}$$

$$\beta = 4\sqrt{R_0} \tag{4.73}$$

Because the nanowire is much thinner than both the wavelength λ and spot size R_L, we have assumed that it does not greatly affect the optical standing wave in Eq. 4.70.

Table 4.1 lists the relevant material properties for SiN and Nb. Tables 4.2 & 4.3 list the resulting mechanical and thermal parameters of our system. In Table 4.2, all values have been measured experimentally except for those marked

with asterisks (*), which were calculated based on Eq. 4.63. In Table 4.3, A excludes the error function shown in Eq. 4.69 since d_L (the laser spot diameter) was used as a fit parameter during the experiment. The other fit parameters were $1/\tau$ (the cooling rate) and ϕ, the initial position of the nanowire within the optical field, as seen in Eq. 4.15. Typical d_L values arising from the fits were 2μm to 2.5μm.

	SiN	Nb	Units	Description
ρ	3000	8600	$\mathrm{kg\,m^{-3}}$	mass density
Y	290	105	GPa	Young's modulus
α	3	7	$10^{-6}\,\mathrm{K^{-1}}$	thermal expansion coeff.
Λ	22	54	$\mathrm{Wm^{-1}K^{-1}}$	thermal conductivity
c	700	265	$\mathrm{Jkg^{-1}K^{-1}}$	specific heat
k	0	3.36		extinction coefficient

Table 4.1: Material parameters used for SiN & Nb

	Value	Units	Description
$\omega_0/2\pi$	3.03	MHz	frequency
A_1	875	$\mathrm{nm^2}$	wire SiN cross-section
A_2	1420	$\mathrm{nm^2}$	wire Nb cross-section
$\varepsilon_{\mathrm{SiN}}$	0.3	%	*strain
$\varepsilon_{\mathrm{Nb}}$	0.02	%	*strain
t_{Nb}	20	nm	Nb thickness
w	51	nm	wire width
L	40	μm	wire length
l_{c1}	2.4	μm	cantilever length
l_{c2}	4.1	μm	cantilever length
θ_1	16°		cantilever angle
θ_2	11°		cantilever angle
A_{c1}	1.41	$10^{-13}\,\mathrm{m^2}$	cantilever SiN cross-section
A_{c2}	1.13	$10^{-13}\,\mathrm{m^2}$	cantilever Nb cross-section

Table 4.2: Mechanical parameters of our nanowire

	Theoretical Value	Value From Fit	Units
A	1.87	–	$10^{11}\,\mathrm{K\,J^{-1}}$
$1/\tau$	2.49	7.46	kHz
C	-2.21	–	$10^{-3}\,\mathrm{K^{-1}}$
D	1.64	–	$\mathrm{nm\,K^{-1}}$
α	0.171	–	
β	2.344	–	

Table 4.3: Photo-thermal parameters of our nanowire

4.7 Beam theory for supporting cantilevers

The supporting cantilevers at either end of our nanowire are composed of a layer of stressed SiN coated with a thin film (20 nm) of Nb. The Nb was deposited by sputter deposition. In this section we assume that the unbalanced stresses which cause the cantilevers to curl upward are entirely thermally induced – *i.e.* arising due to differing thermal expansion coefficients in the two layers and deposition of Nb atoms at a temperature $\gg 300\,\mathrm{K}$. Internal stresses in the sputtered film can also contribute to the overall stress, but will not affect the scaling of our coupling constant D with cantilever dimensions.

We begin by calculating the neutral axis of a two-material composite beam. It is located a distance $\bar{y}$ above the bottom surface of the lower material (material 2). During bending, the stresses above and below the neutral axis must balance to zero. For two homogeneous materials (moduli E_1, E_2) of equal width and uniform thicknesses h_1, h_2, this condition simplifies to $0 = E_1 h_1 y_1 + E_2 h_2 y_2$. Here $y_1 = h_2 + h_1/2 - \bar{y}$ and $y_2 = h_2/2 - \bar{y}$ are the distances from the centers of materials

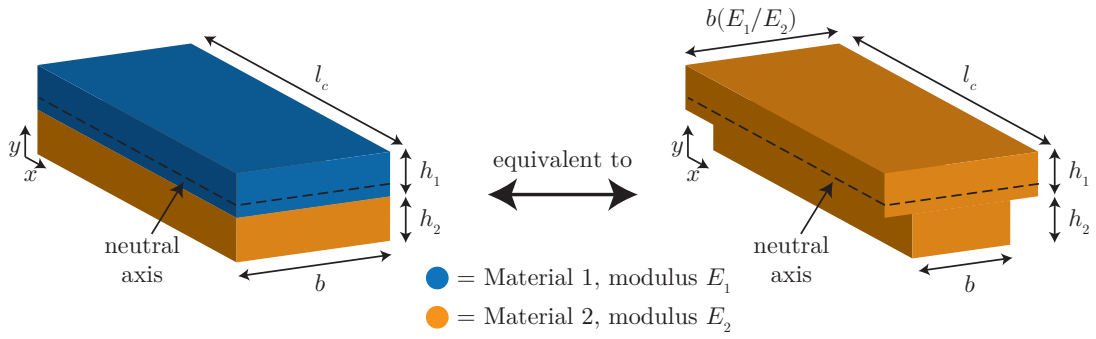

Figure 4.7: Equivalent views of the composite cantilever according to beam theory

1 and 2 to the neutral axis. The neutral axis is therefore located at:

$$\bar{y} = \frac{\left(h_2 + \frac{h_1}{2}\right)\frac{E_1}{E_2}h_1 + \frac{1}{2}h_2^2}{\frac{E_1}{E_2}h_1 + h_2} \tag{4.74}$$

This is depicted in Fig. 4.7. A simplification we can make in analyzing the composite beam is to use an equivalent area to represent the increased stiffness of material 1 (the Nb). This is also depicted in Fig. 4.7. Both materials are now assumed to have modulus E_2, but the top material has an effective width bE_1/E_2 compared to the original b. The area moment of inertia of the beam relative to this axis is:

$$I = \bar{I}_1 + \bar{A}_1 y_1^2 + \bar{I}_2 + \bar{A}_2 y_2^2 \tag{4.75}$$

where

$$\bar{I}_1 = \frac{E_1}{E_2}\frac{bh_1^3}{12} \qquad \bar{I}_2 = \frac{bh_2^3}{12}$$
$$\bar{A}_1 = \frac{E_1}{E_2}bh_1 \qquad \bar{A}_2 = bh_2$$

Above $\bar{I}_1, \bar{I}_2$ are the moments of inertial relative to the center axes of the two materials, and the parallel axis theorem has been applied. Because we have used E_2 as the reference modulus, the bending stiffness of the composite beam is

$$K = E_2 I. \tag{4.76}$$

In the absence of tensile force from the nanowire, either cantilever should have constant curvature κ due to its internal/thermal stresses. Approximating this curvature by $\kappa = d^2z/dx^2$, where $z(x)$ is the vertical position of the cantilever a distance x from its clamping point, leads to a deflection profile of $z(x) = (1/2)\kappa x^2$. Therefore the height of the cantilever end is $z_{\max} = (1/2)\kappa l_c^2$, where l_c is the cantilever length. If the curvature is entirely thermally-induced, it is given by:

$$\kappa = \frac{6E_1E_2(h_1+h_2)h_1h_2(\alpha_1-\alpha_2)\Delta T}{E_1^2h_1^4 + 4E_1E_2h_1^3h_2 + 6E_1E_2h_1^2h_2^2 + 4E_1E_2h_1h_2^3 + E_2^2h_2^4} \tag{4.77}$$

where α_1, α_2 are the thermal expansion coefficients of the two materials and ΔT is the temperature change relative to a reference temperature (the Nb deposition temperature). Other internal stresses in the two materials may contribute to κ, however, so the remaining equations will be presented for a general κ.

Shown in Fig. 4.8 is the effect of nanowire tension σ on the composite beam. Here we approximate the curved cantilever as a straight beam at angle θ. This allows straightforward calculation of the cantilever deflection δ due to loading by the nanowire tension. The angle θ is given by $\tan\theta = z_{\max}/l_c = \kappa l_c/2$, and the nanowire tension applies a load perpendicular to the beam of $\sigma \sin\theta$. The deflection of the composite beam is therefore

$$\delta = \frac{l_c^3 \sigma \sin\theta}{3K} \tag{4.78}$$

The deflection of the cantilever end in the vertical direction is given by $\delta\cos\theta$. Thus we arrive finally at the change in vertical position per unit temperature change (*i.e.* stress change) of the nanowire:

$$D = \frac{d(\delta\cos\theta)}{dT} = \frac{l_c^3 \sin\theta\cos\theta}{3K}\frac{d\sigma}{dT} \tag{4.79}$$

Because the bending stiffness (given by Eq. 4.76) $K \propto b$, where b is the cantilever width, this derivation reveals that the photothermal coupling $D \propto l_c^3/b$. This suggests that D can be drastically enhanced simply by using longer cantilevers. Moreover, the optimal cantilever angle is $\theta = 45°$.

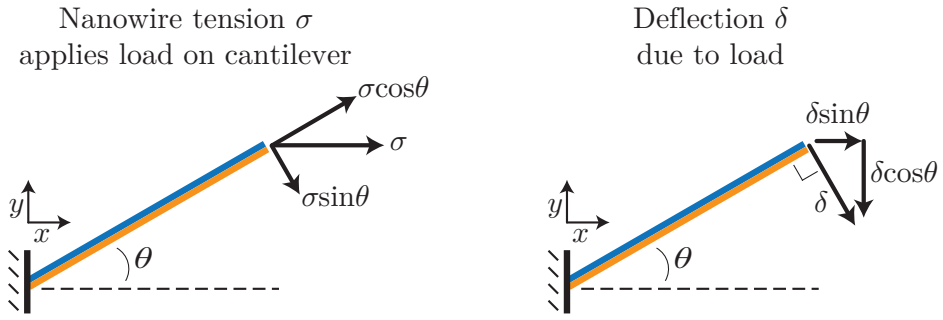

Figure 4.8: Behavior of the composite beam under load

4.8 Nonlinearity of the optical readout technique

The motion of our nanowire is detected by measuring the intensity of laser light reflected from the sample. This reflection comes from the underlying Si backplane, and is modulated by the absorption of our nanowire. We assume that the nanowire is sufficiently thin compared to the laser wavelength ($\lambda = 660\,\text{nm}$) and spot size (Gaussian beam diameter $d_L \approx 2\,\mu\text{m}$) that it does not cause significant reflections itself or trap any light between the nanowire and mirror as in an optical cavity. Indeed, the $\sim 50\,\text{nm}$-wide nanowire acts as a single slit causing any reflected laser light to diffract away from the optical axis quite rapidly.

The power measured by our high-speed photo-detector can be approximated by $P - P_{\text{abs}}(z)$, where P is the incident laser power and $P_{\text{abs}}(z)$ is the position-dependent power absorbed by our nanowire. As shown in Eq. 4.69, the absorbed power is

$$P_{\text{abs}}(z) = aPg(z) \tag{4.80}$$

where a describes the absorptive properties of the Nb film on our nanowire. The dimensionless optical intensity profile $g(z)$ (reproduced form Eq. 4.15) is:

$$g(z) = \alpha + \beta \sin^2\left(\frac{2\pi(z+\phi)}{\lambda} - \frac{\pi}{4}\right) \tag{4.81}$$

where α, β are constants, ϕ is the nanowire's initial location within the optical field. The voltage generated by our photo-detector is therefore

$$V(t) = bGP[1 - ag(z(t))] \tag{4.82}$$

where b denotes any optical losses between the nanowire and the photo-detector (*e.g.* reflections at air-lens interfaces), and G is the photo-detector gain.

The nonlinear relationship between $z(t)$ and $V(t)$ generates harmonics of the

nanowire oscillation frequency ω in the detected voltage. The strength of these harmonics can be calculated in an analogous fashion to the terms $(u_{11}, u_{12}, \cdots)$ in Section 4.3. To do this, the nanowire motion is again modeled by $z = x + z_0$, where $x = R\cos\omega t$ describes the oscillation (with amplitude R and frequency ω) and z_0 is the equilibrium position.

If the optical field $g(x + z_0)$ is approximated by an N^{th} order polynomial (see Eq. 4.22) $h(x) \approx g(x + z_0)$, then the voltage detected at frequency $i\omega$ (where i is a positive integer) has amplitude

$$V_{i\omega} = -2abGP \sum_{m=0}^{M_i} \frac{h_0^{(2m+i)}}{m!(m+i)!} \left(\frac{R}{2}\right)^{2m+i} \tag{4.83}$$

Here $h_0^{(n)}$ is the n^{th} derivative of $h(x)$ evaluated at $x = 0$ or, equivalently, the n^{th} derivative of $g(z)$ evaluated at $z = z_0$. The summation above terminates at $M_i = \text{floor}((N-i)/2)$, where N is again the polynomial order or $h(x)$. See Eqs. 4.38 - 4.43 for details on the derivation.

If we take $N = 7$, the first three harmonics are given by:

$$V_{1\omega} = -2abGP \left[\frac{h_0^{(1)}}{0!1!} \left(\frac{R}{2}\right) + \frac{h_0^{(3)}}{1!2!} \left(\frac{R}{2}\right)^3 + \frac{h_0^{(5)}}{2!3!} \left(\frac{R}{2}\right)^5 + \frac{h_0^{(7)}}{3!4!} \left(\frac{R}{2}\right)^7 \right] \tag{4.84}$$

$$V_{2\omega} = -2abGP \left[\frac{h_0^{(2)}}{0!2!} \left(\frac{R}{2}\right)^2 + \frac{h_0^{(4)}}{1!3!} \left(\frac{R}{2}\right)^4 + \frac{h_0^{(6)}}{2!4!} \left(\frac{R}{2}\right)^6 \right] \tag{4.85}$$

$$V_{3\omega} = -2abGP \left[\frac{h_0^{(3)}}{0!3!} \left(\frac{R}{2}\right)^3 + \frac{h_0^{(5)}}{1!4!} \left(\frac{R}{2}\right)^5 + \frac{h_0^{(7)}}{2!5!} \left(\frac{R}{2}\right)^7 \right] \tag{4.86}$$

The derivatives $h_0^{(n)}$ are listed in Eq. 4.37. Note that the odd harmonics of V only contain odd derivatives of $h(x)$ while the even harmonics only contain even derivatives. This suggests that odd harmonics of V vanish when z_0 is located at an extremum in $g(x + z_0)$, while even harmonics vanish when z_0 is at an inflection point in $g(x + z_0)$. Also note that for low laser powers, when the nanowire is not undergoing self-oscillation, small-amplitude motion $R \ll \lambda$ results in the

linear relationship $V_{1\omega} \approx -abGPh_0^{(1)}R$ and $V_{2\omega} \approx V_{3\omega} \approx 0$. This linear relation between the vibration amplitude R and detected voltage $V_{1\omega}$ allows us to measure Lorentzian lineshapes upon driving nanowire motion inertially, as is shown in Fig. 4.1 (c) of Section 4.2.

Chapter 5

Temperature-dependence of graphene stress and elasticity

5.1 Introduction

As discussed in earlier chapters, atomically thin graphene membranes have considerable promise as mechanical resonators for force and mass sensing, optomechanical elements [12], studies of quantum motion [13, 14], and electronic components as signal filters, frequency mixers, and oscillators [10, 11, 44]. Moreover, suspended graphene with intentionally etched nano-pores has been proposed as a mechanical filter for gas sensors, fuel cells [126], and low-cost DNA sequencers [127]. In all of these applications, graphene performance is strongly tied to its mechanical and thermal properties. Non-idealities such as membrane wrinkles or surface contaminants, which have been widely reported in fabri-

cated graphene devices [33, 91], can drastically degrade device performance.

Despite theoretical work and numerical simulations predicting that suspended graphene should expand as its temperature is lowered (*i.e.* it has a negative thermal expansion coefficient, or TEC) [128, 129], experimental MEMS graphene devices have consistently shown increasing resonant frequencies (*i.e.* increased tension) as they are cooled below 300 K [10, 30, 71]. In some cases this apparent discrepancy in the sign of the TEC has been attributed to a large positive TEC of metal at the membrane boundary [10, 71], but not all devices have such metal at the boundary. In most devices studied by our group – all of which have historically demonstrated positive TECs at and below 300 K – the graphene is supported on all sides by SiO_2 on Si, both of which have smaller TECs (in magnitude) than that expected theoretically for graphene.

Complicating matters further, graphene MEMS devices are generally expected to have a $1 - 2$ nm layer of polymer contamination on their surface. The polymer in question is usually poly(methyl methacrylate), more commonly known as PMMA. For graphene grown by chemical vapor deposition, coating with a layer of ~ 200 nm PMMA is part of a standard process used to remove the graphene from its growth substrate [130, 131]. Graphene that has been exfoliated from bulk graphite is equally susceptible to contamination, since PMMA is typically used as a lithography resist in patterning metal electrodes on top of the exfoliated graphene [10]. While the vast majority of PMMA is easily removed by dissolving in acetone or another solvent, a small portion typically persists on the graphene surface. Even after high-temperature annealing in an H_2/Ar environment (a process specifically designed to remove PMMA from graphene), an almost full surface coverage of PMMA has been shown to per-

sist [33]. For graphene MEMS devices, attempts to measure the membrane mass usually produce a value that is 5 – 10 times larger than expected for clean monolayer graphene [10, 12, 71].

In this chapter we study the temperature dependence of the tension and elastic modulus of two suspended graphene membranes. Our results show that both of these parameters are strongly temperature-dependent from 300 K to 80 K. We also observe the resonant frequencies of these membranes as they are heated from 300 K to 500 K, revealing that a resonant frequency (and therefore tension) minimum exists near room temperature. This suggests that the TEC is positive for temperatures below roughly 315 K, and negative for higher temperatures. Lastly, we observe a large, reproducible hysteresis in the measured resonant frequency as our graphene devices are cycled between 300 K and 550 K. After returning to 300 K, the measured frequency evolves exponentially in time with a time constant of $\sim$ 24 hours. Our results clash with expectations for clean, ideal graphene membranes, but are consistent with expectations for composite membranes composed of graphene coated by a thin layer of polymer residue.

These results have not yet been published.

5.2 Experimental results

In order to measure the elastic properties of graphene, we have suspended it over circular trenches in a Si/SiO_2 substrate, as shown in Figure 5.1. This device geometry is functionally similar to graphene structures used in previous studies [12, 44]. Each device features three metallic electrodes (consisting of 5 nm Ti + 25 nm Pt) which serve as Source, Drain, and Gate; the Source and Drain electrodes contact the graphene from underneath, while the Gate electrode is located at a distance $d = 1.3\,\mu$m below the graphene at the base of the circular trench. A voltage differential $V_{dc} + v_{ac}$ is applied between the Drain and Gate electrodes (as depicted in Fig. 5.1) in order to induce static deformation and to excite resonant motion. The electrostatic force experienced by the graphene is $F_{\text{tot}} = -(1/2)(dC/dz)(V_{dc} + v_{ac})^2$, where dC/dz is the change in capacitance of the graphene-Gate system per unit vertical displacement of the graphene. Assuming $V_{dc} \gg v_{ac}$, the DC and AC forces on the membrane are $F_{dc} = -(1/2)(dC/dz)V_{dc}^2$ and $F_{ac} = -(dC/dz)V_{dc}v_{ac}$.

We focus primarily on two graphene devices throughout this chapter: Device 1, with radius $R = 2.9\,\mu$m, and Device 2, with $R = 2.3\,\mu$m. A Scanning Electron Microscopy (SEM) image of Device 1 is shown in Fig. 5.1 (b). Graphene for these devices was grown on Cu foil via chemical vapor deposition (CVD), and transferred to the pre-patterned substrate via standard processes [32]. Namely, the as-grown graphene was coated with 150 nm of PMMA, followed by wet etching of the Cu foil, cleaning of the graphene in deionized water, and wet transfer onto the pre-fabricated device substrate. The graphene (with PMMA film still present) was then coated with photoresist and patterned to the $\sim 25\,\mu$m circular region shown using optical lithography and plasma etching. Finally, the PMMA

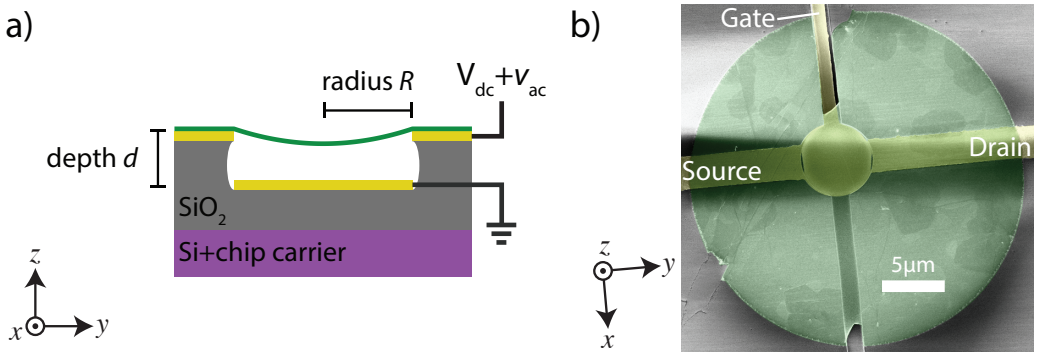

Figure 5.1: **The devices under test.** (a) Cartoon diagram of a graphene device viewed in cross-section. The suspended graphene (green) is pulled downward toward the metallic back-gate via an applied voltage differential $V_{dc} + v_{ac}$; this stretches the graphene membrane, altering its tension and hence resonant frequency. (b) False-color SEM image of Device 1, showing the partially-suspended graphene (green), metallic Source, Drain, and Gate electrodes (yellow), and the surrounding SiO_2 substrate (grey).

and photoresist layers were removed by soaking in Microposit Remover 1165 (1-methyl-2-pyrrolidine) at 80°C, followed by critical point drying in isopropyl alcohol to gently remove the devices from solution. Devices 1 & 2 originate from the same CVD graphene growth, and are located on the same substrate (a roughly 1 cm^2 Si chip).

The presence of both Source and Drain electrodes allows current to flow through the graphene, which can be useful for current-annealing [132] to remove surface contaminants (*e.g.* PMMA residue) or for utilizing the graphene transconductance – *i.e.* the change in conductance G per unit displacement relative to the Gate electrode dG/dz – to detect membrane motion [133]. However, neither of these was employed in this work. Current annealing acts primarily through ohmic heating, and was rejected here in favor of controlled heating of our devices in a custom-built high-temperature sample stage. Furthermore, membrane motion was detected using an all-optical method. This method is

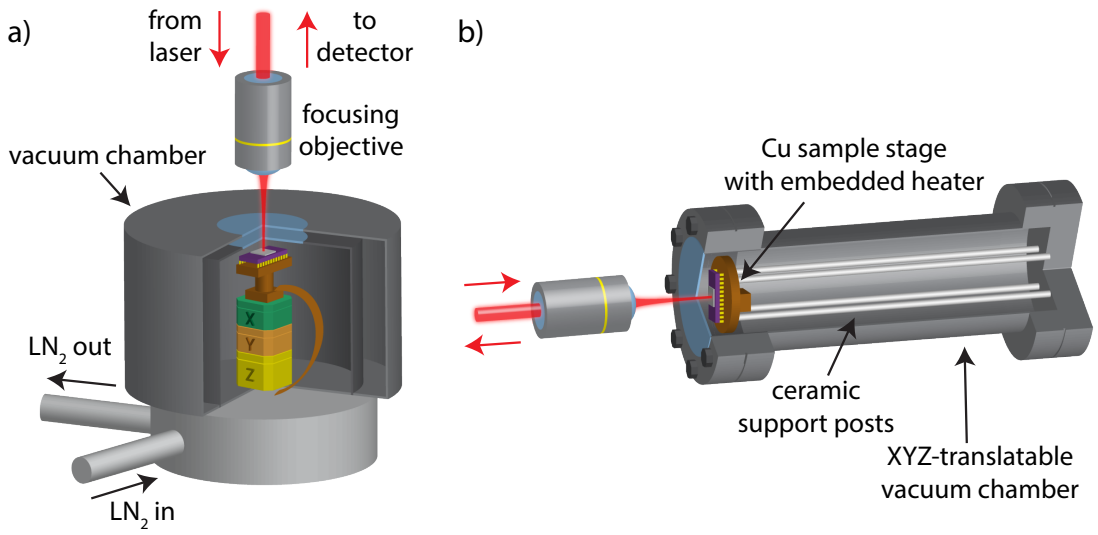

Figure 5.2: **Experimental test chambers.** (a) Liquid N_2 flow cryostat with optical access. Visible are the vacuum chamber and concentric inner radiation shield. The sample is mounted on a 24-pin Dual In-line Package (DIP, purple). (b) The high-temperature test chamber with optical window. The DIP is seen here mounted on a Cu sample stage.

more sensitive than the transconductance measurement and does not suffer from the large "background" capacitive signal which often dominates the desired electrical signal. Optical detection has been described in previous works, and is akin to optical interferometry [12, 44]. A focused laser beam is incident on the device, and reflected light is collected by a high-speed photo-detector. Because of the graphene's 2.3% optical absorption, it encodes its displacement relative to the Gate (which acts as a mirror) in the intensity of the reflected laser beam.

Diagrams of our experimental setup are shown in Figure 5.2. Two separate test chambers are used to study the low-temperature (80-300 K) and high-temperature (300-550 K) behavior of our graphene membranes. For low-

temperature measurements (Fig. 5.2 (a)), an open-loop flow cryostat is employed. The graphene sample is located inside a vacuum chamber with optical access, and is mounted on piezo-electric translation stages in order to focus the detection laser directly on the desired device. The sample is thermally-linked directly to the "cold finger" at the base of the cryostat via braided Cu wire. For high-temperature measurements (Fig. 5.2 (b)), the sample is mounted on a Cu stage which has an embedded resistive heater and is thermally isolated from the remainder of the test chamber by ceramic support posts. In both test chambers, the ambient pressure is maintained below 10^{-6} Torr by an external ion pump.

At a given temperature, we can measure the elastic properties of a graphene membrane by measuring its resonant frequency as a function of the applied electrostatic force F_{dc}. The applied force pulls the graphene towards the Gate, stretching it and thereby increasing its tension by an amount commensurate with its Young's modulus and the induced strain. The resonant frequency of a circular membrane is given by $\omega_0 = (\alpha/R)\sqrt{\sigma/\rho}$, where α is a dimensionless constant and R, σ, ρ are the membrane radius, tension, and mass per unit area, respectively. The tension is a combination of intrinsic tension σ_0 and electrostatically-induced tension $\Delta\sigma = (1/2)Eh(\Delta A/A)$, where $\Delta A/A$ is the fractional change in surface area due to deflection, h is the membrane thickness, and $E = Y/(1-\nu^2)$ is the in-plane modulus. Here, Y, ν are the membrane Young's modulus and Poisson ratio. We will henceforth refer to the combination Eh as the 2-Dimensional (2D) modulus. For pristine graphene, the material parameters are $\rho = 0.75\,\mathrm{kg/m^2}$ and $Eh = 340\,\mathrm{N/m}$ [27]. These values cannot be assumed for our devices because of non-idealities such as surface contaminants and multi-grain CVD graphene.

If the applied voltage V_{dc} is varied over a large enough range, the three parameters ρ, σ_0, Eh can be extracted from a polynomial fit of the type $\omega_0^2 = a + bV_{dc}^2 + cV_{dc}^4$. Expressed in terms of physical parameters, this is

$$\omega_0^2 = \left(\frac{\alpha}{R}\right)^2 \frac{\sigma_0}{\rho} - \frac{\epsilon_0 V_{dc}^2}{d^3\rho} + \frac{\beta E h \epsilon_0^2 V_{dc}^4}{d^4 \rho \sigma_0^2} \tag{5.1}$$

where β is a dimensionless constant and ϵ_0 is the permittivity of free space. The V_{dc}^0 and V_{dc}^4-order terms in this expression describe a tensioned membrane under electrostatic load as discussed above, and the V_{dc}^2-order term represents a nonlinear dynamics effect known as capacitive softening. This is caused by modulation of the graphene-Gate capacitance (and hence the applied force F_{dc}) as the membrane vibrates. The gradient of this force dF_{dc}/dz acts as a negative spring constant, reducing the resonant frequency. This effect is common in capacitively-driven MEMS/NEMS structures. Although all membrane modes will in theory obey Eq. 5.1, we focus solely on the fundamental mode, where $\alpha \approx 2.4048$ and $\beta \approx 0.1316$. A derivation of Eq. 5.1 is provided in Section 5.4.

Shown in Figure 5.2 (a) is a sample data set for Device 2 measured at 300 K. Here the vibration amplitude (in units of μV produced by the photo-detector) is measured as a function of drive frequency and V_{dc}, where V_{dc} is the slow scan axis. We note that in order to obtain an adequate signal to noise ratio, the membrane is in some cases driven into the nonlinear "Duffing" regime. That is, the amplitude of motion is sufficiently large that the measured linescans are strongly asymmetric (Figs. 5.2 (c,d)); this is consistent with motion-induced membrane stiffening, as it always displays spring hardening (*i.e.* a right-leaning peak). From these nonlinear linescans, a fit to the phase and amplitude (black lines) allows us to extract the true resonant frequency, which does not coincide with the peak amplitude. In this way, the resonant frequency ω_0 is measured at each voltage V_{dc} and fit to a model similar to Equation 5.1, as shown in Fig-

ure 5.2 (d); the full fitting model used incorporates more nonlinear terms (producing better results at high V_{dc}), while maintaining only three free-parameters ρ, σ_0, and Eh. See Section 5.4 for more information. In fitting the resonant frequencies, positive and negative V_{dc} data are fitted separately to allow for slight temperature variations over the slow V_{dc} scan, and fit parameters are then combined in an inverse-variance weighted average. Uncertainties in the resulting parameters ρ, σ_0, Eh reflect 68% confidence intervals based on the residuals of the fits.

Low-temperature data for Devices 1 & 2 is shown in Figures 5.4 & 5.5. In both, the sample temperature T is lowered from 300 K to 80 K in 20 K increments and then returned to 300 K at the same rate. As can be seen in both data sets, the ω_0 versus V_{dc} curves shift upward in frequency and flatten considerably as the temperature is decreased below 300 K. Because of the flattening of this data, the 3-parameter fit for ρ, σ_0, Eh described above becomes increasingly unreliable at low temperatures. To counteract this, the 3-parameter fit was performed only initially at $T = 300$ K, and the resulting mass density ρ was used in a 2-parameter fit at all lower temperatures. The assumption that ρ remains constant over the entire temperature range is justified because: 1) A constant vacuum is maintained throughout the experiment, so any adsorption or desorption of gases from the membrane surface is minimal. 2) The membrane is far from the coldest component of the cryostat, meaning that any potential cryopump effect which would lead to increased gas adsorption is also negligible. Because our fitted value of ρ has some associated uncertainty, a Monte-Carlo approach was used in the 2-parameter fits (each fit was performed 500 times using random, normally distributed ρ values) to properly estimate our error bars for σ_0 and Eh.

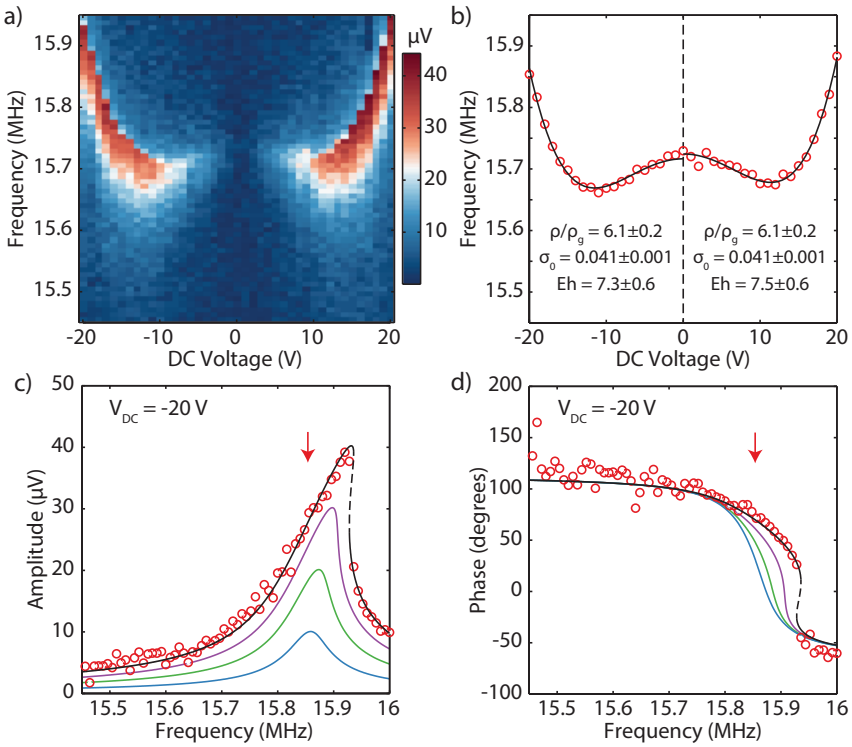

Figure 5.3: **A sample V_{dc} scan of Device 2, measured at 300K.** (a) Amplitude of graphene motion vs drive frequency and V_{dc}. (b) The extracted resonant frequencies from (a) (circles), and fit to the model described in the text (black lines). (c,d) A single linescan from (a) taken at $V_{dc} = -20$ V (circles), plotted as amplitude and phase. Red arrows indicate the location of the resonant frequency, as determined from a Duffing model fit to the data (black line). Colored lines are theoretical linescans using the same Duffing constant but weaker drive forces. Dashed portions of the fit indicate multivalued regions.

The measured mass of each device at $T = 300\,\mathrm{K}$ is (in units of graphene monolayers): $\rho = 7.2 \pm 0.5$ for Device 1 and $\rho = 6.1 \pm 0.2$ for Device 2. Using these masses, the fits to the low-temperature data produce the values of σ_0 and Eh shown in Figs. 5.4 (b) & 5.5 (b). Both devices show a clear and monotonic increase in σ_0 and Eh as the temperature decreases. We note that this increase in σ_0 is counter to expectations for ideal graphene, as its negative thermal expansion coefficient (TEC) of $\alpha_g \approx -4.8 \times 10^{-6}\,\mathrm{K}^{-1}$ (Ref. 129) should be large enough

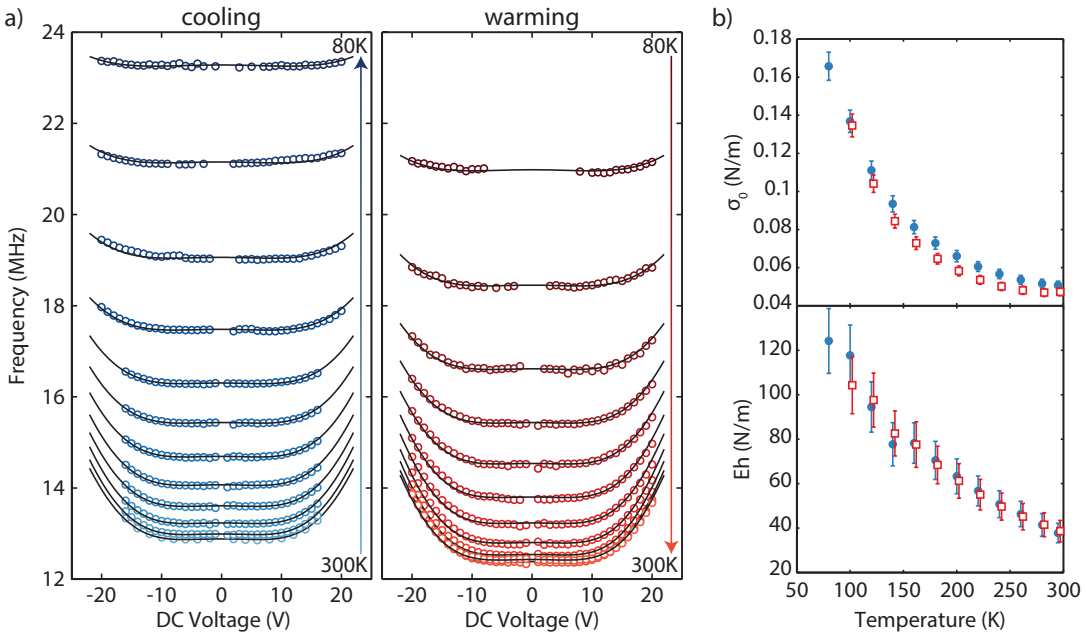

Figure 5.4: **Low-temperature frequency measurements of Device 1.** (a) Measured resonant frequencies (circles) versus V_{dc} at multiple temperatures during cooling (left panel) and heating (right panel). Black lines are the fits to the data at each temperature. (b) The membrane intrinsic tension σ_0 and modulus Eh extracted from the fits in (a). Filled circles are data taken during cooling, and open squares are data taken during warming.

in magnitude to counter the thermal contraction of the surrounding Si substrate with $\alpha_{\mathrm{Si}} \approx 2.6 \times 10^{-6}\,\mathrm{K}^{-1}$. Furthermore, our measured values for Eh at 300 K are much smaller than the 340 N/m expected for ideal graphene. This incredible softening of CVD graphene has been studied previously in great detail, and is likely due to grain boundaries and nm-scale ripples in the membrane surface [91]. The variation in Eh between our two devices is also consistent with previous experiments [91, 134].

The behavior of our devices within the entire temperature range of 80 K – 550 K is summarized in Figures 5.6 & 5.7. Here, the resonant frequency ω_0 and

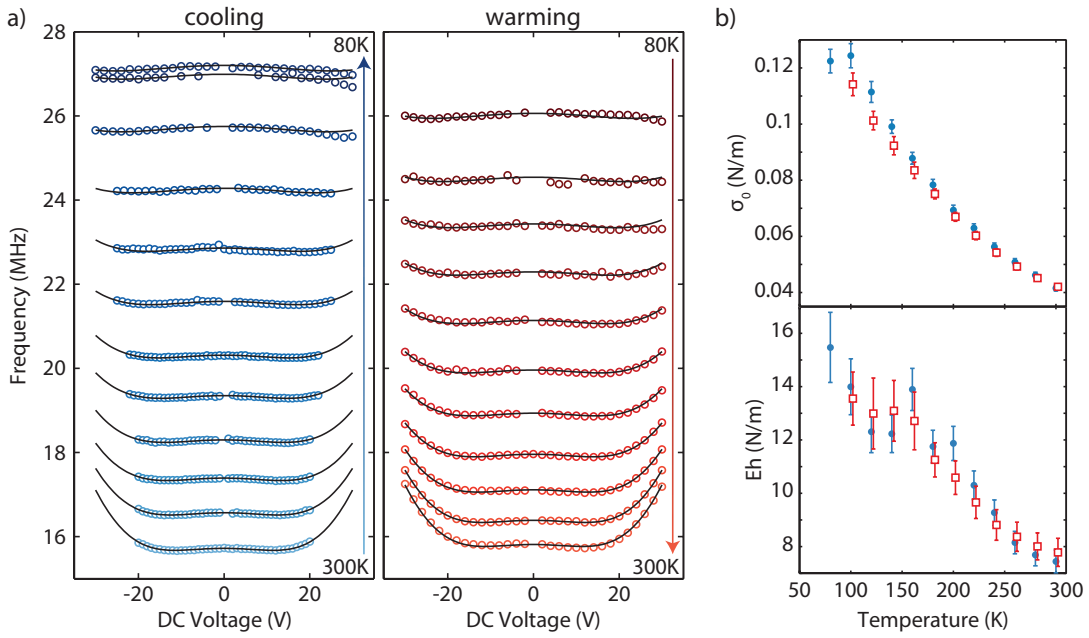

Figure 5.5: **Low-temperature frequency measurements of Device 2.** (a,b) Similar results to the previous figure, taken using Device 2.

quality factor Q were measured (from continuously running linescans) using constant voltage V_{dc} as the temperature was varied. Both devices are located on the same substrate (*i.e.* the same Si chip), so although only one device could be monitored during any given temperature cycle, both devices share the same thermal history. Low temperature data in Figure 5.6 was measured simultaneously with data in Figure 5.4, using a voltage of $V_{dc} = -16\,\mathrm{V}$. We observe greatly enhanced Q factors at low temperatures, consistent with previous experiments [10, 30], and slight hysteresis in ω_0 upon returning to 300 K. During heating to 520 K, V_{dc} sweeps were performed on Device 1 in 20 K increments in order to track its mechanical parameters (ρ, τ_0, Eh) as was done at cryogenic temperatures. This, however, led to degradation of the resonant frequency and Q, as evidenced in Figure 5.6. At the highest temperatures, downward shifts in frequency were observed immediately after each V_{dc} sweep, possibly due to

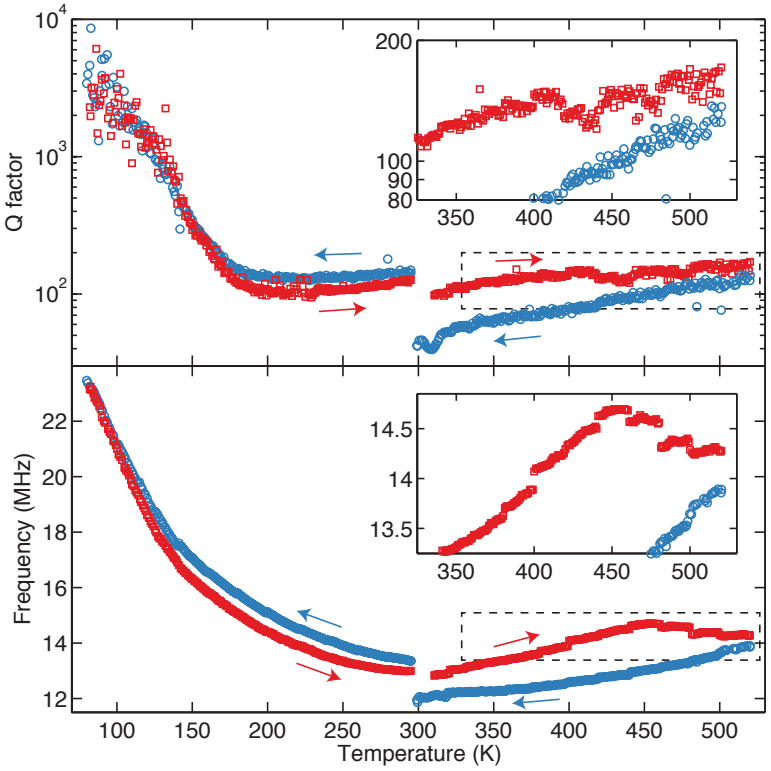

Figure 5.6: **Resonant frequency and Q of Device 1 over the entire temperature range.** Red squares: data taken while warming. Blue circles: data taken while cooling. Arrows indicate the direction of the temperature ramp. Insets: Magnified images of the dashed regions; these show "slipping events" caused by gate voltage V_{dc} scans at high temperatures, which are characterized by irreversible downward shifts in frequency and Q.

slipping of the graphene on the substrate or to a conformational change of polymer contaminants on the graphene. The observed hysteresis upon returning to 300 K was irreversible, and the measured values for ρ, σ_0, and Eh during the cycle (not shown here) were erratic. Upon a second heating cycle to 550 K (not shown), Device 1 failed and was thereafter unusable.

The data shown in Figure 5.7 for Device 2 was measured without intermediate V_{dc} sweeps; a constant voltage of $V_{dc} = 3$ V was maintained throughout.

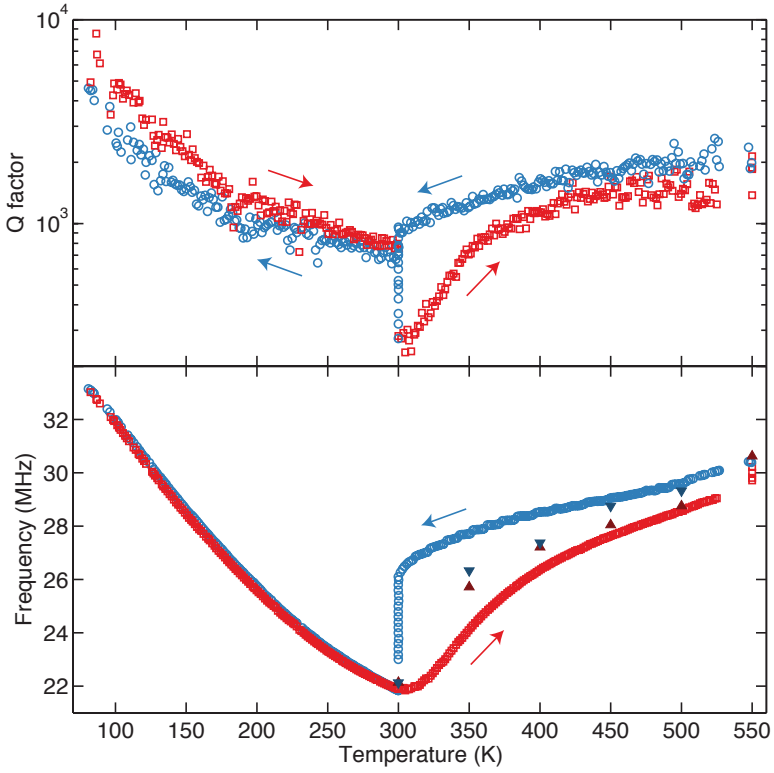

Figure 5.7: **Resonant frequency and Q of Device 2 over the entire temperature range.** Red squares: data taken while warming. Blue circles: data taken while cooling. Arrows indicate the direction of the temperature ramp. Above 300 K, a continuous heating rate of 0.2 K/min was used. In lower panel, triangles represent saturation frequencies measured during a subsequent heating cycle in which the temperature was varied in 50 K increments; here each temperature was held constant for several hours to allow the membrane to reach equilibrium. Upward (downward) triangles: saturations frequencies measured during heating (cooling).

Considerable hysteresis is seen during the 300 K – 550 K heating cycle, but this proved to be completely reversible. Multiple heating cycles at various heating rates produced similar results to those shown. We observed that when maintaining a fixed temperature (*e.g.* at 550 K or 300 K in Fig. 5.7), the resonant frequency (and the Q) of the membrane evolves exponentially in time as $\omega_0(t) - \omega_{\text{sat}} \propto e^{-t/\tau}$, where ω_{sat} and τ are the saturation value and time constant,

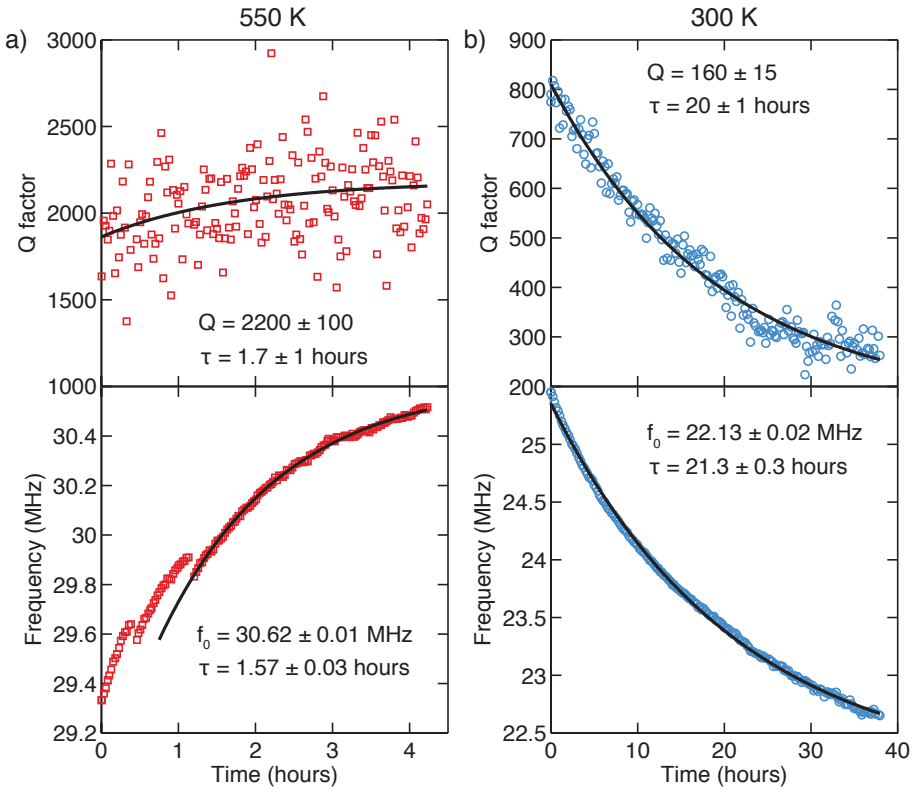

Figure 5.8: **Evolution of Device 2 at fixed temperature.** A portion of the frequency and Q data shown in Figure 5.7, plotted versus time. Values were continuously measured while maintaining fixed temperature (a) at $T = 550\,\mathrm{K}$, and (b) after returning to room temperature $T = 300\,\mathrm{K}$. The black line in each panel is an exponential fit to the data, with saturation values and time constants τ as shown. In (a), abrupt jumps in frequency are caused by refocusing of the detection laser beam.

respectively. This is depicted in Figure 5.8. In order to study this behavior further, a second heating cycle was preformed in which the temperature was varied in 50 K increments and maintained at each temperature for several hours. The resulting saturation frequencies are shown in Figure 5.7, and display a near complete closing of the hysteresis loop. Interestingly, time constants measured during heating (upward triangles) were typically $1 - 2$ hours, while those measured during cooling (downward triangles) were typically $12 - 24$ hours.

We note that the data for Device 2 shown in Figures 5.7 & 5.8 was taken after all measurements of Device 1 (meaning that the device had previously been cycled to 80 K and 550 K), but prior to the measurements shown in Figure 5.5. In the intervening time between the measurements of Figures 5.7 & 5.5 (12 weeks in total), the device was stored under vacuum and electrically grounded at $V_{dc} = 0$. Still, there was a marked change in resonant frequency at 300 K between measurements, the source of which remains unknown.

There are several observed thermal effects in our two devices which are wholly unexpected for pristine graphene membranes. These include: 1) a non-monotonic resonant frequency as a function of temperature, 2) a strongly temperature-dependent 2D modulus Eh, and 3) long time constants for frequency relaxation after heating. We conjecture that all of these effects can be explained by a thin layer of polymer residue (most likely the PMMA used during fabrication) on the graphene surface. A thin film ($1 - 2$ nm) of PMMA is known to persist on CVD graphene even after standard annealing methods are implemented to remove it [33, 135]. Furthermore, even devices made using mechanically exfoliated graphene typically require PMMA at some point during fabrication, and such membranes also have mass densities which are up to 10 times larger than pure monolayer graphene [10].

We can model our membranes as consisting of monolayer graphene with modulus, thickness, and TEC given by E_g, h_g, and α_g coated by a polymer film with corresponding parameters E_p, h_p, and α_p. The effective 2D modulus and TEC of the composite membrane can then be approximated as [136, 137]:

$$Eh = E_g h_g + E_p h_p \tag{5.2}$$

$$\alpha = \frac{\alpha_g E_g h_g + \alpha_p E_p h_p}{E_g h_g + E_p h_p} \tag{5.3}$$

Here all the parameters E_g, E_p, α_g, α_p are expected to be functions of temperature. The tension σ_0 of such a composite membrane would then depend on temperature as:

$$\sigma_0(T) = E_g h_g \varepsilon_{300\mathrm{K}} + Eh \int_{300\mathrm{K}}^{T} \Big(\alpha(T') - \alpha_{\mathrm{Si}}(T')\Big) dT' \tag{5.4}$$

Here $\varepsilon_{300\mathrm{K}}$ is the graphene strain at room temperature, and $\alpha_{\mathrm{Si}}(T)$ is the TEC of the surrounding substrate. For consistency with our experimental observations (discussed below) we have assumed in Eq. 5.4 that the polymer has zero strain at room temperature. Note that temperature-dependence of σ_0 arises not only due to thermal expansion but also from the temperature-dependent moduli. Within our experimental temperature range of $80 - 550\,\mathrm{K}$, the substrate expansion $\alpha_{\mathrm{Si}} \lesssim 3.7 \times 10^{-6}\,\mathrm{K}^{-1}$ is expected to be smaller in magnitude than either graphene or PMMA [138, 139].

Using reported values for the volumetric mass density [140], modulus [141], and TEC [142] of bulk PMMA ($1.1\,\mathrm{kg/m^3}$, $E_p = 3\,\mathrm{GPa}$, and $\alpha_p = 8 \times 10^{-5}\,\mathrm{K}^{-1}$ at room temperature) we can estimate the thickness of our polymer films and their contribution to the overall membrane TEC as given by Eq. 5.3. Of course the material properties of PMMA can vary based on molecular weight and can differ between bulk material and thin films, but this will suffice to give a qualitative explanation of our observations. The measured mass densities of our membranes of $\rho \approx 6 - 7$ graphene monolayers suggests the polymer films have thickness $h_p \approx 3 - 4\,\mathrm{nm}$. This would lead to a 2D modulus of $E_p h_p \approx 10\,\mathrm{N/m}$, which is comparable to the total moduli Eh we have measured (shown in Figs. 5.4 (b) & 5.5 (b)). For both of our devices, this then suggests a 2D graphene modulus of $E_g h_g < 30\,\mathrm{N/m}$ at room temperature based on Eq. 5.2. Substituting these numbers into Eq. 5.3 (with $\alpha_p = 8 \times 10^{-5}\,\mathrm{K}^{-1}$ and $\alpha_g \approx -5 \times 10^{-6}\,\mathrm{K}^{-1}$) then reveals that the TEC of PMMA should dominate the composite membrane TEC at room tem-

perature. Furthermore, because the TEC and modulus of graphene are expected to remain roughly constant at low temperatures [129], while for polymers (and PMMA specifically) the modulus is expected to rise [143], the composite membrane should continue to have a TEC $\alpha > 0$ below 300 K. This is consistent with our measurements of $\sigma_0(T)$ and $\omega_0(T)$ as presented in Figs. 5.4 - 5.7, as well as our observed increase in Eh at low temperatures.

At some temperature $T > 300$ K, PMMA is expected to pass through its glass transition. During this transition, it changes from a rigid, glass-like state to a soft, rubbery state; this is characterized by a sudden drop in Young's modulus E_p by up to three orders of magnitude [143]. Therefore when our composite membrane passes through the glass transition temperature, its TEC $\alpha(T)$ should transition from being PMMA-dominated to graphene-dominated, and we should observe a sudden transition from $\alpha > 0$ to $\alpha < 0$. For bulk PMMA, the glass transition temperature occurs at $T \approx 380$ K [144], but this transition is known to shift to lower temperatures as the film thickness decreases [145–149]. We thus interpret the minimum in resonant frequency observed for Device 2 at $T \approx 315$ K (in Figure 5.7) as indicative of the PMMA passing through its glass transition, and giving way to the negative thermal expansion of graphene α_g at higher temperatures. Because this transition (and the inferred sudden drop in E_p) is not accompanied by a sudden downward frequency shift, we assume that the temperature-independent strain component $\varepsilon_{300\text{K}}$ in Eq. 5.4 is present only in the graphene layer. That is to say, the PMMA has negligible strain at 300 K.

The hysteresis and long time constants seen in Figures 5.7 & 5.8 are also consistent with polymer relaxation. The long time constants observed can be a sign of creep (*i.e.* very slow deformation) of the polymer in response to the

ever-present tensile stress applied to it by the graphene – both in the glassy and rubbery states [150–152]. Particularly during cooling and vitrification (*i.e.* re-entering the glassy state), relaxation times in polymers are known to increase dramatically; timescales of several hours are common near the glass transition [144, 153]. Because the polymer layers on our devices are only a few molecular chains thick and under constant stress from the graphene, time constants for creep and relaxation may vary substantially from that expected of bulk PMMA. The previously mentioned downward shift in resonant frequency observed in Device 2 between Figures 5.5 & 5.7 over 12 weeks may even be a result of aging of the PMMA [154].

An alternate explanation for the long time constants observed in Device 2 above 300 K is that mass (*e.g.* trace gas in the vacuum chamber) is adsorbing onto or desorbing from the membrane surface – despite the low pressures $\sim 10^{-6}$ Torr used. Such an effect would be consistent with the slow rise in frequency at 550 K and fall in frequency at 300 K shown in Figure 5.8, as adsorbates leave the membrane at high temperatures and are re-adsorbed (at a much slower rate) at low temperatures. Attempts to discount this theory – by performing V_{dc} sweeps to measure ρ during the frequency relation at 300 K – have thus far been inconclusive. This effect may thus contribute to the apparent negative TEC observed above 315 K, and further testing is needed. For the frequency decay observed in Figure 5.8 at 300 K to be entirely adsorbate-driven, a change in frequency from 26 MHz to 22 MHz implies a 40% increase in mass (assuming tension is constant). Using the measured value of $\rho = 6.1$ monolayers in steady state at 300 K, this corresponds to an increase in mass of roughly 2 graphene monolayers.

In summary, we have studied the mechanical properties of two tensioned CVD graphene membranes under vacuum in the temperature range of 80 K – 550 K. We observe a number of behavioral responses of the membranes that are inconsistent with our expectations for pristine, single crystal graphene. Namely: 1) The measured mass density ρ corresponds to $6 - 7$ times that of monolayer graphene. 2) The measured membrane tension σ_0 and 2D modulus Eh both increase as the temperature is decreased below 300 K, in contrast to the expectations of a negative TEC and constant modulus. 3) The resonant frequency has a minimum at $T \approx 315$ K. 4) The resonant frequency evolves with long time constants of $1 - 2$ hours during heating above room temperature, and $12 - 24$ hours while cooling back to room temperature. All of these observations are suggestive of a thin $1 - 4$ nm film of PMMA residue on the graphene surface, although the high temperature measurements may be confounded by desorption and adsorption of gasses in our high vacuum test chamber. These results suggest that while graphene mechanical resonators benefit from the low mass and electrical conductivity of graphene, many of the mechanical behaviors of these devices are ultimately dominated by polymer contaminants. The loss modulus of PMMA may also play a dominant role in determining the Q factor of graphene devices, which are known to be substantially lower than most other MEMS/NEMS membrane systems [31].

5.3 Effect of including 3 parameters in the low-temperature fits

As discussed in Section 5.2, fits to the resonant frequency ω_0 versus gate voltage V_{dc} become increasingly difficult to perform at low temperatures, where the membrane tension σ_0 increases significantly and the effect of V_{dc} on ω_0 is therefore reduced. It was thus determined that in order to extract meaningful results from the fits, the membrane mass density ρ should be constrained to its fitted value at 300 K. Figure 5.9 shows the results of fits to the low temperature data (Figs. 5.4 (a) & 5.5 (a)) in which the mass was not constrained. These should be compared to Figs. 5.4 (b) & 5.5 (b) in Section 5.2, in which ρ was constrained.

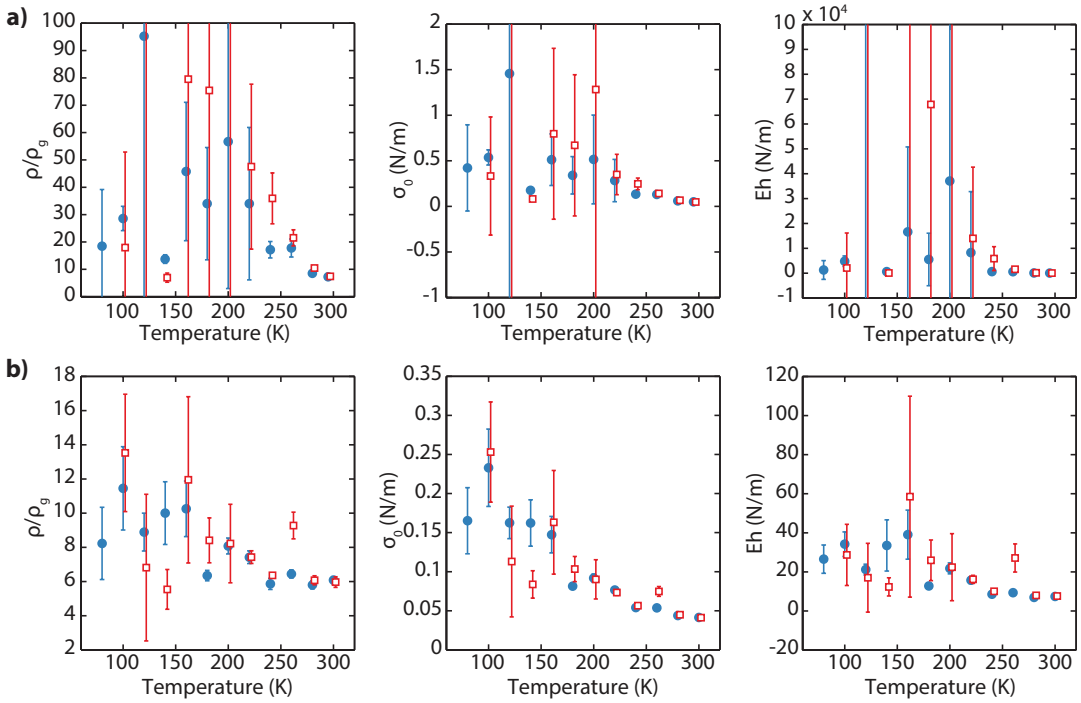

Figure 5.9: **Results of 3-parameter fits.** Mass density ρ (in units of ρ_g, the density of monolayer graphene), built-in tension σ_0, and modulus Eh versus temperature for (a) Device 1 and (b) Device 2. Blue circles: values measured during cooling to 80 K. Red squares: values measured during heating to 300 K

5.4 Modeling the membrane frequency vs gate voltage

5.4.1 Calculating the resonant frequency of a nonlinear tensioned membrane

As described in Section 3.3, the Lagrangian of a tensioned membrane under electroscatic loading is:

$$\begin{aligned} L = \frac{\rho}{2}\int dA\dot{x}^2 - \frac{D}{2}\int dA(\Delta x)^2 - \frac{C}{16}\left[\frac{1}{A}\int dA(\nabla x)^2\right]\cdot\int dA(\nabla x)^2 \\ - \frac{\sigma_0}{2}\int dA(\nabla x)^2 + \frac{\epsilon_0 V_{dc}^2}{2}\int \frac{dA}{d-x} \end{aligned} \tag{5.5}$$

where each integral is over the membrane area A, x is the membrane's out-of-plane deformation, ρ is the surface density, $D = Yh^3/(12(1-\nu^2))$ and $C = Yh/(1-\nu^2)$ are the bending stiffness and tensile stiffness, σ_0 is the built-in tension, V_{dc} is the applied gate voltage, and d is the gate-membrane separation. Y and ν are the Young's modulus and Poisson ratio, respectively, and h is the membrane thickness. We can express the membrane's out-of-plane deformation $x(\vec{r},t)$ as a sum of static and harmonic parts:

$$x(\vec{r},t) = x_0\xi_0(\vec{r}) + x_i(t)\xi_i(\vec{r}). \tag{5.6}$$

Here we have included only the motion of a single mechanical eigenmode i. Also, we have introduced x_0 and $x_i(t)$, which denote the membrane deflection at its antinode. $\xi_0(\vec{r})$ and $\xi_i(\vec{r})$ describe the shape of the static deformation and of mode i, both normalized such that $|\xi(\vec{r})| \leq 1$.

As shown in Section 3.3, expressing the deflection in this way allows us to rewrite the Lagrangian as that of a nonlinear 1-Dimensional harmonic oscillator:

$$L = \frac{\rho}{2}\dot{x}_i^2\int dA\xi_i^2 - \frac{\sigma}{2}x_i^2\int dA(\nabla\xi_i)^2 - L_i x_i - S_i x_i^2 - T_i x_i^3 - F_i x_i^4 \tag{5.7}$$

where

$$\sigma = \sigma_0 + \frac{Cx_0^2}{4A}\int dA(\nabla\xi_0)^2 \tag{5.8}$$

$$L_i = \left[\sigma_0 + \frac{Cx_0^2}{4A}\int dA(\nabla\xi_0)^2\right]\cdot x_0 \int dA(\nabla\xi_0\nabla\xi_i) \tag{5.9}$$

$$S_i = \frac{Cx_0^2}{4A}\left[\int dA(\nabla\xi_0\nabla\xi_i)\right]^2 \tag{5.10}$$

$$T_i = \frac{Cx_0}{4A}\left[\int dA(\nabla\xi_0\nabla\xi_i)\right]\cdot\int dA(\nabla\xi_i)^2 \tag{5.11}$$

$$F_i = \frac{C}{16A}\left[\int dA(\nabla\xi_i)^2\right]^2 \tag{5.12}$$

Eq. 5.8 represents the change in membrane tension due to the static deflection x_0. Nonlinearites due to the flexural rigidity D (plate-bending terms) in Eq. 5.5 have been neglected in Eq. 5.7 since $h^2/A \ll 1$. Nonlinear electrostatic terms have been neglected for now, but will be reintroduced in the next subsection.

The mechanics of mode i can be determined by applying the Euler-Lagrange equation toEq. 5.7:

$$\frac{d}{dt}\left(\frac{\partial L}{\partial \dot{x}_i}\right) - \frac{\partial L}{\partial x_i} = 0 \tag{5.13}$$

which leads to

$$\rho\ddot{x}_i\int dA\xi_i^2 + \sigma x_i\int dA(\nabla\xi_i)^2 + L_i + 2S_i x_i + 3T_i x_i^2 + 4T_i x_i^3 = 0 \tag{5.14}$$

Dividing each term above by the effective mass $m_i = \rho\int dA\xi_i^2$ thus produces the familiar harmonic oscillator result:

$$\ddot{x}_i + \omega_i^2 x_i + \{\text{nonlinear terms}\} = 0. \tag{5.15}$$

This represents the undamped harmonic oscillator; a phenomenological damping force $\gamma\dot{x}$ is typically added in as well. The resonant frequency of mode i, ω_i, is thus given by:

$$\omega_i = \sqrt{\frac{\sigma\int dA(\nabla\xi_i)^2}{\rho\int dA\xi_i^2}}. \tag{5.16}$$

To test this result, we can compare it to the known eigenmodes and eigenfrequencies of circular or square membranes. For circles we know that $\xi_i = \xi_{m,n} = J_m(\frac{\alpha_{m,n}r}{R})\cos(m\theta)$, where (r,θ) are polar coordinates, R is the membrane radius, J_m is the m-th Bessel function and $\alpha_{m,n}$ is its n-th root. For the fundamental mode $(m,n) = (0,1)$, we have $\nabla\xi_i = \frac{d}{dr}J_0\left(\frac{\alpha_{0,1}r}{R}\right) = -\frac{\alpha_{0,1}}{R}\cdot J_1\left(\frac{\alpha_{0,1}r}{R}\right)$. Eq. 5.16 then gives

$$\omega_{0,1} = \sqrt{\frac{\sigma\int rdr\left(\frac{\alpha_{0,1}}{R}\cdot J_1\left(\frac{\alpha_{0,1}r}{R}\right)\right)^2}{\rho\int rdr\left(J_0\left(\frac{\alpha_{0,1}r}{R}\right)\right)^2}} = \sqrt{\frac{\sigma\left(\frac{\alpha_{0,1}}{R}\right)^2\cdot\frac{1}{2}J_1(\alpha_{0,1})^2}{\rho\cdot\frac{1}{2}J_1(\alpha_{0,1})^2}} = \frac{\alpha_{0,1}}{R}\sqrt{\frac{\sigma}{\rho}} \tag{5.17}$$

where computer algebra software (Ref. 155) was used to evaluate the integrals. This result reproduces the well-known fundamental frequency of a circular drum. Eq. 5.16 can similarly predict the full spectrum of circular membrane frequencies $\omega_{m,n} = \frac{\alpha_{m,n}}{R}\sqrt{\frac{\sigma}{\rho}}$, however the integration becomes more arduous for a general (m,n). It can likewise be applied to a rectangular membrane $\xi_{m,n} = \sin\left(\frac{m\pi x}{a}\right)\sin\left(\frac{n\pi y}{b}\right)$ to obtain the expected $\omega_{m,n} = \pi\sqrt{\frac{\sigma}{\rho}\left[\left(\frac{m}{a}\right)^2 + \left(\frac{n}{b}\right)^2\right]}$.

The term $\rho\int dA\xi_i^2$ in Eq. 5.14 is commonly referred to as the effective mass m_i of mode i [15, 156, 157], and this concept can be extremely useful when mathematically reducing the 2-dimensional membrane to a 1-dimensional harmonic oscillator (*e.g.* Eq. 5.15). This 1-dimensional analogy goes so far as to accurately describe the thermal oscillations of x_i. Invoking the equipartition theorem, the time-averaged thermal amplitude $\langle x_i^2(t)\rangle$ is related to the ambient temperature T by:

$$\frac{1}{2}m_i\omega_i^2\langle x_i^2(t)\rangle = \frac{1}{2}k_BT. \tag{5.18}$$

Similarly, the quantum zero-point fluctuations of x_i (oscillations expected at $T = 0$) are:

$$\langle x_i^2\rangle_{\text{zpf}} = \frac{\hbar}{2m_i\omega_i}. \tag{5.19}$$

Lists of effective masses for several modes of common MEMs geometries (membranes, cantilevers, doubly- clamped bridges) are given in Ref. 156.

5.4.2 Contribution of capacitive softening

The electrostatic term in Eq. 5.5 can be approximated as:

$$\frac{\epsilon_0 V_{dc}^2}{2}\int \frac{dA}{d-x} \approx \frac{\epsilon_0 V_{dc}^2}{2d}\int\left(1+\frac{x}{d}+\frac{x^2}{d^2}+\frac{x^3}{d^3}\right) \tag{5.20}$$

These terms will play a role in determining the resonant frequency of our membrane as well as its nonlinear coefficients. In order to incorporate these terms into our model, we must substitute $x = x_0\xi_0 + x_i\xi_i$ into Eq. 5.20 and collect terms in powers of x_i. Once this is done, application of the Euler-Lagrange equation to Eq. 5.7 gives the following equation of motion:

$$\ddot{x}_i + \gamma_i\dot{x}_i + \left(\omega_i^2 + \frac{2\mathcal{S}_i}{m_i}\right)x_i + \frac{\mathcal{L}_i}{m_i} + \frac{3\mathcal{T}_i}{m_i}x_i^2 + \frac{4\mathcal{F}_i}{m_i}x_i^3 = 0 \tag{5.21}$$

where the coefficients $\mathcal{L}_i, \mathcal{S}_i, \mathcal{T}_i, \mathcal{F}_i$ are a sum of the tension-based terms (Eqs. 5.9-5.12) and the electrostatic terms given by Eq. 5.20. Thus we now have:

$$\mathcal{L}_i = \left(\sigma_0 + \frac{Cx_0^2}{4A}\mathbb{I}_{00}\right)x_0\mathbb{I}_{0i} - \frac{\epsilon_0 V_{dc}^2 A}{2d^2}\left[\mathbb{K}_i + \frac{x_0}{d}2\mathbb{K}_{0i} + \frac{x_0^2}{d^2}3\mathbb{K}_{00i} + \frac{x_0^3}{d^3}4\mathbb{K}_{000i}\right] \tag{5.22}$$

$$\mathcal{S}_i = \frac{Cx_0^2}{4A}\mathbb{I}_{0i}^2 - \frac{\epsilon_0 V_{dc}^2 A}{2d^3}\left[\mathbb{K}_{ii} + \frac{x_0}{d}3\mathbb{K}_{0ii} + \frac{x_0^2}{d^2}6\mathbb{K}_{00ii}\right] \tag{5.23}$$

$$\mathcal{T}_i = \frac{Cx_0}{4A}\mathbb{I}_{0i}\mathbb{I}_{ii} - \frac{\epsilon_0 V_{dc}^2 A}{2d^4}\left[\mathbb{K}_{iii} + \frac{x_0}{d}4\mathbb{K}_{0iii}\right] \tag{5.24}$$

$$\mathcal{F}_i = \frac{C}{16A}\mathbb{I}_{ii}^2 - \frac{\epsilon_0 V_{dc}^2 A}{2d^5}\mathbb{K}_{iiii} \tag{5.25}$$

$$\omega_i^2 = \frac{1}{m_i}\left(\sigma_0 + \frac{Cx_0^2}{4A}\mathbb{I}_{00}\right)\mathbb{I}_{ii} \tag{5.26}$$

$$m_i = \rho A\mathbb{K}_{ii} \tag{5.27}$$

where we have introduced the symbols $\mathbb{I}_{mn}$ and $\mathbb{K}_{jklm}$. These are a set of dimensionless numbers (different for each eigenmode) that are found by solving the integrals $\mathbb{I}_{mn} = \int dA(\nabla\xi_m\nabla\xi_n)$ and $\mathbb{K}_{jklm} = (1/A)\int dA\xi_j\xi_k\xi_l\xi_m$. The full set of these integrals (to 3$^{\text{rd}}$ order in x_0/d) are given in Section 5.4.5 for the fundamental mode of a circular membrane.

Based on Eq. 5.21, the resonant frequency Ω_i of our membrane is given by $\Omega_i^2 = \omega_i^2 + 2\mathcal{S}_i/m_i$. Furthermore, we have Duffing coefficients given by the cubic restoring force $(4\mathcal{F}_i/m_i)x_i^3$ and quadratic restoring force $(3\mathcal{T}_i/m_i)x_i^2$. And Eqs. 5.22 - 5.27 tell us precisely how each of these terms depends on the membrane modulus C, static displacement x_0, and gate voltage V_{dc}. Another added layer of complexity would be to calculate how the constant term $\mathcal{L}_i$ in Eq. 5.21 affects the equilibrium position of x_i, which would in turn slightly change the resonant frequency because of the nonlinear forces $\mathcal{T}_i$ and $\mathcal{F}_i$. This turns out to be a small correction to the resonant frequency Ω_i.

The only remaining piece of the puzzle is to determine the static membrane deflection x_0 as a function of applied gate voltage V_{dc}.

5.4.3 Static membrane deflection x_0 vs V_{dc}

Our task is now to determine the static deflection of the membrane center x_0 and the static membrane profile ξ_0. One approach is to simply balance the total vertical forces acting on the membrane. Using the parallel-plate capacitor approximation, the force exerted by the gate voltage on the graphene is $F_{dc} = -\epsilon_0 A V_{dc}^2/(2d^2)$. This downward force is balanced all along the circumference of the membrane by an upward tension force of $F_\sigma = 2\pi R\sigma \sin\theta$, where θ is the contact angle with the substrate. This is depicted schematically in Figure 5.10.

If we approximate the static membrane profile as a paraboloid $\xi_0(r) = 1 - r^2/R^2$ and use a small angle approximation, we can use the simple expression $\sin\theta \approx \tan\theta = d\xi_0/dr|_{r=R} = -2x_0/R$. Balance of the upward and downward forces

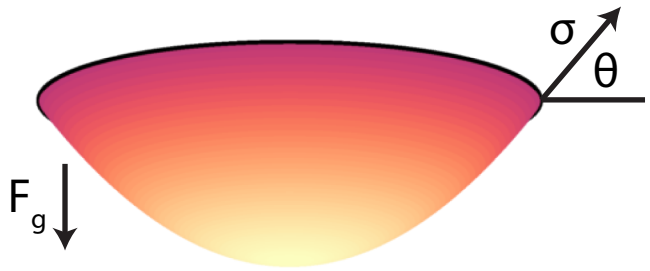

Figure 5.10: Balance of forces in the static membrane.

then gives a relation between x_0 and V_{dc}:

$$x_0 = \frac{\epsilon_0 A V_{dc}^2}{8\pi d^2 \sigma} \tag{5.28}$$

A second (perhaps more rigorous) approach to calculating x_0 is to consider only static deformation in the original Lagrangian Eq. 5.5 (*i.e.* to set $x = x_0\xi_0$) and then apply the Euler-Lagrange equation. Because there is no time-dependence, this simplifies to $\partial L/\partial x_0 = 0$. Using Eq. 5.20 to approximate the electrostatic terms, this approach produces the result

$$-\sigma x_0 \mathbb{I}_{00} + \frac{\epsilon_0 V_{dc}^2 A}{2d^2}\left[\mathbb{K}_0 + \frac{x_0}{d}2\mathbb{K}_{00} + \frac{x_0^2}{d^2}3\mathbb{K}_{000}\right] = 0 \tag{5.29}$$

where, as in earlier sections, the total tension is

$$\sigma = \sigma_0 + \frac{C x_0^2}{4A}\mathbb{I}_{00} \tag{5.30}$$

In the experimentally relevant limit of $x_0/d \ll 1$, Eq. 5.29 reduces to

$$x_0 = \frac{\epsilon_0 A V_{dc}^2 \mathbb{K}_0}{2d^2 \sigma \mathbb{I}_{00}} \tag{5.31}$$

which reproduces Eq. 5.28 if we use the same approximation of a parabolic membrane shape $\xi_0 = 1 - r^2/R^2$. See Section 5.4.5 for the relevant integrals $\mathbb{I}_{00}$ and $\mathbb{K}_0$.

5.4.4 The final fitting function

Combining the results of Eqs. 5.21 & 5.31 (and neglecting terms of order x_0/d and higher) gives the following equation for the resonant frequency Ω_i:

$$\Omega_i^2 = \omega_i^2 + \frac{2\mathcal{S}_i}{m_i} \tag{5.32}$$

$$= \frac{\mathbb{I}_{ii}\sigma_0}{\mathbb{K}_{ii}\rho A} - \frac{\epsilon_0 V_{dc}^2}{2d^3} + \frac{C\epsilon_0^2 V_{dc}^4}{d^4\rho\sigma^2}\frac{\mathbb{K}_0^2(\mathbb{I}_{00}\mathbb{I}_{ii} + 2\mathbb{I}_{0i}^2)}{16\mathbb{K}_{ii}\mathbb{I}_{00}^2} \tag{5.33}$$

The various dimensionless integrals $\mathbb{I}$ and $\mathbb{K}$ are given in Section 5.4.5 for the fundamental mode of a circular membrane. If we substitute these values in, the above equation becomes

$$\Omega_1^2 = \frac{\alpha^2\sigma_0}{R^2\rho} - \frac{\epsilon_0 V_{dc}^2}{d^3\rho} + \frac{\beta C\epsilon_0^2 V_{dc}^4}{d^4\rho\sigma^2} \tag{5.34}$$

where $\alpha = 2.4048$ and $\beta = 0.1316$, reproducing Eq. 5.1. Note that the V_{dc}^4 term above depends on the total tension σ rather than the intrinsic tension σ_0. The fitting routine used throughout Section 5.2 to fit our data indeed used this total tension. The fitting function was therefore not a simple polynomial, but incorporated Eqs. 5.30 & 5.31 to better match the data – particularly at high voltages where σ_0 is no longer a good approximation for σ.

5.4.5 Useful Integrals

The following integrals are helpful when calculating nonlinear contributions to the Lagrangian of a circular tensioned membrane. The static out-of-plane profile is assumed to be quadratic $\xi_0 = 1 - r^2/R^2$, and the first resonant mode is assumed to be a Bessel function $\xi_1 = J_0(\alpha_{0,1} r/R)$.

$$\mathbb{I}_{00} = \int dA(\nabla\xi_0)^2 = 2\pi \tag{5.35}$$

$$\mathbb{I}_{11} = \int dA(\nabla\xi_1)^2 = \pi\alpha_{0,1}^2 J_1(\alpha_{0,1})^2 \approx \pi \times 1.558650 \tag{5.36}$$

$$\mathbb{I}_{01} = \int dA(\nabla\xi_0)(\nabla\xi_1) = \pi 4 J_2(\alpha_{0,1}) \approx \pi \times 1.727019 \tag{5.37}$$

$$\mathbb{K}_0 = \frac{1}{A}\int dA\xi_0 = \frac{1}{2} \tag{5.38}$$

$$\mathbb{K}_{00} = \frac{1}{A}\int dA(\xi_0)^2 = \frac{1}{3} \tag{5.39}$$

$$\mathbb{K}_{000} = \frac{1}{A}\int dA(\xi_0)^3 = \frac{1}{4} \tag{5.40}$$

$$\mathbb{K}_1 = \frac{1}{A}\int dA\xi_1 = \frac{2J_1(\alpha_{0,1})}{\alpha_{0,1}} \approx 0.431755 \tag{5.41}$$

$$\mathbb{K}_{11} = \frac{1}{A}\int dA(\xi_1)^2 = J_1(\alpha_{01})^2 \approx 0.269514 \tag{5.42}$$

$$\mathbb{K}_{111} = \frac{1}{A}\int dA(\xi_1)^3 \approx 0.194923 \tag{5.43}$$

$$\mathbb{K}_{01} = \frac{1}{A}\int dA\xi_0\xi_1 = \frac{4J_2(\alpha_{0,1})}{\alpha_{0,1}^2} \approx 0.298628 \tag{5.44}$$

$$\mathbb{K}_{001} = \frac{1}{A}\int dA(\xi_0)^2\xi_1 = \left(\frac{2}{\alpha_{0,1}}\right)^4 (4J_2(\alpha_{0,1}) - \alpha_{0,1}J_1(\alpha_{0,1})) \approx 0.22894 \tag{5.45}$$

$$\mathbb{K}_{011} = \frac{1}{A}\int dA\xi_0(\xi_1)^2 = \frac{2(1+\alpha_{0,1})^2 J_1(\alpha_{0,1})^2}{3\alpha_{0,1}^2} \approx 0.210745 \tag{5.46}$$

Chapter 6

Conclusions and outlook

Throughout this thesis, we have explored several routes to exploit the nonlinear mechanics of two-dimensional membranes and one-dimensional wires.

In Chapter 2 we studied silicon nitride membrane resonators coated with CVD graphene in order to create high surface area, high Q factor, electrically integrated devices. This resulted in membranes with Q factors ranging from $\sim 20\,000$ to $250\,000$ and in which motion could be both driven and detected electrically. Moreover, the resonant frequency could be tuned at will using a gate voltage, similar to pure graphene membranes. Lastly, we demonstrated photothermal frequency and damping control in this system due to the graphene's absorption of laser light. The damping was varied by a factor of 4 simply by moving the membrane relative to a fixed mirror under constant illumination. It is likely that slightly higher laser power would have led to photothermal self-oscillation of this system.

In Chapter 3 we explored the coupling of energy between mechanical modes in a graphene membrane. We showed that by driving the membrane at a frequency corresponding to the "sideband" of two modes, the experimenter can enable energy exchange between them. With this effect, we demonstrated amplification of motion in a desired mode and mechanics-based frequency mixing in a MEMS device. While this effect can also be used to cool the thermal motion of a mode, it cannot be used to reach the quantum regime. This is because both modes – the mode being cooled and the "cavity mode" to which energy is diverted – have frequencies in the MHz range, and therefore have large phonon occupancies at experimentally accessible temperatures. However, current efforts to cool graphene into the quantum regime by coupling it to superconducting microwave cavities [13, 14] hold great promise. Once in the quantum ground state, the coupling we have demonstrated could be exploited to study the interactions of coupled quantum modes.

In Chapter 4 we presented a detailed study of photothermal self-oscillation in one-dimensional nanowires. We showed optically induced motion at incident laser powers of $\sim 1\,\mu$W, lower than has ever been demonstrated to our knowledge. We also applied perturbation theory to the governing differential equations to prove that the oscillation amplitude was set by two different effects: 1) a direct temperature-position coupling dz/dT, and 2) parametric excitation at twice the resonant frequency, caused by a temperature-frequency coupling $d\omega_0/dT$. We then demonstrated the use of the photothermal effect to overcome air damping in NEMS devices.

Lastly, in Chapter 5, we studied the behavior of graphene NEMS over a wide temperature range. We showed that the elastic modulus and tension increase as

the temperature is decreased below 300 K, and that the resonant frequency is not monotonic, but has a minimum at roughy 315 K. This suggests that the thermal expansion coefficient of graphene is positive for temperatures below 315 K, and negative for higher temperatures. We showed that when heated to 550 K and returned to 300 K, the resonant frequency of a graphene membrane displays considerable hysteresis. If then held steady at 300 K, the resonant frequency evolves exponentially in time, with a time constant of roughly 24 hours. Our results are consistent with suspicions that a 2 to 4 nm-thick film of polymer residue is present on the graphene surface. Slow adsorption and desorption of molecules in our vacuum test chamber (*e.g.* H_2O) could also be playing a role in the observed hysteresis and long time constants.

We set out to show that two-dimensional and one-dimensional NEMS devices had a wealth of interesting and useful nonlinear properties waiting to be explored and exploited. While this is true of both systems, graphene membranes at present seem hindered by surface contaminants. This is evidenced simply enough by their room temperature quality factors ($\sim$ 50 to 500), which are significantly lower than those of other membrane materials (*e.g.* silicon nitride) of comparable dimensions. New, cleaner processes to fabricate graphene devices without the use of polymers must be developed in order for these devices to reach their full potential – both as electromechanical elements and as sensors of ultra-weak forces and masses. Still, graphene is quite competitive for applications such as mass sensing because the ultimate sensitivity (see Eq. 1.4) depends on the ratio of membrane mass to Q factor. At low temperatures, the Q factors of graphene increase dramatically (see Refs. 10, 30 and Figs. 5.6 & 5.7), meaning it still holds great promise for low-temperature experiments and studies of quantum motion.

In future experiments and applications of graphene NEMS a key design element may be the split-back-gate design that we developed in Chapter 3. Here we used two semi-circular gates in order to separately drive symmetric and asymmetric modes, but more complex gate arrangements can also be used for tailor-made electric field patterns. This may enable the experimenter to drive vibration modes that are otherwise inaccessible, and could mean more modes for bit-wise information storage in NEMS memory devices [4, 22] or other as-yet unforeseen device applications.

Yet another exciting avenue in graphene NEMS is the creation of graphene heterostructures [158–160]. These structures consist of stacked layers of graphene and other atomically thin materials, including insulators such as hexagonal boron nitride (h-BN) and semiconductors such as the many Transition Metal Dichalcogenides (TMDs, *e.g.* MoS_2, $MoSe_2$, WS_2, etc.). To our knowledge such heterostructure devices have to present all been fabricated by exfoliation and on-substrate (*i.e.* not free-standing). However, as NEMS devices, graphene heterostructures would have novel electronic and optical interactions not seen in pure graphene – while still benefiting from the graphene's conductivity and frequency tunability. Pure TMD mechanical resonators have already been demonstrated [85, 161], and hold great promise in their own right.

For the case of optomechanics in nanowires, it would be useful to test our theory that longer cantilevers at either end of the wire would lead to significantly stronger photothermal effects. In order to do this, one could easily fabricate an array of such devices with varying cantilever length. By doing this, even lower laser thresholds than 1 μW can likely be achieved. Furthermore, performing a Deep Reactive Ion Etch rather than a wet etch of the underlying silicon

would likely result in a much smoother reflecting back-plane and improve the optical performance of these devices. Lastly, because the devices are coated with a thin metal film, it would be interesting to test whether a direct current can be applied across the wire to induce joule heating and (utilizing the dz/dT coupling) thereby have independent control of the nanowire distance from the reflecting back-plane. This could give the experimenter a means to enable or disable optically-induced self-oscillation without changing the laser power. If, on the other hand, an alternating current applied, this could be used to apply parametric excitation or to entrain the self-oscillating nanowire to a desired frequency. Further experiments are also needed to determine the dominant sources of phase noise in these devices (*e.g.* mechanical dissipation, laser power noise, or laser beam position jitter) and mitigate them, as a low phase noise is required in MEMS/NEMS time-keeping and frequency reference applications.

MEMS and NEMS structures today, while far simpler than the swimming micro-robots envisioned by Richard Feynman in 1983 [18], play integral roles in modern electronics and studies of fundamental physics. Reducing their dimensions to single-atom-thick graphene membranes or one-dimensional nanowires, and utilizing nonlinear behaviors of these devices, could hold the key to their next major applications in sensing or signal processing. Furthermore, these low-mass devices (with their large zero point motion) may also play vital roles in future studies of quantum motion. With the coming rise of quantum computing, mechanical resonators represent a new means to interface with qubits and other quantum systems. The future thus holds many exciting and yet unforeseen applications of these devices.

Bibliography

[1] Marek, J. & Gómez, U.-M. MEMS (micro-electro-mechanical systems) for automotive and consumer electronics. In *Chips 2020*, 293–314 (Springer, 2011).

[2] Li, M., Tang, H. X. & Roukes, M. L. Ultra-sensitive NEMS-based cantilevers for sensing, scanned probe and very high-frequency applications. *Nature Nanotechnology* **2**, 114–120 (2007).

[3] Chaste, J. *et al.* A nanomechanical mass sensor with yoctogram resolution. *Nature Nanotechnology* **7**, 301–304 (2012).

[4] Mahboob, I. & Yamaguchi, H. Bit storage and bit flip operations in an electromechanical oscillator. *Nature Nanotechnology* **3**, 275–279 (2008).

[5] O'Connell, A. D. *et al.* Quantum ground state and single-phonon control of a mechanical resonator. *Nature* **464**, 697–703 (2010).

[6] Teufel, J. D. *et al.* Circuit cavity electromechanics in the strong-coupling regime. *Nature* **471**, 204–208 (2011).

[7] Teufel, J. D. *et al.* Sideband cooling of micromechanical motion to the quantum ground state. *Nature* **475**, 359–363 (2011).

[8] Huang, P. Y. *et al.* Grains and grain boundaries in single-layer graphene atomic patchwork quilts. *Nature* **469**, 389–392 (2011).

[9] Bunch, J. S. *et al.* Electromechanical resonators from graphene sheets. *Science* **315**, 490–493 (2007).

[10] Chen, C. *et al.* Performance of monolayer graphene nanomechanical resonators with electrical readout. *Nature Nanotechnology* **4**, 861–867 (2009).

[11] Chen, C. *et al.* Graphene mechanical oscillators with tunable frequency. *Nature Nanotechnology* **8**, 923–927 (2013).

[12] Barton, R. A. *et al.* Photothermal self-oscillation and laser cooling of graphene optomechanical systems. *Nano Letters* **12**, 4681–4686 (2012).

[13] Weber, P., Guttinger, J., Tsioutsios, I., Chang, D. E. & Bachtold, A. Coupling graphene mechanical resonators to superconducting microwave cavities. *Nano Letters* **14**, 2854–2860 (2014).

[14] Singh, V. *et al.* Optomechanical coupling between a multilayer graphene mechanical resonator and a superconducting microwave cavity. *Nature Nanotechnology* **9**, 820–824 (2014).

[15] Aspelmeyer, M., Kippenberg, T. J. & Marquardt, F. Cavity optomechanics. *Reviews of Modern Physics* **86**, 1391 (2014).

[16] Blocher, D., Rand, R. H. & Zehnder, A. T. Multiple limit cycles in laser interference transduced resonators. *International Journal of Non-Linear Mechanics* **52**, 119–126 (2013).

[17] Aubin, K. *et al.* Limit cycle oscillations in CW laser-driven NEMS. *Journal of Microelectromechanical Systems* **13**, 1018–1026 (2004).

[18] Feynman, R. Infinitesimal machinery. *Journal of Microelectromechanical Systems* **2**, 4–14 (1993).

[19] Petersen, K. E. Silicon as a mechanical material. *Proceedings of the IEEE* **70**, 420–457 (1982).

[20] Judy, J. W. Microelectromechanical systems (MEMS): fabrication, design and applications. *Smart Materials and Structures* **10**, 1115 (2001).

[21] Waggoner, P. S. & Craighead, H. G. Micro-and nanomechanical sensors for environmental, chemical, and biological detection. *Lab on a Chip* **7**, 1238–1255 (2007).

[22] Mahboob, I., Mounaix, M., Nishiguchi, K., Fujiwara, A. & Yamaguchi, H. A multimode electromechanical parametric resonator array. *Scientific Reports* **4**, 4448 (2014).

[23] Antonio, D., Zanette, D. H. & López, D. Frequency stabilization in nonlinear micromechanical oscillators. *Nature Communications* **3**, 806 (2012).

[24] Villanueva, L. G. *et al.* A nanoscale parametric feedback oscillator. *Nano Letters* **11**, 5054–5059 (2011).

[25] Novoselov, K. S. *et al.* Electric field effect in atomically thin carbon films. *Science* **306**, 666–669 (2004).

[26] Castro Neto, A. H., Guinea, F., Peres, N. M. R., Novoselov, K. S. & Geim, A. K. The electronic properties of graphene. *Reviews of Modern Physics* **81**, 109 (2009).

[27] Lee, C., Wei, X., Kysar, J. W. & Hone, J. Measurement of the elastic prop-

erties and intrinsic strength of monolayer graphene. *Science* **321**, 385–388 (2008).

[28] Li, X. *et al.* Large-area synthesis of high-quality and uniform graphene films on copper foils. *Science* **324**, 1312–1314 (2009).

[29] Bae, S. *et al.* Roll-to-roll production of 30-inch graphene films for transparent electrodes. *Nature Nanotechnology* **5**, 574–578 (2010).

[30] van der Zande, A. M. *et al.* Large-scale arrays of single-layer graphene resonators. *Nano Letters* **10**, 4869–4873 (2010).

[31] Barton, R. A. *et al.* High, size-dependent quality factor in an array of graphene mechanical resonators. *Nano Letters* **11**, 1232–1236 (2011).

[32] Liang, X. *et al.* Toward clean and crackless transfer of graphene. *ACS Nano* **5**, 9144–9153 (2011).

[33] Lin, Y.-C. *et al.* Graphene annealing: how clean can it be? *Nano Letters* **12**, 414–419 (2011).

[34] Eichler, A. *et al.* Nonlinear damping in mechanical resonators made from carbon nanotubes and graphene. *Nature Nanotechnology* **6**, 339–342 (2011).

[35] Barton, R. A., Parpia, J. & Craighead, H. G. Fabrication and performance of graphene nanoelectromechanical systems. *Journal of Vacuum Science & Technology B* **29**, 050801 (2011).

[36] Chen, C. & Hone, J. Graphene nanoelectromechanical systems. *Proceedings of the IEEE* **101**, 1766–1779 (2013).

[37] Bunch, J. S. *Mechanical and electrical properties of graphene sheets*. Ph.D. thesis, Cornell University (2008).

[38] van der Zande, A. M. *The structure and mechanics of atomically-thin graphene membranes*. Ph.D. thesis, Cornell University (2011).

[39] Barton, R. A. *Engineering atomically thin mechanical systems*. Ph.D. thesis, Cornell University (2013).

[40] Storch, I. R. *Temperature-dependent mechanics in suspended graphene systems*. Ph.D. thesis, Cornell University (2015).

[41] Metzger, C., Favero, I., Ortlieb, A. & Karrai, K. Optical self cooling of a deformable Fabry-Perot cavity in the classical limit. *Physical Review B* **78**, 035309 (2008).

[42] Metzger, C. *et al.* Self-induced oscillations in an optomechanical system driven by bolometric backaction. *Physical Review Letters* **101**, 133903 (2008).

[43] Adiga, V. P. *et al.* Simultaneous electrical and optical readout of graphene-coated high Q silicon nitride resonators. *Applied Physics Letters* **103**, 143103 (2013).

[44] De Alba, R. *et al.* Tunable phonon-cavity coupling in graphene membranes. *Nature Nanotechnology* **11**, 741–746 (2016).

[45] De Alba, R., Abhilash, T. S., Rand, R., Craighead, H. G. & Parpia, J. M. Low-power photothermal self-oscillation of bimetallic nanowires. *ArXiv e-prints* (2016). 1610.07591.

[46] Craighead, H. G. Nanoelectromechanical systems. *Science* **290**, 1532–1535 (2000).

[47] Ekinci, K. L. & Roukes, M. L. Nanoelectromechanical systems. *Review of Scientific Instruments* **76**, 061101 (2005).

[48] Thompson, J. D. *et al.* Strong dispersive coupling of a high-finesse cavity to a micromechanical membrane. *Nature* **452**, 72–75 (2008).

[49] Dean Jr., R. N. & Luque, A. Applications of microelectromechanical systems in industrial processes and services. *IEEE Transactions on Industrial Electronics* **56**, 913–925 (2009).

[50] Naik, A. K., Hanay, M. S., Hiebert, W. K., Feng, X. L. & Roukes, M. L. Towards single-molecule nanomechanical mass spectrometry. *Nature Nanotechnology* **4**, 445–450 (2009).

[51] Ilic, B. *et al.* Enumeration of DNA molecules bound to a nanomechanical oscillator. *Nano Letters* **5**, 925–929 (2005).

[52] Park, J. *et al.* A mechanical nanomembrane detector for time-of-flight mass spectrometry. *Nano Letters* **11**, 3681–3684 (2011).

[53] Garcia-Sanchez, D., Fong, K. Y., Bhaskaran, H., Lamoreaux, S. & Tang, H. X. Casimir force and in situ surface potential measurements on nanomembranes. *Physical Review Letters* **109**, 027202 (2012).

[54] Adiga, V. P. *et al.* Approaching intrinsic performance in ultra-thin silicon nitride drum resonators. *Journal of Applied Physics* **112**, 064323 (2012).

[55] Adiga, V. P. *et al.* Modal dependence of dissipation in silicon nitride drum resonators. *Applied Physics Letters* **99**, 253103 (2011).

[56] Wilson, D. J., Regal, C. A., Papp, S. B. & Kimble, H. J. Cavity optome-

chanics with stoichiometric sin films. *Physical Review Letters* **103**, 207204 (2009).

[57] Wilson-Rae, I. *et al.* High-Q nanomechanics via destructive interference of elastic waves. *Physical Review Letters* **106**, 047205 (2011).

[58] Sekaric, L., Carr, D. W., Evoy, S., Parpia, J. M. & Craighead, H. G. Nanomechanical resonant structures in silicon nitride: fabrication, operation and dissipation issues. *Sensors and Actuators A: Physical* **101**, 215–219 (2002).

[59] Biswas, T. S. *et al.* High-Q gold and silicon nitride bilayer nanostrings. *Applied Physics Letters* **101**, 093105 (2012).

[60] Yu, P.-L., Purdy, T. P. & Regal, C. A. Control of material damping in high-Q membrane microresonators. *Physical Review Letters* **108**, 083603 (2012).

[61] Nair, R. R. *et al.* Fine structure constant defines visual transparency of graphene. *Science* **320**, 1308–1308 (2008).

[62] Shivaraman, S. *et al.* Free-standing epitaxial graphene. *Nano Letters* **9**, 3100–3105 (2009).

[63] Sridaran, S. & Bhave, S. A. Electrostatic actuation of silicon optomechanical resonators. *Optics Express* **19**, 9020–9026 (2011).

[64] Perahia, R., Cohen, J. D., Meenehan, S., Alegre, T. P. M. & Painter, O. Electrostatically tunable optomechanical "zipper" cavity laser. *Applied Physics Letters* **97**, 191112 (2010).

[65] Xiong, C., Fan, L., Sun, X. & Tang, H. X. Cavity piezooptomechanics: Piezoelectrically excited, optically transduced optomechanical resonators. *Applied Physics Letters* **102**, 021110 (2013).

[66] Eriksson, A. M., Midtvedt, D., Croy, A. & Isacsson, A. Frequency tuning, nonlinearities and mode coupling in circular mechanical graphene resonators. *Nanotechnology* **24**, 395702 (2013).

[67] Zaitsev, S., Gottlieb, O. & Buks, E. Nonlinear dynamics of a microelectromechanical mirror in an optical resonance cavity. *Nonlinear Dynamics* **69**, 1589–1610 (2012).

[68] Yuvaraj, D., Kadam, M. B., Shtempluck, O. & Buks, E. Optomechanical cavity with a buckled mirror. *Journal of Microelectromechanical Systems* **22**, 430–437 (2013).

[69] Lee, K. H., McRae, T. G., Harris, G. I., Knittel, J. & Bowen, W. P. Cooling and control of a cavity optoelectromechanical system. *Physical Review Letters* **104**, 123604 (2010).

[70] Carr, D. W. & Craighead, H. G. Fabrication of nanoelectromechanical systems in single crystal silicon using silicon on insulator substrates and electron beam lithography. *Journal of Vacuum Science & Technology B* **15**, 2760–2763 (1997).

[71] Singh, V. *et al.* Probing thermal expansion of graphene and modal dispersion at low-temperature using graphene nanoelectromechanical systems resonators. *Nanotechnology* **21**, 165204 (2010).

[72] Lee, J., Wang, Z., He, K., Shan, J. & Feng, P. X.-L. High frequency MoS_2 nanomechanical resonators. *ACS Nano* **7**, 6086–6091 (2013).

[73] Metzger, C. H. & Karrai, K. Cavity cooling of a microlever. *Nature* **432**, 1002–1005 (2004).

[74] Orfanidis, S. J. *Electromagnetic waves and antennas* (Rutgers University New Brunswick, NJ, 2002).

[75] Ando, T., Zheng, Y. & Suzuura, H. Dynamical conductivity and zero-mode anomaly in honeycomb lattices. *Journal of the Physical Society of Japan* **71**, 1318–1324 (2002).

[76] Gusynin, V. P., Sharapov, S. G. & Carbotte, J. P. Unusual microwave response of Dirac quasiparticles in graphene. *Physical Review Letters* **96**, 256802 (2006).

[77] Barnes, J. R. *et al.* A femtojoule calorimeter using micromechanical sensors. *Review of Scientific Instruments* **65**, 3793–3798 (1994).

[78] Teufel, J. D. *et al.* Sideband cooling of micromechanical motion to the quantum ground state. *Nature* **475**, 359–363 (2011).

[79] Andrews, R. W. *et al.* Bidirectional and efficient conversion between microwave and optical light. *Nature Physics* **10**, 321–326 (2014).

[80] Mahboob, I., Nishiguchi, K., Okamoto, H. & Yamaguchi, H. Phonon-cavity electromechanics. *Nature Physics* **8**, 387–392 (2012).

[81] Mahboob, I., Nishiguchi, K., Fujiwara, A. & Yamaguchi, H. Phonon lasing in an electromechanical resonator. *Physical Review Letters* **110**, 127202 (2013).

[82] Khan, R., Massel, F. & Heikkilä, T. T. Tension-induced nonlinearities of flexural modes in nanomechanical resonators. *Physical Review B* **87**, 235406 (2013).

[83] Song, X. *et al.* Stamp transferred suspended graphene mechanical resonators for radio frequency electrical readout. *Nano Letters* **12**, 198–202 (2012).

[84] Eichler, A., del Álamo Ruiz, M., Plaza, J. & Bachtold, A. Strong coupling between mechanical modes in a nanotube resonator. *Physical Review Letters* **109**, 025503 (2012).

[85] Liu, C.-H., Kim, I. S. & Lauhon, L. J. Optical control of mechanical mode-coupling within a MoS_2 resonator in the strong-coupling regime. *Nano Letters* **15**, 6727–6731 (2015).

[86] Cole, R. M. *et al.* Evanescent-field optical readout of graphene mechanical motion at room temperature. *Physical Review Applied* **3**, 024004 (2015).

[87] Song, X., Oksanen, M., Li, J., Hakonen, P. J. & Sillanpää, M. A. Graphene optomechanics realized at microwave frequencies. *Physical Review Letters* **113**, 027404 (2014).

[88] Atalaya, J., Kinaret, J. M. & Isacsson, A. Nanomechanical mass measurement using nonlinear response of a graphene membrane. *EPL (Europhysics Letters)* **91**, 48001 (2010).

[89] Westra, H. J. R., Poot, M., Van Der Zant, H. S. J. & Venstra, W. J. Nonlinear modal interactions in clamped-clamped mechanical resonators. *Physical Review Letters* **105**, 117205 (2010).

[90] Patil, Y. S., Chakram, S., Chang, L. & Vengalattore, M. Thermomechanical two-mode squeezing in an ultrahigh-Q membrane resonator. *Physical Review Letters* **115**, 017202 (2015).

[91] Ruiz-Vargas, C. S. *et al.* Softened elastic response and unzipping in chemical vapor deposition graphene membranes. *Nano Letters* **11**, 2259–2263 (2011).

[92] Bunch, J. S. *et al.* Impermeable atomic membranes from graphene sheets. *Nano Letters* **8**, 2458–2462 (2008).

[93] Wang, Z., Lee, J., He, K., Shan, J. & Feng, P. X.-L. Embracing structural nonidealities and asymmetries in two-dimensional nanomechanical resonators. *Scientific Reports* **4** (2014).

[94] Knothe, K. History of wheel/rail contact mechanics: from Redtenbacher to Kalker. *Vehicle System Dynamics* **46**, 9–26 (2008).

[95] Denegri, C. M. Limit cycle oscillation flight test results of a fighter with external stores. *Journal of Aircraft* **37**, 761–769 (2000).

[96] Pai, A., Dhurandhar, S. V., Hello, P. & Vinet, J.-Y. Radiation pressure induced instabilities in laser interferometric detectors of gravitational waves. *The European Physical Journal D* **8**, 333–346 (2000).

[97] May, R. M. Limit cycles in predator-prey communities. *Science* **177**, 900–902 (1972).

[98] Arcizet, O., Cohadon, P.-F., Briant, T., Pinard, M. & Heidmann, A. Radiation-pressure cooling and optomechanical instability of a micromirror. *Nature* **444**, 71–74 (2006).

[99] Poot, M. *et al.* Tunable backaction of a DC SQUID on an integrated micromechanical resonator. *Physical Review Letters* **105**, 207203 (2010).

[100] Etaki, S., Konschelle, F., Blanter, Y. M., Yamaguchi, H. & Van Der Zant, H. Self-sustained oscillations of a torsional SQUID resonator induced by Lorentz-force back-action. *Nature Communications* **4**, 1803 (2013).

[101] Zook, J. D. *et al.* Fiber-optic vibration sensor based on frequency modulation of light-excited oscillators. *Sensors and Actuators A: Physical* **83**, 270–276 (2000).

[102] Ekinci, K. L., Yang, Y. T. & Roukes, M. L. Ultimate limits to inertial mass sensing based upon nanoelectromechanical systems. *Journal of Applied Physics* **95**, 2682–2689 (2004).

[103] Ilic, B., Yang, Y. & Craighead, H. G. Virus detection using nanoelectromechanical devices. *Applied Physics Letters* **85**, 2604–2606 (2004).

[104] Nguyen, C. T.-C. MEMS technology for timing and frequency control. In *Proceedings of the 2005 IEEE International Frequency Control Symposium and Exposition, 2005.*, 11–pp (IEEE, 2005).

[105] Verd, J. *et al.* Monolithic CMOS MEMS oscillator circuit for sensing in the attogram range. *IEEE Electron Device Letters* **29**, 146–148 (2008).

[106] Van Beek, J. T. M. & Puers, R. A review of MEMS oscillators for frequency reference and timing applications. *Journal of Micromechanics and Microengineering* **22**, 013001 (2011).

[107] Gavartin, E., Verlot, P. & Kippenberg, T. J. A hybrid on-chip optomechanical transducer for ultrasensitive force measurements. *Nature Nanotechnology* **7**, 509–514 (2012).

[108] Feng, X. L., White, C. J., Hajimiri, A. & Roukes, M. L. A self-sustaining

ultrahigh-frequency nanoelectromechanical oscillator. *Nature Nanotechnology* **3**, 342–346 (2008).

[109] Weldon, J. A., Alemán, B., Sussman, A., Gannett, W. & Zettl, A. K. Sustained mechanical self-oscillations in carbon nanotubes. *Nano Letters* **10**, 1728–1733 (2010).

[110] Chen, C., Zanette, D. H., Guest, J. R., Czaplewski, D. A. & López, D. Self-sustained micromechanical oscillator with linear feedback. *Physical Review Letters* **117**, 017203 (2016).

[111] Zalalutdinov, M. *et al.* Autoparametric optical drive for micromechanical oscillators. *Applied Physics Letters* **79**, 695–697 (2001).

[112] Kleckner, D. & Bouwmeester, D. Sub-kelvin optical cooling of a micromechanical resonator. *Nature* **444**, 75–78 (2006).

[113] Gigan, S. *et al.* Self-cooling of a micromirror by radiation pressure. *Nature* **444**, 67–70 (2006).

[114] Eichenfield, M., Camacho, R., Chan, J., Vahala, K. J. & Painter, O. A picogram- and nanometre-scale photonic-crystal optomechanical cavity. *Nature* **459**, 550–555 (2009).

[115] Schliesser, A., Arcizet, O., Rivière, R., Anetsberger, G. & Kippenberg, T. J. Resolved-sideband cooling and position measurement of a micromechanical oscillator close to the Heisenberg uncertainty limit. *Nature Physics* **5**, 509–514 (2009).

[116] Chan, J. *et al.* Laser cooling of a nanomechanical oscillator into its quantum ground state. *Nature* **478**, 89–92 (2011).

[117] Ramos, D., Mertens, J., Calleja, M. & Tamayo, J. Photothermal self-excitation of nanomechanical resonators in liquids. *Applied Physics Letters* **92**, 173108 (2008).

[118] Ramos, D. *et al.* Optomechanics with silicon nanowires by harnessing confined electromagnetic modes. *Nano Letters* **12**, 932–937 (2012).

[119] Blocher, D., Zehnder, A. T., Rand, R. H. & Mukerji, S. Anchor deformations drive limit cycle oscillations in interferometrically transduced MEMS beams. *Finite Elements in Analysis and Design* **49**, 52–57 (2012).

[120] Restrepo, J., Gabelli, J., Ciuti, C. & Favero, I. Classical and quantum theory of photothermal cavity cooling of a mechanical oscillator. *Comptes Rendus Physique* **12**, 860–870 (2011).

[121] Ramos, D. *et al.* Silicon nanowires: where mechanics and optics meet at the nanoscale. *Scientific Reports* **3** (2013).

[122] Zalalutdinov, M. *et al.* Frequency entrainment for micromechanical oscillator. *Applied Physics Letters* **83**, 3281–3283 (2003).

[123] Pandey, M. *et al.* Analysis of frequency locking in optically driven MEMS resonators. *Journal of Microelectromechanical Systems* **15**, 1546–1554 (2006).

[124] Pandey, M., Rand, R. & Zehnder, A. Perturbation analysis of entrainment in a micromechanical limit cycle oscillator. *Communications in Nonlinear Science and Numerical Simulation* **12**, 1291–1301 (2007).

[125] Blocher, D. B., Zehnder, A. T. & Rand, R. H. Entrainment of micromechanical limit cycle oscillators in the presence of frequency instability. *Journal of Microelectromechanical Systems* **22**, 835–845 (2013).

[126] Blankenburg, S. *et al.* Porous graphene as an atmospheric nanofilter. *Small* **6**, 2266–2271 (2010).

[127] Merchant, C. A. *et al.* DNA translocation through graphene nanopores. *Nano Letters* **10**, 2915–2921 (2010).

[128] Jiang, J.-W., Wang, J.-S. & Li, B. Thermal expansion in single-walled carbon nanotubes and graphene: Nonequilibrium Green's function approach. *Physical Review B* **80**, 205429 (2009).

[129] Zakharchenko, K. V., Katsnelson, M. I. & Fasolino, A. Finite temperature lattice properties of graphene beyond the quasiharmonic approximation. *Physical Review Letters* **102**, 046808 (2009).

[130] Reina, A. *et al.* Large area, few-layer graphene films on arbitrary substrates by chemical vapor deposition. *Nano Letters* **9**, 30–35 (2009).

[131] Li, X. *et al.* Transfer of large-area graphene films for high-performance transparent conductive electrodes. *Nano Letters* **9**, 4359–4363 (2009).

[132] Moser, J., Barreiro, A. & Bachtold, A. Current-induced cleaning of graphene. *Applied Physics Letters* **91**, 163513 (2007).

[133] Xu, Y. *et al.* Radio frequency electrical transduction of graphene mechanical resonators. *Applied Physics Letters* **97**, 243111 (2010).

[134] Nicholl, R. J. *et al.* The effect of intrinsic crumpling on the mechanics of free-standing graphene. *Nature Communications* **6** (2015).

[135] Lin, Y.-C. *et al.* Clean transfer of graphene for isolation and suspension. *ACS Nano* **5**, 2362–2368 (2011).

[136] Begley, M. R., Bart-Smith, H., Scott, O. N., Jones, M. H. & Reed, M. L. The electro-mechanical response of elastomer membranes coated with ultra-thin metal electrodes. *Journal of the Mechanics and Physics of Solids* **53**, 2557–2578 (2005).

[137] Sevostianov, I. On the thermal expansion of composite materials and cross-property connection between thermal expansion and thermal conductivity. *Mechanics of Materials* **45**, 20–33 (2012).

[138] Okada, Y. & Tokumaru, Y. Precise determination of lattice parameter and thermal expansion coefficient of silicon between 300 and 1500 K. *Journal of Applied Physics* **56**, 314–320 (1984).

[139] Middelmann, T., Walkov, A., Bartl, G. & Schödel, R. Thermal expansion coefficient of single-crystal silicon from 7 K to 293 K. *Physical Review B* **92**, 174113 (2015).

[140] Fetters, L. J., Lohse, D. J., Richter, D., Witten, T. A. & Zirkel, A. Connection between polymer molecular weight, density, chain dimensions, and melt viscoelastic properties. *Macromolecules* **27**, 4639–4647 (1994).

[141] Gilmour, I. W., Trainor, A. & Haward, R. N. Elastic moduli of glassy polymers at low strains. *Journal of Applied Polymer Science* **23**, 3129–3138 (1979).

[142] Lyon, K. G., Salinger, G. L. & Swenson, C. A. Tunneling models and the experimental thermal expansivities of fused silica and poly (methylmethacrylate)(pmma) below 4 K. *Physical Review B* **19**, 4231 (1979).

[143] Richeton, J., Schlatter, G., Vecchio, K. S., Rémond, Y. & Ahzi, S. A unified model for stiffness modulus of amorphous polymers across transition temperatures and strain rates. *Polymer* **46**, 8194–8201 (2005).

[144] Roland, C. M. Relaxation phenomena in vitrifying polymers and molecular liquids. *Macromolecules* **43**, 7875–7890 (2010).

[145] Keddie, J. L., Jones, R. A. L. & Cory, R. A. Interface and surface effects on the glass-transition temperature in thin polymer films. *Faraday Discussions* **98**, 219–230 (1994).

[146] Keddie, J. L., Jones, R. A. L. & Cory, R. A. Size-dependent depression of the glass transition temperature in polymer films. *EPL (Europhysics Letters)* **27**, 59 (1994).

[147] Forrest, J. A., Dalnoki-Veress, K., Stevens, J. R. & Dutcher, J. R. Effect of free surfaces on the glass transition temperature of thin polymer films. *Physical Review Letters* **77**, 2002 (1996).

[148] Forrest, J. A. & Dalnoki-Veress, K. The glass transition in thin polymer films. *Advances in Colloid and Interface Science* **94**, 167–195 (2001).

[149] Kawana, S. & Jones, R. A. L. Character of the glass transition in thin supported polymer films. *Physical Review E* **63**, 021501 (2001).

[150] Gent, A. N. Relaxation processes in vulcanized rubber. I. Relation among stress relaxation, creep, recovery, and hysteresis. *Journal of Applied Polymer Science* **6**, 433–441 (1962).

[151] Sternstein, S. S. & Ho, T. C. Biaxial stress relaxation in glassy polymers: polymethylmethacrylate. *Journal of Applied Physics* **43**, 4370–4383 (1972).

[152] Tervoort, T. A., Klompen, E. T. J. & Govaert, L. E. A multi-mode approach to finite, three-dimensional, nonlinear viscoelastic behavior of polymer glasses. *Journal of Rheology* **40**, 779–797 (1996).

[153] Roland, C. M. Characteristic relaxation times and their invariance to thermodynamic conditions. *Soft Matter* **4**, 2316–2322 (2008).

[154] Hodge, I. M. Physical aging in polymer glasses. *Science* **267**, 1945 (1995).

[155] *Wolfram Alpha* (Wolfram Alpha LLC, 2016). URL `www.wolframalpha.com`.

[156] Hauer, B. D., Doolin, C., Beach, K. S. D. & Davis, J. P. A general procedure for thermomechanical calibration of nano/micro-mechanical resonators. *Annals of Physics* **339**, 181–207 (2013).

[157] Cleveland, J. P., Manne, S., Bocek, D. & Hansma, P. K. A nondestructive method for determining the spring constant of cantilevers for scanning force microscopy. *Review of Scientific Instruments* **64**, 403–405 (1993).

[158] Geim, A. K. & Grigorieva, I. V. Van der Waals heterostructures. *Nature* **499**, 419–425 (2013).

[159] Shanmugam, M., Jacobs-Gedrim, R., Song, E. S. & Yu, B. Two-dimensional layered semiconductor/graphene heterostructures for solar photovoltaic applications. *Nanoscale* **6**, 12682–12689 (2014).

[160] Britnell, L. *et al.* Field-effect tunneling transistor based on vertical graphene heterostructures. *Science* **335**, 947–950 (2012).

[161] Lee, J., Wang, Z., He, K., Shan, J. & Feng, P. X.-L. High frequency MoS_2 nanomechanical resonators. *ACS nano* **7**, 6086–6091 (2013).